



AFRL-RZ-WP-TR-2010-2167

**POWER AND THERMAL TECHNOLOGIES FOR AIR AND
SPACE-SCIENTIFIC RESEARCH PROGRAM**

**Delivery Order 0012: High-Temperature Superconductor Performance
Enhancement**

Chakrapani Varanasi

University of Dayton Research Institute

JUNE 2010

Final Report

Approved for public release; distribution unlimited.

See additional restrictions described on inside pages

STINFO COPY

**AIR FORCE RESEARCH LABORATORY
PROPULSION DIRECTORATE
WRIGHT-PATTERSON AIR FORCE BASE, OH 45433-7251
AIR FORCE MATERIEL COMMAND
UNITED STATES AIR FORCE**

NOTICE AND SIGNATURE PAGE

Using Government drawings, specifications, or other data included in this document for any purpose other than Government procurement does not in any way obligate the U.S. Government. The fact that the Government formulated or supplied the drawings, specifications, or other data does not license the holder or any other person or corporation; or convey any rights or permission to manufacture, use, or sell any patented invention that may relate to them.

This report was cleared for public release by the USAF 88th Air Base Wing (88 ABW) Public Affairs (AFRL/PA) Office and is available to the general public, including foreign nationals. Copies may be obtained from the Defense Technical Information Center (DTIC) (<http://www.dtic.mil>).

AFRL-RZ-WP-TR-2010-2167 HAS BEEN REVIEWED AND IS APPROVED FOR PUBLICATION IN ACCORDANCE WITH THE ASSIGNED DISTRIBUTION STATEMENT.

*//Signature//

LT BREANNA RUTER-SCHOPPMAN
Project Engineer
Mechanical Energy Conversion Branch
Energy/Power/Thermal Division
Propulsion Directorate

//Signature//

JACK VONDRELL
Branch Chief
Mechanical Energy Conversion Branch
Energy/Power/Thermal Division
Propulsion Directorate

This report is published in the interest of scientific and technical information exchange, and its publication does not constitute the Government's approval or disapproval of its ideas or findings.

*Disseminated copies will show “//Signature//” stamped or typed above the signature blocks.

REPORT DOCUMENTATION PAGE				Form Approved OMB No. 0704-0188	
<p>The public reporting burden for this collection of information is estimated to average 1 hour per response, including the time for reviewing instructions, searching existing data sources, gathering and maintaining the data needed, and completing and reviewing the collection of information. Send comments regarding this burden estimate or any other aspect of this collection of information, including suggestions for reducing this burden, to Department of Defense, Washington Headquarters Services, Directorate for Information Operations and Reports (0704-0188), 1215 Jefferson Davis Highway, Suite 1204, Arlington, VA 22202-4302. Respondents should be aware that notwithstanding any other provision of law, no person shall be subject to any penalty for failing to comply with a collection of information if it does not display a currently valid OMB control number. PLEASE DO NOT RETURN YOUR FORM TO THE ABOVE ADDRESS.</p>					
1. REPORT DATE (DD-MM-YY) June 2010		2. REPORT TYPE Final		3. DATES COVERED (From - To) 18 December 2006 – 30 April 2010	
4. TITLE AND SUBTITLE POWER AND THERMAL TECHNOLOGIES FOR AIR AND SPACE-SCIENTIFIC RESEARCH PROGRAM Delivery Order 0012: High-Temperature Superconductor Performance Enhancement				5a. CONTRACT NUMBER FA8650-04-D-2403-0012	
				5b. GRANT NUMBER	
				5c. PROGRAM ELEMENT NUMBER 62203F	
6. AUTHOR(S) Chakrapani Varanasi				5d. PROJECT NUMBER 3145	
				5e. TASK NUMBER G2	
				5f. WORK UNIT NUMBER 3145G200	
7. PERFORMING ORGANIZATION NAME(S) AND ADDRESS(ES) University of Dayton Research Institute Metals & Ceramics Division 300 College Park Dayton, OH 45469-0170				8. PERFORMING ORGANIZATION REPORT NUMBER UDR-TR-2010-0063	
9. SPONSORING/MONITORING AGENCY NAME(S) AND ADDRESS(ES) Air Force Research Laboratory Propulsion Directorate Wright-Patterson Air Force Base, OH 45433-7251 Air Force Materiel Command United States Air Force				10. SPONSORING/MONITORING AGENCY ACRONYM(S) AFRL/RZPG	
				11. SPONSORING/MONITORING AGENCY REPORT NUMBER(S) AFRL-RZ-WP-TR-2010-2167	
12. DISTRIBUTION/AVAILABILITY STATEMENT Approved for public release; distribution unlimited.					
13. SUPPLEMENTARY NOTES PAO Case Number: 88ABW-2010-5311, Clearance Date: 01 Oct 2010. Report contains color.					
14. ABSTRACT The objectives of this delivery order were to 1) Improve critical current density in applied magnetic fields through flux pinning mechanisms and thicker films. 2) Investigate AC losses in YBCO coated conductors 3) Develop means to stabilize YBCO thin filmed coated conductors and electrically connect them to the substrate. 4) Develop improved measurement techniques and standards of measurement for properties of high temperature superconductors in order to fully characterize AC loss issues, flux pinning effects, stabilization concerns, and higher critical currents. 5) Research the growth and characterization of carbon nanotubes for electrical and thermal applications.					
15. SUBJECT TERMS superconductivity, carbon nanotubes, AC loss					
16. SECURITY CLASSIFICATION OF:			17. LIMITATION OF ABSTRACT: SAR	18. NUMBER OF PAGES 92	19a. NAME OF RESPONSIBLE PERSON (Monitor) Lt Breanna Ruter-Schoppman 19b. TELEPHONE NUMBER (Include Area Code) N/A
a. REPORT Unclassified	b. ABSTRACT Unclassified	c. THIS PAGE Unclassified			

TABLE OF CONTENTS

Section	Section Title	Page
	List of Figures and Tables	v
	Foreword	ix
	1. Flux Pinning Enhancements in $\text{YBa}_2\text{Cu}_3\text{O}_{7-x}$ through BaSnO_3 Nanocolumns	
1.1	Introduction	1
1.2	Experimental	2
1.3	Results and Discussion	4
1.4	Conclusion	32
1.5	References	33
	2. Effects of Second Phase (BaGeO_3, BaSiO_3) Nanocolumns in $\text{YBa}_2\text{Cu}_3\text{O}_{7-x}$ Films	
2.1	Introduction	35
2.2	Experimental	35
2.3	Results and Discussion	37
2.4	Conclusion	41
2.5	References	41
	3. $\text{YBa}_2\text{Cu}_3\text{O}_{7-x}$ Coated Conductors on Ceraflex (Polycrystalline Flexible Yttria-Stabilized Zirconia) Substrates	
3.1	Introduction	43
3.2	Experimental	43
3.3	Results and Discussion	46
3.4	Conclusion	52
3.5	References	53
	4. Carbon Nanotubes Growth and Characterization for Electrical and Thermal Applications: Constantan (Ni-Cu-Mn Alloy) Metallic Substrates without Adding Additional Catalysts	
4.1	Introduction	54
4.2	Experimental	54
4.3	Results and Discussion	55
4.4	Conclusion	59
4.5	References	60
	5. Carbon Nanotubes Growth and Characterization for Electrical and Thermal Applications: Diamond Substrates	
5.1	Introduction	62
5.2	Experimental	63
5.3	Results and Discussion	63
5.4	Conclusion	68
5.5	References	69

	6. AC Losses in Superconductors	
6.1	Introduction	70
6.2	Experimental	70
6.3	Results and Discussion	74
6.4	Conclusion	76
6.5	References	77
	List of Acronyms, Abbreviations and Symbols	78

LIST OF FIGURES AND TABLES

1. Flux Pinning Enhancements in $\text{YBa}_2\text{Cu}_3\text{O}_{7-x}$ through BaSnO_3 Nanocolumns		
Figure	Figure Title	Page
1.1	Schematic diagram of a PLD YBCO target with a small sector of a second phase such as Y_2BaCuO_5 or BaSnO_3 as an (a) inserted type or (b) thin sector on top type	3
1.2	Magnetization J_c data (H/c) of YBCO+Y211 and YBCO+BSO films made by sectored target method	5
1.3a	SEM micrograph of YBCO+Y211 film made by sectored target approach	6
1.3b	Cross-sectional TEM micrograph of YBCO+Y211 film made by sectored target approach	6
1.4a	Cross-sectional TEM micrograph of a YBCO+BSO film made by sectored target approach	7
1.4b	Plan view TEM micrograph of a YBCO+BSO film made by sectored target approach	7
1.5	Normalized plot of transport critical current density (J_{ct}) in applied magnetic field of a YBCO+BSO sample on LaAlO_3 substrate at 77 K	8
1.6	Temperature dependence of α values for a control YBCO and YBCO+BSO samples	8
1.7	Angular dependence of J_{ct} values of YBCO+BSO sample on a LaAlO_3 substrate at various applied fields of 1, 3 and 5 T at 77 K	9
1.8	Normalized J_{ct} with respect to J_{ct} in H/ab for a YBCO+BSO sample as compared to regular YBCO at 77 K	10
1.9	Angular dependence of J_{ct} for a YBCO+BSO film on a buffered metallic Ni-W substrate in an applied magnetic field of 1 T at 77 K	10
1.10	Scanning electron micrograph of an YBCO+BSO sample on a buffered Ni-W metallic substrate	11
1.11	Cross-sectional TEM image of an YBCO+BSO sample on a LaAlO_3 substrate with BSO particles identified in the selected area diffraction pattern	11
1.12	(a) High resolution TEM image of an YBCO+BSO film showing high density of dislocations and stacking faults; (b) FFT filtered image showing the existence of high density of misfit dislocations and stacking faults at the YBCO/BSO interfaces	12
1.13	Alpha values of YBCO+Y211 and YBCO+BSO films at different temperatures	13
1.14	Magnetization J_c of YBCO+BSO films at various temperatures	13
1.15	F_p plots of YBCO+BSO, YBCO+211 and YBCO films at 77 K	14
1.16	X-ray $\theta - 2\theta$ scan patterns scans of various YBCO+BSO films	14
1.17	T_c variation in YBCO+BSO films with varying BSO content	15
1.18	Magnetization J_c of YBCO+BSO films as a function of applied magnetic field with varying amounts of BSO content as compared to regular YBCO (a) at 77 K (b) at 65 K	16
1.19	Magnetization J_c of YBCO+BSO films as a function of the BSO content at various magnetic fields at 77 K	17
1.20	Flux pinning force (F_p) of different YBCO + BSO films (a) F_p at 77 K, (b) $F_p/F_{p_{\max}}$ at 77 K, (c) F_p at 65 K, (d) $F_p/F_{p_{\max}}$ at 65 K	18
1.21	Scanning electron micrograph showing the BSO nanoparticles in a YBCO+4 mol% BSO sample: (a) low magnification micrograph showing large particles, and (b) high magnification micrograph showing nanoparticles in plan view	19
1.22	TEM images showing (a) YBCO+2 mol% BSO in plan view, (b) YBCO+20 mol% BSO in plan view, (c) YBCO+2 mol% BSO in cross-section view, and (d) YBCO+2 mol% BSO in cross-section view	20
1.23	(a) Critical current density (J_c) of different thickness YBCO+BSO nanocomposite films as compared to 300 nm YBCO samples at 77 K, H/c and a NbTi sample at 4.2 K; (b) Flux pinning force (F_p) data for various samples with different thicknesses	22
1.24	J_c values of YBCO+BSO films with different thicknesses at different applied fields measured at 77 K, with H/c orientation	23
1.25	SEM micrograph of a $\sim 3.6 \mu\text{m}$ film showing uniform distribution of BSO in YBCO matrix	23
1.26	TEM cross-sectional image of a $\sim 3.6 \mu\text{m}$ film showing the BSO nanocolumns extending	24

	throughout the thickness of the films	
1.27	Cross-sectional TEM images of YBCO+BSO thick films at different magnifications showing that the BSO nanocolumns extend throughout the thickness	24
1.28	Cross-sectional TEM image of YBCO+BSO thick films showing the ordering of nanocolumns as shown by arrow marks	25
1.29	High resolution scanning electron images of YBCO+BSO thick films with different thicknesses (t) showing the planar view of the BSO nanorods	26
1.30	Low magnification SEM images of YBCO+BSO thick film showing an increase in the amount of mis-oriented grains as the thickness was increased.	27
1.31	X-ray diffraction patterns of YBCO+BSO thick films showing the BSO (100) and YBCO (100) peaks in all samples; an increase in YBCO (103) is seen as thickness was increased	28
1.32	T_c in YBCO+20 mol% BSO films with varying thickness	28
1.33	J_c values for varying thickness YBCO+20 mol% BSO films at 77 K and H//c	29
1.34	VSM J_c data for selected YBCO+20 mol% BSO film thicknesses compared with 300 nm YBCO at 77 K and H//c	30
1.35	X-ray $\theta - 2\theta$ scans of YBCO+20 mol% BSO of varying thickness	30
1.36	SEM photomicrograph showing surface microstructure of (a) 260 nm sample and a (b) 2.8 μm sample	31
1.37	SEM photomicrograph showing uniform BSO distribution in YBCO on (a) 260 nm sample and a (b) 2.8 μm sample	31
1.38	Cross sectional TEM image showing through-thickness, uniform BSO nanocolumns in (a) 780nm film and a (b) 2.8 μm film	32

2. Effects of Second Phase (BaGeO₃, BaSiO₃) Nanocolumns in YBa₂Cu₃O_{7-x} Films		
Figure	Figure Title	Page
2.1	X-ray $\theta - 2\theta$ scans of BaGeO ₃ prepared samples	37
2.2	X-ray $\theta - 2\theta$ patterns of Ba-Si-O powder	38
2.3	Plan View SEM micrographs of YBCO films made by using a PLD sectored targets of (a) YBCO+BGeO and (b) YBCO+BSiO	38
2.4	Cross-sectional TEM micrographs of YBCO+BGeO samples showing the nanocolumns at two different magnifications: (a) low magnification and (b) high magnification	39
2.5	X-ray $\theta - 2\theta$ diffraction patterns of YBCO+BGeO films showing the (001) orientation of YBCO films	39
2.6	Cross-sectional TEM showing the nanocolumns in YBCO+BSiO films at two different magnifications: (a) low magnification and (b) high magnification	40
2.7	Susceptibility of YBCO+BGeO and YBCO+BSiO films showing the T_c data of different samples	40

3. YBa₂Cu₃O_{7-x} Coated Conductors on Ceraflex (Polycrystalline Flexible Yttria-Stabilized Zirconia) Substrates		
Figure	Figure Title	Page
3.1	Optical macrograph of a Ceraflex tensile test specimen in aluminum tabs with width measurements	44
3.2	Optical macrograph of a tested Ceraflex tensile test specimen at the end of the test showing the fractured tensile gage section: (a) top half and (b) bottom half	45
3.3	Stress-extension curves of a Ceraflex substrate compared with a stress-extension curve of a biaxially textured Ni-5 at% W substrate	47
3.4	X-ray $\theta - 2\theta$ diffraction patterns of (a) YBCO/LMO/single crystal MgO, and (b) and (c) two different samples of YBCO/LMO/IBAD-MgO/Y ₂ O ₃ /SiO ₂ / Ceraflex	48
3.5	Phi scans of (110) YBCO on (a) YBCO/LMO/ single crystal MgO, and (b)	48

	YBCO/LMO/IBAD-MgO/Y ₂ O ₃ / SiO ₂ / Ceraflex	
3.6	(200) YBCO Omega scans of YBCO/LMO/IBAD-MgO/Y ₂ O ₃ /SiO ₂ /Ceraflex in (a) longitudinal and (b) transverse directions	49
3.7	Scanning electron micrograph of a YBCO/LMO/IBAD-MgO/Y ₂ O ₃ /SiO ₂ / Ceraflex sample	49
3.8	AC susceptibility curves of (a) YBCO/LMO/single crystal MgO and (b) YBCO/LMO/IBAD-MgO/Y ₂ O ₃ /SiO ₂ /Ceraflex	50
3.9	Magnetization J _c data as a function of applied magnetic field of YBCO/LMO/IBAD-MgO/Y ₂ O ₃ / SiO ₂ /Ceraflex sample at 77 K and 65 K	50
3.10	SIMS depth profile analyses of a YBCO/LMO/IBAD-MgO/Y ₂ O ₃ /SiO ₂ / Ceraflex sample	51

4. Carbon Nanotubes Growth and Characterization for Electrical and Thermal Applications: Constantan (Ni-Cu-Mn Alloy) Metallic Substrates without Adding Additional Catalysts		
Figure	Figure Title	Page
4.1	Scanning electron micrograph of a Si substrate sample with Ni islands deposited using a pulsed laser ablation method and then annealed	55
4.2	Scanning electron micrograph showing CNTs on the Si substrate sample decorated with Ni islands presented in Figure 4.1	56
4.3	Cross-sectional SEM of the same sample showing the thickness of the CNT mat grown on the Si substrate with PLD deposited Ni islands	56
4.4	CNTs grown on a rolled and low temp annealed (500 °C, 3 h), mechanically roughened, constantan substrate	56
4.5	CNTs grown on a rolled and high temp annealed (1200 °C, 2 h), ion milled constantan substrate	57
4.6	CNTs grown on as rolled, mechanically grinded constantan substrate	57
4.7	Transmission electron micrograph of CNTs grown on high temp annealed (1200 °C, 2 h), ion milled constantan substrates	58
4.8	Transmission electron micrograph of CNTs showing tip growth mechanism may also be possible in the constantan substrates	58
4.9	Raman spectra of CNTs grown on three different substrates: (a) constantan substrate annealed and then ion milled to roughen, (b) constantan substrate annealed and mechanically grinded to roughen, and (c) constantan substrate on as rolled condition and mechanically grinded	59

5. Carbon Nanotubes Growth and Characterization for Electrical and Thermal Applications: Diamond Substrates		
Figure	Figure Title	Page
5.1	SEM micrograph of as grown diamond sample showing facets of crystals	63
5.2	X-ray diffraction pattern taken from a diamond substrate	63
5.3	Raman spectra taken from a diamond substrate as compared to CNT/diamond samples grown at two different processing conditions	64
5.4	Partial coverage of CNTs grown on diamond substrate partially covered with Ni-W- Fe deposited by using initial sputtering conditions	65
5.5	Complete coverage of CNTs on diamond substrates with Ni catalysts deposited by sputtering using optimized conditions	65
5.6	Higher magnification pictures showing the CNTs grown on a diamond substrate	66
5.7	Cross-sectional SEM image showing CNTs grown on a diamond substrate	66
5.8	(a) TEM micrograph showing 20 nm diameter CNTs grown on diamond substrates (b) High resolution TEM micrograph showing 16 Walls of highly crystalline MWCNT	67

6. AC Losses in Superconductors		
Figure	Figure Title	Page
6.1	Compensation curve from resistance	70
6.2	Schematic of resistance heater used for calibration	70
6.3	Schematic of initial system	71
6.4	Schematic of modified system showing taller lead cooling section	72
6.5	Results from initial coil measurements	73
6.6	Cross section of SAM machine	74
6.7	Schematic indicating the vacuum space	74

Table	Table Title	Page
3.1	Summary of Yield Strength Measurements	46

FOREWORD

The work documented in this report (UDRI report number UDR-TR-2010-0063) was performed by the University of Dayton Research Institute (UDRI) between December 2006 and April 2010, for the Propulsion Directorate of the Air Force Research Laboratory, Wright-Patterson Air Force Base, Ohio. The effort was performed as Delivery Order 0012 on Contract No. FA8650-04-D-2403, Power and Thermal Technologies for Air and Space – Scientific Research Program (SRP).

Technical support and direction of this delivery order was provided by Dr. Paul Barnes and his staff of AFRL/RZPG. Dr. Chakrapani Varanasi was the Delivery Order Principal Investigator and is the primary author of the report. Organizational revisions to the report were made by Dr. Evan L. Thomas. Dr. Varanasi was supported by his staff, John Murphy, Lyle Brunke, Jack Burke and Dr. Evan L. Thomas.

The author would like to thank Lt. Breanna Ruter-Schoppman for providing the delivery order government administration. The author also wishes to acknowledge the assistance of Ms. Sheila Liskany and Mr. Jeffrey Fox of the UDRI, who provided the administrative support to make this work possible. Mr. Fox is the SRP Program Manager.

1. Flux Pinning Enhancements in $\text{YBa}_2\text{Cu}_3\text{O}_{7-x}$ through BaSnO_3 Nanocolumns

1.1. Introduction

Coated conductors are electrical conductors prepared with $\text{YBa}_2\text{Cu}_3\text{O}_{7-x}$ (YBCO) superconducting material coatings deposited on metallic substrates along with several other intermediate buffer layers. Buffer layers are deposited sequentially on the metallic substrates prior to YBCO deposition to serve as barrier layers. They are selected such that epitaxial relationships are maintained throughout the thickness of the coated conductors to obtain highly-textured YBCO coatings. To process conductors with high critical current density (J_c), highly-textured YBCO coatings with both in-plane and out-of-plane alignment of grains are required with grain boundary mis-orientation angles below 5° . More details of the texture requirements, processing, and different types of coated conductor architectures can be found in the references [1-5]. Two primary industrial approaches are used to manufacture the coated conductors. One approach uses a rolling-assisted-biaxially-textured (RABiTSTM) metallic substrate such as Ni-5 at.% W with sputtered $\text{Y}_2\text{O}_3/\text{YSZ}/\text{Ce}_2\text{O}_3$ buffer layers and YBCO layer deposited by the metallo-organic deposition (MOD) technique [3]. In the second approach, a polycrystalline HastelloyTM substrate is coated with textured MgO buffer layer grown by ion-beam assisted deposition (IBAD) and other subsequent buffer layers [4]. YBCO is deposited by metallo-organic chemical vapor deposition (MOCVD) on these substrates. In the recent years, impressive progress has been made in the manufacturing of long lengths of YBCO coated conductors processed by using both the RABiTSTM substrates as well as IBAD substrates [6, 7]. Such long-length coated conductors are needed to make coils for rotating machinery and cables for electrical transmission. However, in high magnetic field applications such as MRI (Magnetic Resonance Imaging), SMES (Superconducting Magnetic Energy Storage), superconducting magnets and generators, etc., high J_c at high magnetic fields needs to be maintained. In the absence of flux pinning centers in the coated conductors, the magnetic flux lines will move due to Lorentz forces acting upon them at high fields. This motion causes dissipation, and losses will occur as a result. This lowers the J_c in coated conductors. Hence, it is important to incorporate flux pinning centers into coated conductors to improve the high-field J_c performance.

In addition to increasing the J_c , it is of importance to increase the J_e , the engineering critical current density. J_e is determined by dividing the critical current of a coated conductor (I_c) with the entire cross-section of a wire, including the thickness of the substrate, buffer layers, and metallic stabilizers, as well as the YBCO layer. The higher the J_c of a superconductor, the higher the resulting J_e of the coated conductor would be for similar thickness of buffers and substrate. Higher J_e conductors reduce the size of coils needed in the applications, and less of the superconductor material will be used, thereby reducing the total material and processing costs of the coils. Increasing J_e is also important in reducing the cost, size, and weight of coated conductors. The size and weight is of interest for airborne applications such as megawatt generators in future military aircraft [8]. Improvements to the J_e and other superconducting properties of YBCO will ultimately enable the U.S. Air Force to deploy more compact and lightweight power devices with higher energy densities and less cryogenic burden.

Another problem faced with the coated conductor is the quench and instability of a coil winding during the operation. Local overheating will trigger normal zone propagation in the coil, quickly resulting in a quench and the attendant rapid boil-off of the liquid nitrogen, which can

subsequently damage the coil. The lower the operating current density of the coil, the less likely the conductor will experience an incidence of quench. Hence, it is desirable to increase the J_c of coated conductors so that the coils can be run at reduced relative ratio of operating current density to critical current density level, in order to avoid the occurrences of quench and still be able to meet the required operating current levels.

One way to increase the J_c in coated conductors is to artificially introduce defects that pin the flux lines during the application of a magnetic field [9]. Since the coherence length of YBCO is ~ 4 nm at 77 K, the defects necessary to serve as effective pinning centers need to be very small. In addition, the pinning centers must not disrupt the texture of the bulk YBCO lattice deposited on top of the buffer layers nor lower the critical transition temperature (T_c) of the superconductors. Although a slight depression in T_c from 90 K may be tolerated since the operating temperature is 77 K (i.e., the boiling temperature of liquid nitrogen), significant depression in T_c will result in inferior properties at 77 K. The pinning center material needs to be economically introduced, and the method of introduction needs to be compatible with the processing method of choice. It is further beneficial if the pinning centers can be introduced during the YBCO growth as opposed to during post deposition processing.

In the present report, recent progress made to improve the flux pinning through introduction of various pinning centers is presented. Initially transport critical current density of YBCO+BaSnO₃ (BSO) films and magnetic field dependence was investigated. Then the effects of varying amounts of BSO content was studied by using premixed targets. Thick YBCO+BSO films were processed by using 30° sector target as well as pre-mixed target to investigate if nanocolumns would maintain the J_c in thick films.

1.2. Experimental

1.2.1. Pulsed laser deposition (PLD)

Flux pinning studies are done using samples made by pulsed laser deposition (PLD) method. Briefly, PLD is a physical vapor deposition technique in which an excimer laser is typically used to ablate the target in several short duration pulses, and the evaporated material is made to condense on to a substrate heated to different temperatures. By using optimum temperatures of ambience, pressure, laser energy, substrate temperature, substrate-to-heater distance, and selection of the substrate materials, excellent quality YBCO films can be made. The targets used in PLD for flux pinning studies were of the following types: (1) pre-mixed targets and (2) sector targets.

1.2.2. Pre-mixed targets

YBCO+BSO [10] films were deposited by using a pre-mixed target consisting of BSO second-phase additions and YBCO, which was mixed together in powder form prior to sintering of the final target. To study the effects of a systematic increase of BSO pinning material content in YBCO films, targets were mixed in powder form with the proper ratio of BSO pinning material to bulk YBCO. In this study, different by-weight amounts of YBCO and BSO powders were mixed to make final target compositions with 2, 4, 10, and 20 mol% BSO in YBCO. To make the target, initially the powders were well-mixed in a mortar and pestle to obtain homogeneous mixtures, and then disks with the dimensions of 1 in. diameter and 1/4 in. thickness were pressed

using a hydraulic press. These disks were sintered at 920 °C for 170 h in air to get a final density > 90% of the theoretical density.

1.2.3. Sectored target

A special pulsed laser ablation YBCO target with second phase material sector such as Y_2BaCuO_5 (Y211) or BaSnO_3 (BSO) was first used to make YBCO films nanoparticle pinning centers [11-12]. A thin sector piece ($\sim 30^\circ$) cut from a disc is attached onto the top surface of a YBCO target. As the target is rotated (at a speed of 15 – 20 rpm), the target is ablated at an approximate ratio of 11 pulses of YBCO to one pulse of the sector, resulting in the growth of a nanocomposite film. More than one sector can be used to deposit films with more than two different compositions in films. The second phase content can be varied by varying the sector size. It is also possible to use different sectors while maintaining a single YBCO target. In this way the effect of second phases in films without changing the matrix composition can be investigated. A particular advantage of this approach over a pre-mixed target approach is that any possible chemical reactions between the pinning material and the YBCO in the target preparation stage are prevented as the second phase is physically separated from YBCO. The reaction time between the pinning material and YBCO coatings is reduced as the growth of the nanoparticles occurs simultaneously with the growth of YBCO film. Also, nanoparticles are introduced in a non-layered fashion in contrast to an alternating target approach. The dual sector deposition approach provides a quick evaluation of different compositions by changing the second phase sector while maintaining the same YBCO target, thus avoiding differences that might be partially ascribed to differences in the batch of YBCO powder used.

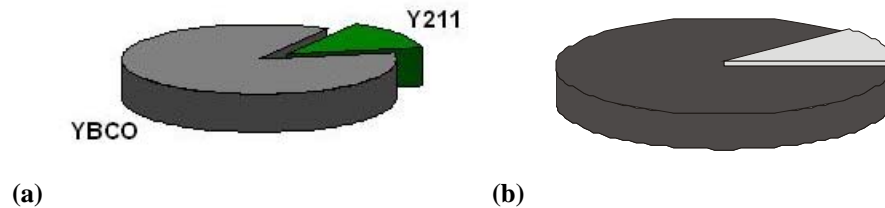


Figure 1.1. Schematic diagram of a PLD YBCO target with a small sector of a second phase such as Y_2BaCuO_5 or BaSnO_3 as an (a) inserted type or (b) thin sector on top type

1.2.4. Sample preparation and characterization

Commercially available $\text{YBa}_2\text{Cu}_3\text{O}_{7-x}$ powders (Nexans) and BaSnO_3 powders (Cerac) were used to make the targets to deposit YBCO + BSO films with different compositions. The starting powders of BaSnO_3 were of a -325 mesh size. No nanomaterials of BSO were used to make these targets. Different amounts of the YBCO and BSO powders were mixed to make the targets with 2, 4, 10, and 20 mol% BSO in YBCO. The powders were well mixed in a mortar and pestle to obtain homogeneous mixtures. Disks with the dimensions of 1 in. diameter and $\frac{1}{4}$ in. thickness were pressed using a hydraulic press. These disks were sintered at 920 °C for 170 h in air to get a final density > 90% of the theoretical density.

To process thin film samples, a Lambda Physik excimer laser (Model No. LPX 300, wavelength (λ) = 248 nm, KrF) was used to deposit the films at 780 °C using a 4 Hz repetition rate, 2 J/cm² energy density, 300 mTorr of oxygen pressure in a Neocera PLD chamber. Substrate to the target distance was maintained at nearly 6 cm for all the depositions. All the films were oxygen annealed at 500 °C for 30 min in 600 Torr of oxygen pressure inside the chamber after the deposition was completed. Films of different thicknesses were deposited on LaAlO₃ (100) or buffered metallic substrates, and the thickness was varied by increasing the length of deposition.

The film microstructure was studied using a SIRION (FEI) ultra high resolution field emission scanning electron microscope (FE-SEM). The critical transition temperature (T_c) was measured by AC susceptibility method. The magnetization J_c was measured using the hysteresis loops data acquired from a Quantum Design PPMS vibrating sample magnetometer (VSM) in H//c orientation. The Bean's model ($J_c = 20 \times \Delta M / [a (1-a/3b)]$), in which ΔM is the hysteresis in emu·cm⁻³ and a and b are the sample dimensions, was used to estimate J_c . The J_{ct} of the samples were measured by using a four-probe transport current measurement method. Samples were prepared with 1 – 2 mm wide bridges using either laser ablation or chemical etch methods. The J_{ct} angular dependence was measured by rotating the sample through a range of -20° to 120° about the sample normal in an applied magnetic field of 1 – 5 T at 77 K. The J_{ct} data was collected every 2° near H//c and H//ab orientations and every 4° elsewhere. A voltage criterion of 1 μ V/cm was used in the I-V curves obtained at various angles to determine the I_c and calculate J_c .

The thickness of all the samples was measured using a KLA Tencor profilometer and verified with cross-sectional SEM. The cross-section transmission electron microscopy (TEM) samples were prepared through a conventional TEM sample preparation technique involving gluing, grinding, polishing, and ion milling. The detailed microstructure of these samples was characterized by TEM and high resolution TEM using a JEOL-2010 analytical electron microscope with point-to-point resolution of 0.21 nm. An x-ray diffractometer was used to obtain $\theta - 2\theta$ scans on the films to verify the film orientation and composition of the YBCO + BSO films.

1.3. Results and Discussion

1.3.1. YBCO + Y₂BaCuO₅ and YBCO+ BaSnO₃ films prepared by using a sector PLD target approach

Figure 1.2 shows the magnetization J_c data (H//c) of YBCO+Y211 and YBCO+BSO films measured at various temperatures. It can be seen that the J_c of YBCO+Y211 films is lower than YBCO+BSO films at all the measured temperatures of 77, 65, and 40 K. However, it should be noted that YBCO+Y211 films had better J_c than regular YBCO films at these temperatures, but they do not have J_c as good as that of YBCO+BSO. The improvement in J_c is significant in YBCO+BSO films at higher fields, possibly due to the increase in the irreversibility field as well as improved flux pinning.

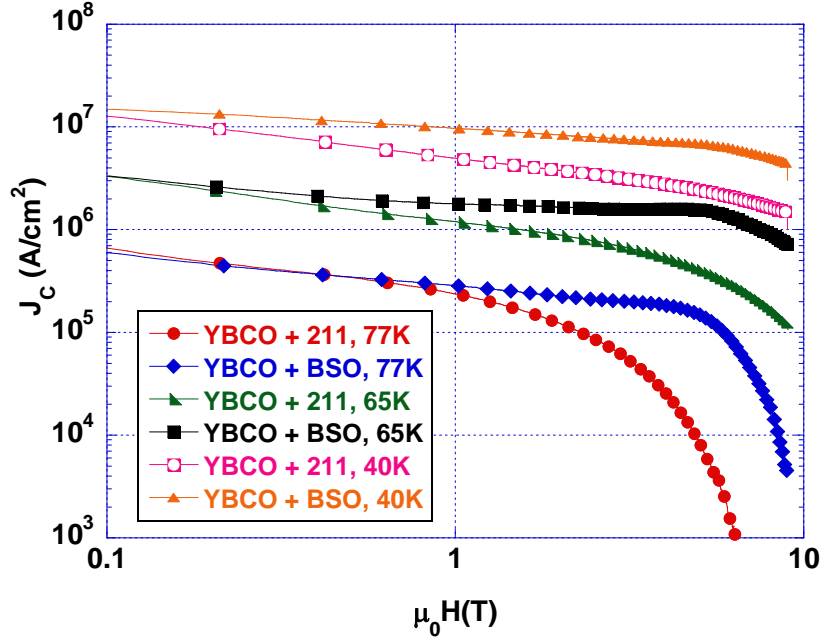


Figure 1.2. Magnetization J_c data ($H//c$) of YBCO+Y211 and YBCO+BSO films made by sectored target method

Figure 1.3 shows a plan view SEM micrograph and a cross-sectional TEM micrograph of YBCO+Y211 films. Good dispersion of Y211 nanoparticles in the YBCO matrix can be seen. The bright particles in the SEM image and dark particles in the TEM image correspond to the Y211 phase. The nanoparticles seem to be present throughout the thickness of the films. In addition to the nanoparticles, the YBCO+Y211 films also had YBCO plane buckling due to the presence of these nanoparticles as evidenced by the cross-sectional TEM images published elsewhere [13]. In contrast to the YBCO+Y211 films, the YBCO+BSO films were found to have many BSO nanocolumns, as shown in a cross-sectional TEM image in Figure 1.4 (a) as well as in reference [14]. In a plan view image, these nanocolumns appear to be nanoparticles, as shown in Figure 1.4 (b). It can be seen that the nanorods are uniform in diameter and are self-organized to be equidistant from each other. It is thought that a phase separation during the deposition and self-assembly are responsible for the nanorod growth. Strain due to lattice mismatch, texture and deposition conditions seem to help grow the nanocolumns in a certain constant diameter. Since BSO and YBCO are both perovskites, they tend to grow along the c -axis perpendicular to LAO substrate, and thus resulted in the BSO nanocolumnar growth in a matrix of YBCO. Due to these nanocolumns, a significant increase in J_c in $H//c$ orientation was observed, as the magnetic flux line interaction with the nanocolumns is expected to be at maximum in this orientation. The nanorod diameter was found to be around 10 – 11 nm, and the density was estimated to be $3 \times 10^{11}/\text{cm}^2$. The normalized angular dependence of transport current data at 1 T shows that a peak only in YBCO+BSO samples is found at $H//c$, indicating the contribution of flux pinning due to nanocolumns in YBCO+BSO films in this direction.

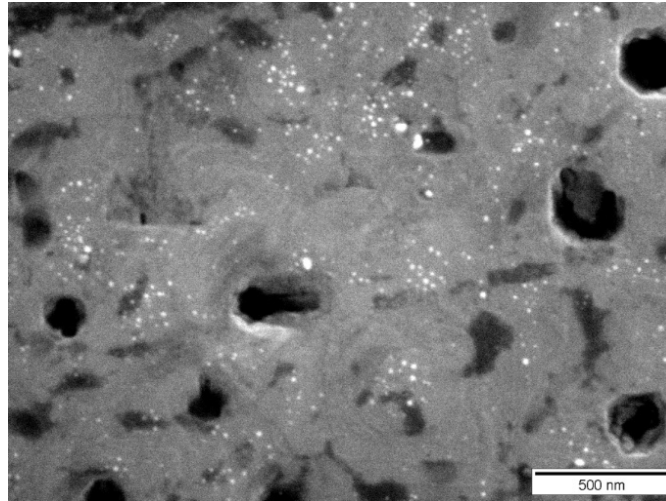


Figure 1.3 (a). SEM micrograph of YBCO+Y211 film made by sectored target approach



Figure 1.3 (b). Cross-sectional TEM micrograph of YBCO+Y211 film made by sectored target approach

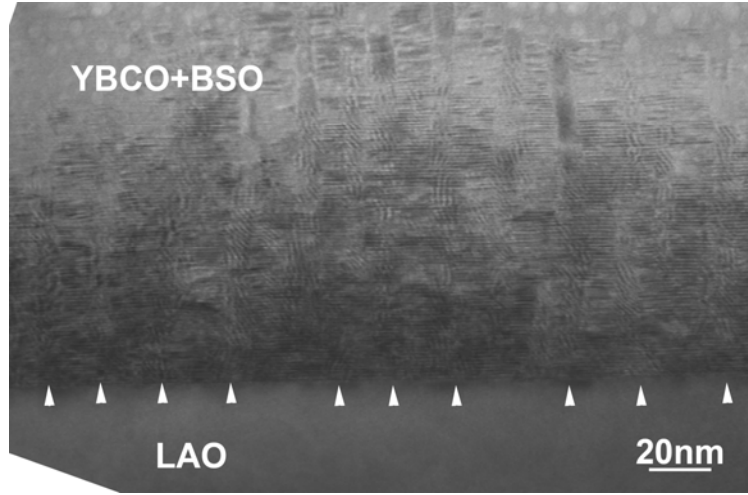


Figure 1.4 (a). Cross-sectional TEM micrograph of a YBCO+BSO film made by sectored target approach

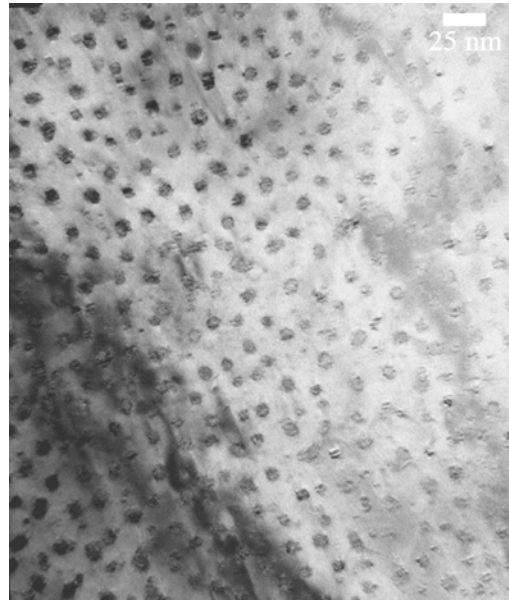


Figure 1.4 (b). Plan view TEM micrograph of a YBCO+BSO film made by sectored target approach

1.3.2. Transport critical current density YBCO+BSO films

Figure 1.5 shows the normalized J_{ct} data of a YBCO+BSO sample on a LaAlO_3 substrate in an applied magnetic field of 0 to 12 T. Even though the J_{ct} at self field was found to be around 1 MA/cm^2 , the J_{ct} in the applied magnetic fields was found to be enhanced considerably. The increased J_{ct} in these films is believed to be due to the presence of 10 nm size BSO nanocolumns that were formed in the YBCO films (to be discussed later).

It can be seen from Figure 1.5 that the rate of fall in J_{ct} with the applied magnetic field in YBCO+BSO samples was very low. To illustrate this more clearly, alpha (α) measurements at low magnetic fields were taken using a vibrating sample magnetometer on YBCO+BSO and regular YBCO samples in the region where J_c is proportional to $B^{-\alpha}$ where B is the magnetic field. The temperature dependence of α over a temperature range of 20 – 77 K was measured and is presented in Figure 1.6 for a YBCO control sample and for two of the YBCO+BSO samples. It can be seen that the typical value for α for the YBCO control sample is 0.5 and is temperature-independent. However, for the YBCO+BSO samples, α was found to be around 0.1 at low temperatures and it rises slowly to 0.3 at higher temperatures giving an average value of 0.2 in the temperature range of 20 – 77 K for YBCO+BSO samples. A low α value indicates that J_c drops with the magnetic field at a much lower rate. Such low values of α at 77 K were also reported in other pinned YBCO samples with BZO nanoparticles [15], corroborating the data of low α value for these highly pinned YBCO+BSO samples.

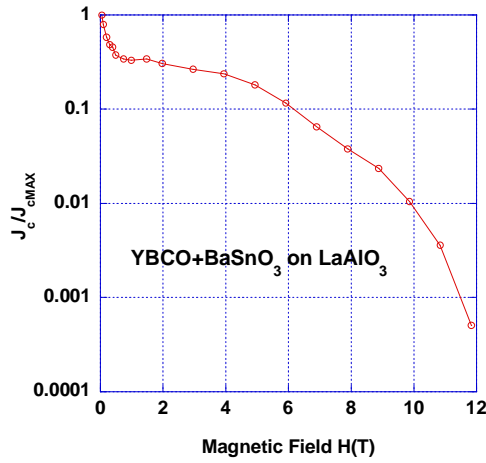


Figure 1.5. Normalized plot of transport critical current density (J_{ct}) in applied magnetic field of a YBCO+BSO sample on LaAlO_3 substrate at 77 K

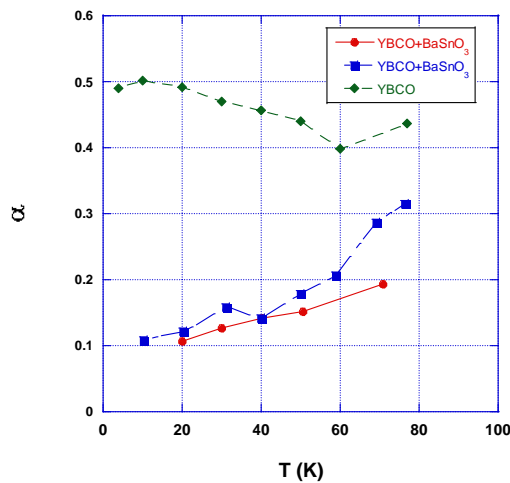


Figure 1.6. Temperature dependence of α values for a control YBCO and YBCO+BSO samples

Variations in J_{ct} with the applied magnetic field orientation to the sample normal at 77 K of a YBCO+BSO sample on a LaAlO_3 substrate is shown in Figure 1.7. The angular dependence at various applied fields of 1, 3, and 5 T were compared. It can be seen that the J_{ct} in H//c orientation is higher than J_{ct} in H//ab orientation in all of these applied fields. The presence of peaks in the J_{ct} in H//c or H//ab orientation are commonly attributed due to the presence of correlated defects [16-17]. Evidence of the c-axis correlated defects in YBCO+BSO is provided in more detail later during the TEM analyses.

To compare the relative increase in J_{ct} in H//c as compared to J_{ct} in H//ab in YBCO+BSO films, normalized J_{ct} values with respect to J_{ct} in H//ab data in various orientations to the sample normal are presented in Figure 1.8. In comparison, data taken from a plain YBCO film on a buffered biaxially textured metallic Ni-W substrate is presented along with YBCO+BSO film. As expected, the J_{ct} in H//c orientation is observed to be lower than J_{ct} in H//ab in regular YBCO samples, however, a peak in YBCO+BSO samples in H//c orientation is clearly present similar to the data shown in Figure 1.8. In this particular YBCO+BSO sample, the ratio of the J_{ct} in H//c to J_{ct} in H//ab is about 1.3, whereas it is only 0.3 for regular YBCO.

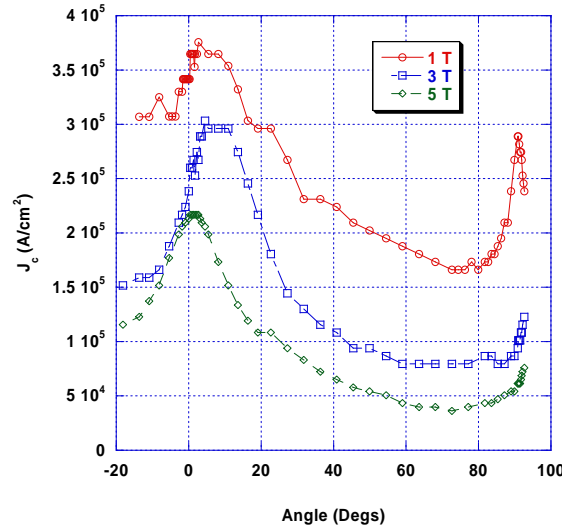


Figure 1.7. Angular dependence of J_{ct} values of YBCO+BSO sample on a LaAlO_3 substrate at various applied fields of 1, 3 and 5 T at 77 K

Angular dependence of J_{ct} values of YBCO+BSO samples deposited on a buffered Ni-W metallic substrate were also measured to see if the improvements seen on LaAlO_3 can also be observed on the more practical buffered metallic substrates. Figure 1.9 shows the J_{ct} values measured at 77 K in an applied field of 1 T. It can be seen that the J_{ct} in the H//c orientation is increased compared to the J_{ct} in the H//ab orientation similar to the behavior observed in the YBCO+BSO samples on LaAlO_3 substrates. This illustrates that the angular dependence with YBCO+BSO is independent of the substrate used and are directly caused by the nanoparticles and/or the defects created by them. It can be seen that J_{ct} in H//c orientation in the sample is found to be slightly higher than J_{ct} in H//c in YBCO+BSO sample on LaAlO_3 substrate shown in Figure 1.7. The T_c of the samples processed on the metallic substrates (90 K) was found to be slightly higher than the films processed on LaAlO_3 substrates (88 K). The slight increase in J_c could probably be due to the T_c differences. However, the J_{ct} behavior in the applied magnetic

field in YBCO+BSO films, such as the increase in the H//c orientation over H//ab orientation, is similar irrespective of the substrates used.

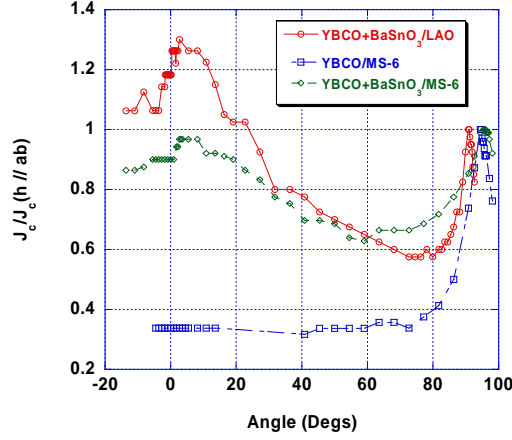


Figure 1.8. Normalized J_{ct} with respect to J_{ct} in H//ab for a YBCO+BSO sample as compared to regular YBCO at 77 K

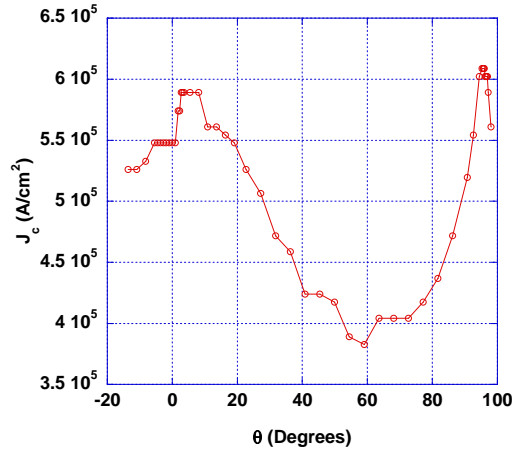


Figure 1.9. Angular dependence of J_{ct} for a YBCO+BSO film on a buffered metallic Ni-W substrate in an applied magnetic field of 1 T at 77 K

Microstructural characterizations were carried out to understand the observed J_{ct} angular dependence. Figure 1.10 shows an SEM micrograph of a YBCO+BSO film on a buffered metallic substrate. The micrograph shows the presence of high density of nanoparticles (~10 nm bright particles) in a YBCO+BSO sample. It is known that as the applied magnetic field is increased, the magnetic flux line density increases in YBCO and so accordingly the number density of pinning centers required to interact with the magnetic flux lines also needs to be high for high field applications. The number density of pinning centers in the present sample was estimated to be $\sim 3.5 \times 10^{11}/\text{cm}^2$ from the SEM pictures, which corresponds to a matching field of 6 – 7 T. This implies that at high magnetic field > 5 T the interaction between the flux lines and the particles was expected to be optimal.

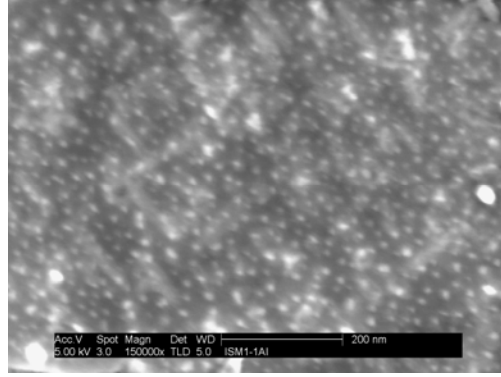


Figure 1.10. Scanning electron micrograph of an YBCO+BSO sample on a buffered Ni-W metallic substrate

In cross-sectional TEM images of the YBCO+BSO samples on LaAlO_3 substrates, high quality epitaxial growth of YBCO/BSO nanocomposites were observed. Figure 1.11 shows the cross-sectional bright field TEM image obtained from one of the samples. The presence of nanocolumns extending the entire thickness of the films can be clearly seen. The average spacing between the nanocolumns is around $\sim 20 - 30$ nm. In the literature, nanorod structures were observed in YBCO+BZO or YBCO+YSZ films made using PLD of pre-mixed targets [15, 18]. In the present work, without using a pre-mixed target but using only a dual sector target, similar microstructural features were obtained. Also noteworthy, the columns seem to be formed as continuous rods as opposed to a structure of self assembled nanodots as indicated for other YBCO+BZO samples [15]. The corresponding selected area diffraction pattern (shown in Figure 1.11) clearly shows the high quality epitaxial growth of YBCO/BSO on LAO substrate. The diffraction dots from BSO can be clearly seen and indexed to be BSO (002) and (020), correspondingly (marked in Figure 1.11). The epitaxial relations are determined to be YBCO (003)//LAO (001)//(BSO (002) and YBCO (020)//LAO (020)//BSO (020).

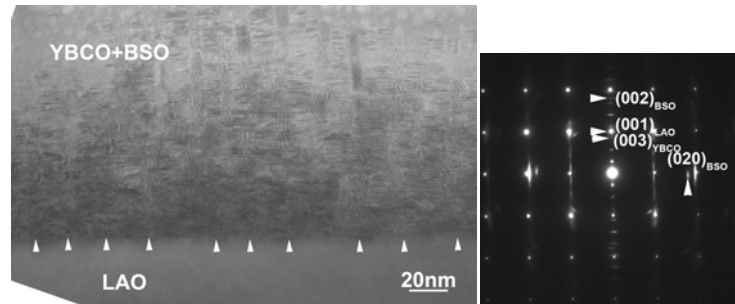


Figure 1.11. Cross-sectional TEM image of an YBCO+BSO sample on a LaAlO_3 substrate with BSO particles identified in the selected area diffraction pattern

The fringe or moiré patterns in Figure 1.11 around the rods are created due to the overlap of the YBCO and BSO lattices and their lattice mismatch. In order to reveal the detailed defect information at the interface of the YBCO/BSO, we conducted a detailed high resolution TEM (HRTEM) study on these cross-section samples. A high quality epitaxial growth of the YBCO/BSO nanocomposite was observed as shown in the HRTEM image given in Figure 1.12.

High density misfit dislocations and stacking faults generated at the interfaces of YBCO and BSO are shown in the corresponding Fast Fourier Transform (FFT) filtered image. The high density of these defects is strongly related to the high density of these BSO nanocolumns (spacing of ~ 20 nm), the large lattice mismatch between YBCO and BSO ($\sim 7\%$), and their vertical aligned orientation. From several cross-sectional images, the density of the misfit dislocations is estimated to be on the order of $1000/\mu\text{m}^2$. In the FFT image, it is clearly shown that the formation of the stacking faults is closely related to the generation of misfit dislocations. Therefore, the density of the stacking faults is on the same order of magnitude as that of the misfit dislocations. The presence of these high density columnar defects (nanocolumns) and the c-axis correlated defects (misfit dislocations and stacking faults) could all contribute to enhancing the J_c in the H//c orientation.

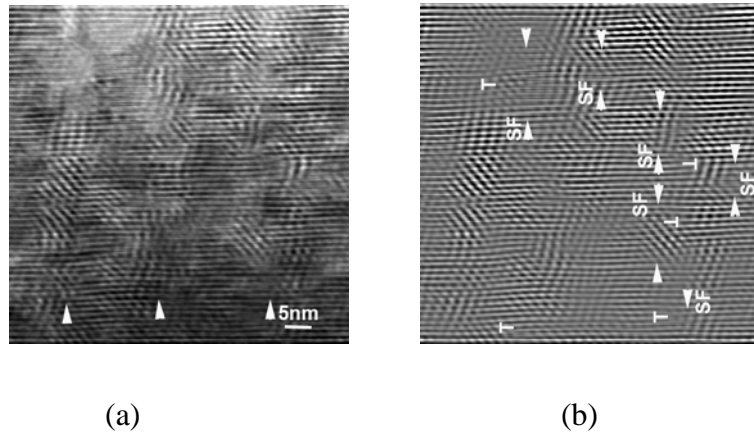


Figure 1.12. (a) High resolution TEM image of an YBCO+BSO film showing high density of dislocations and stacking faults; (b) FFT filtered image showing the existence of high density of misfit dislocations and stacking faults at the YBCO/BSO interfaces

1.3.3. Current density and alpha value variations with temperature, and dual peaks in F_p plots of YBCO+BSO samples

The alpha values at 77 K were found to be small for YBCO+BSO films, as compared to YBCO or YBCO+Y211. Typically, for undoped YBCO an alpha value of 0.5 at 77 K is noted [19]. The alpha values of YBCO+Y211 samples were found to be around 0.4 – 0.5, whereas for YBCO+BSO films they were found to be 0.2 – 0.3. In addition, alpha values of YBCO+BSO samples were found to decrease with the temperature to a value as low as 0.1 at 20 K, as shown in Figure 1.13.

The J_c value variations with the temperature for YBCO+BSO films are shown in Figure 1.14. This figure has additional J_c data taken at temperatures other than those shown in Figure 1.14, as some applications may need operation at lower temperatures. As expected, the J_c continues to increase as the temperature was lowered and was found to be higher than YBCO or YBCO+Y211 films. It was found that the flux pinning force increases in YBCO+BSO films as compared to YBCO or YBCO+Y211 films, with values as high as 18 GN/cm^3 at 77 K for a 300 nm thick film as shown in Figure 1.15. Flux pinning force maxima ($F_{p \text{ max}}$) higher than this value

are possible in thicker films, as discussed later. It can be seen that the peak shifts to higher fields, and also sometimes clearly discernable dual peaks were also observed in YBCO+BSO samples. A shoulder in low fields followed by a peak at the higher fields was observed. Such dual peaks were not observed in YBCO or YBCO+Y211 samples. It was observed that the peak intensity is lowered as the peak shifts to higher fields in YBCO+BSO samples. The presence of dual peaks can be ascribed to dual pinning mechanisms that may be operative, as discussed in reference [20].

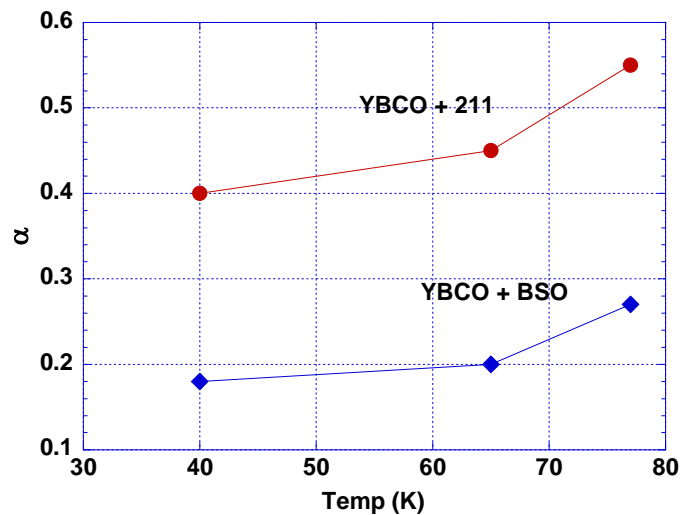


Figure 1.13. Alpha values of YBCO+Y211 and YBCO+BSO films at different temperatures

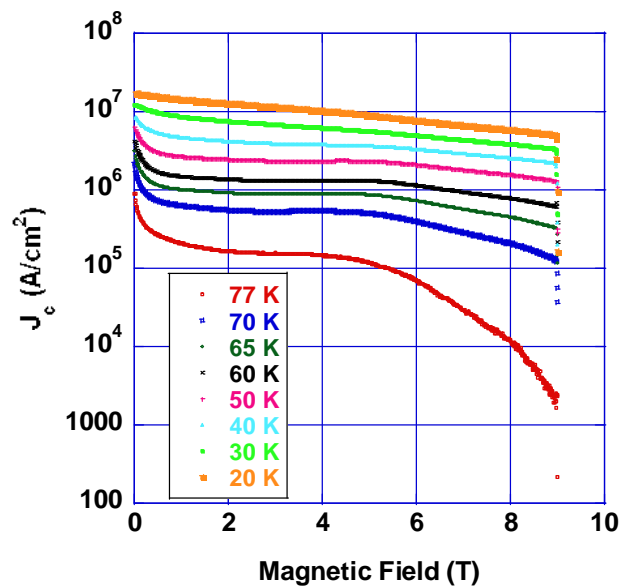


Figure 1.14. Magnetization J_c of YBCO+BSO films at various temperatures

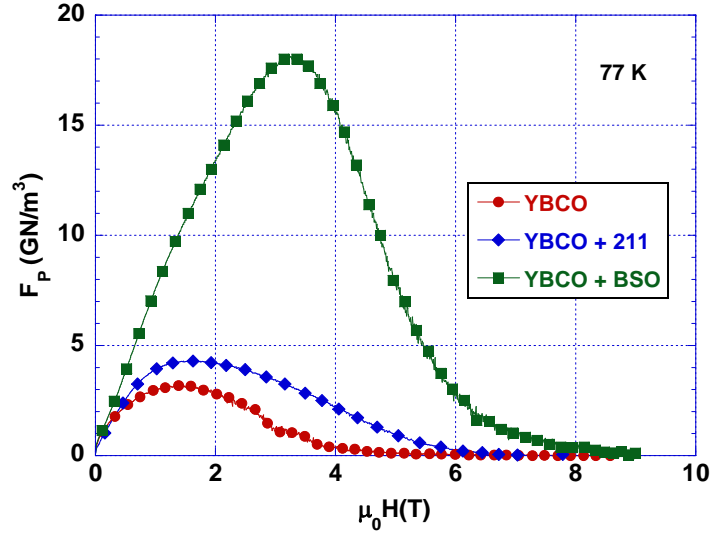


Figure 1.15. F_p plots of YBCO+BSO, YBCO+211 and YBCO films at 77 K

1.3.4. YBCO+BSO films with varying amounts of BSO content

Figure 1.16 shows the $\theta - 2\theta$ scan patterns (normalized with the highest peak intensity of each sample) of different films processed in this study. It can be seen that all the films are c-axis oriented showing only YBCO (00 l) peaks. Peaks corresponding to only the BSO (200) reflections were noted at $\sim 44^\circ$, indicating that BSO is also well oriented in the films. In addition, the intensity of the BSO (200) peaks increased as the mol% of BSO in the films was increased, indicating that the (200) orientation was maintained as the BSO content increased. No additional peaks corresponding to any other phases were observed, indicating that the BSO is probably inert in YBCO at these processing conditions.

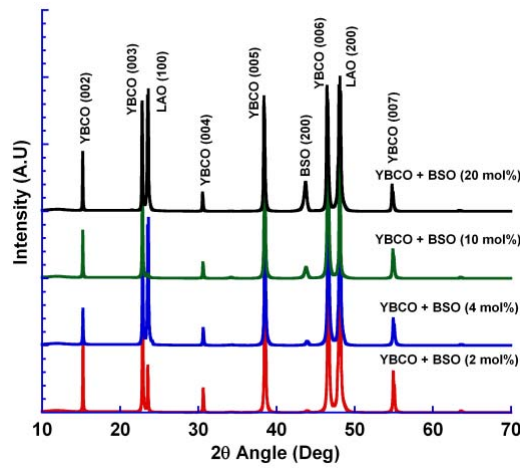


Figure 1.16. X-ray $\theta - 2\theta$ scan patterns scans of various YBCO+BSO films

The T_c values of different YBCO+BSO films are plotted in Figure 1.17 as a function of BSO content. It can be seen that a high T_c of ~ 92 K was found for the YBCO+2 mol % BSO films, which is similar to plain YBCO films; however, as the content of BSO was increased, a gradual decrease in T_c was observed. Even though the films had 20 mol% BSO content, they still showed a reasonably high T_c of 87 K. These results are in stark contrast to BaZrO₃ (BZO) additions to YBCO films where a significant drop in T_c was observed [21] when the BZO content was increased. It is possible that some Sn diffusion into YBCO films can occur during PLD. It has been shown previously that a drop in T_c can be expected if Sn is substituted for Cu sites in bulk YBCO [22]. The observed minor drop in T_c may be attributed to these Sn substitutions or to the total strain in the YBCO lattice due to a lattice mismatch between BSO and YBCO that may increase as the BSO content is increased; however, it appears that these effects are limited and do not reduce the T_c significantly below 87 K even up to 20 mol% of BSO additions. It should be noted that even though the T_c in YBCO + 20 mol% BSO films is lowered to 87 K, it is still much higher than the operating temperature of many applications (77 or 65 K) and the effect of T_c reduction on J_c seems to be minimal at these temperatures, as will be discussed later.

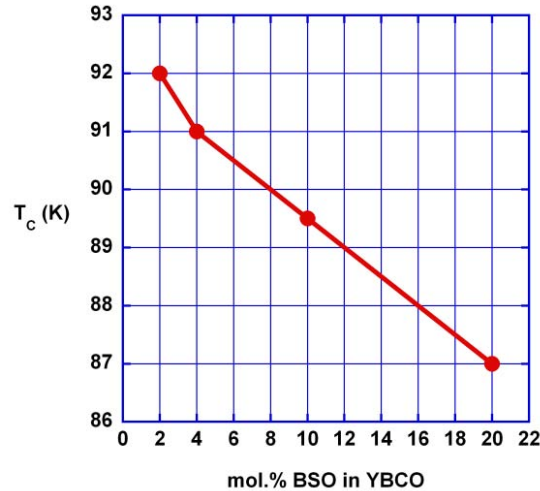


Figure 1.17. T_c variation in YBCO+BSO films with varying BSO content

Figure 1.18 shows the magnetization J_c of YBCO+BSO films with different amounts of BSO at 77 and 65 K as a function of magnetic field in the H//c orientation. It can be seen that the YBCO+BSO films show more than an order of magnitude improvement over regular YBCO films at fields > 4 T and nearly 2 orders of magnitude improvement at even higher fields > 6 T. Even at lower fields (< 2 T), the improvement is significant in low doping levels of BSO (e.g. YBCO+10 mol% BSO) samples. At low fields, the amount of BSO in the films does not participate in the flux pinning enhancement (due to a lower density of fluxons), and detracts from the overall superconducting volume of the film. For the YBCO+20 mol% BSO films, the observed decrease in J_c below 1 T is due at least in part to this contribution of non-superconducting volume of BSO in the films. However, due to a large number of fluxons, the interaction between the BSO nanocolumns (to be discussed later) and fluxons is more fully utilized and results in enhanced pinning as evidenced by the significantly increased J_c at high fields. Transport current J_c measurements taken on one of the samples (YBCO+20 mol %BSO)

correlated well with the magnetization J_c data presented here especially at high fields. However, the magnetization J_c in low fields ($< 4\text{ T}$) was found to be lower than the transport J_c for the reasons explained above.

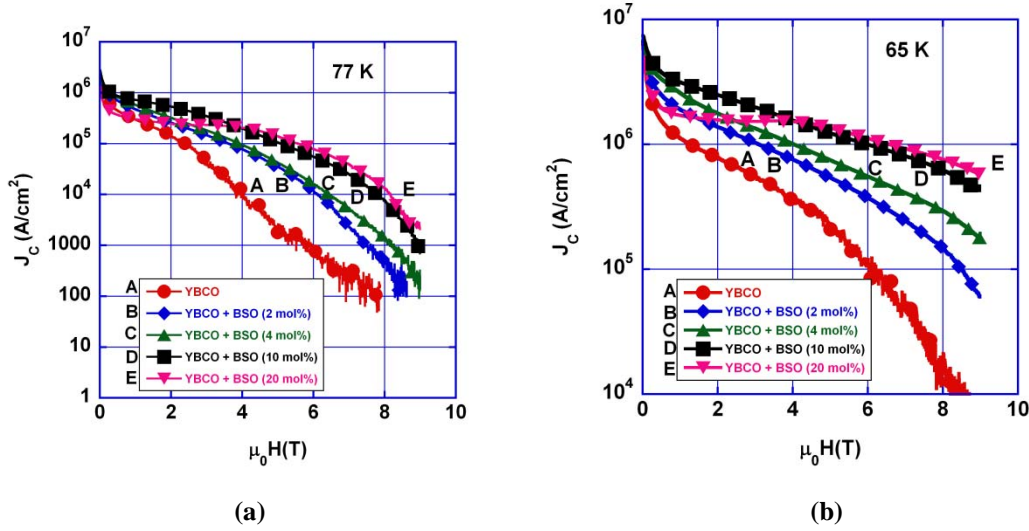


Figure 1.18. Magnetization J_c of YBCO+BSO films as a function of applied magnetic field with varying amounts of BSO content as compared to regular YBCO (a) at 77 K (b) at 65 K

Figure 1.19 shows the 77 K J_c data plotted for YBCO samples with different BSO concentrations at different magnetic fields (1 – 7 T) to more clearly depict the effects of BSO content on the J_c in these films. It can be clearly seen that the effect of BSO content on J_c seems to depend upon the field of measurement. For example, self-field J_c , or J_c at low fields ($< 3\text{ T}$), decreases slightly by increasing the BSO content from 2 mol% to 20 mol%. However, with the same change in composition, the J_c was found to increase significantly at higher fields such as 5 or 7 T. It should be noted that all the films show improvement over regular YBCO data (shown as a sample of YBCO+BSO, 0 mol%, Figure 1.19) at high fields. The optimum level seems to be 10 mol% BSO for the applications below 3 T. For higher field applications, a higher level may be suitable, although the improvements in J_c seem to indicate that it could approach a plateau above 20 mol%. However, it should be noted that higher amounts could further reduce the low-field J_c data even though slightly higher J_c at high fields may be obtained. In the YBCO +BSO films with higher BSO amounts ($\sim 30\text{ mol\%}$) prepared with a 30° BSO wedge, such degradation in low fields was observed even though high field performance was enhanced. So it appears that the optimum BSO content in YBCO depends upon the intended application. YBCO+10 mol% BSO seems to have optimum performance in the magnetic field range of 0 – 4 T and YBCO+20 mol% seems to be optimum in 4 – 9 T range.

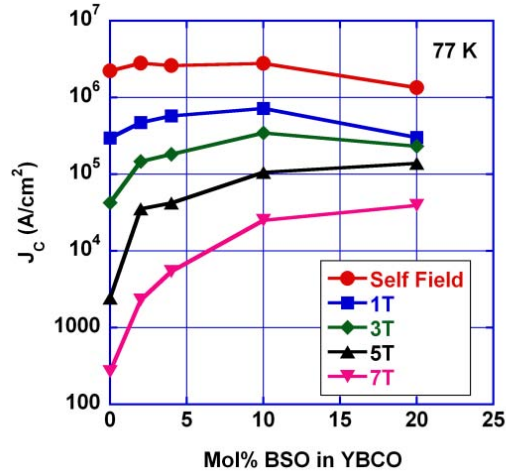


Figure 1.19. Magnetization J_c of YBCO+BSO films as a function of the BSO content at various magnetic fields at 77 K

The YBCO+10 mol% BSO films had a low α (alpha) value of 0.36 and YBCO+20 mol% BSO films had an α value of 0.38 at 77 K as compared to a regular YBCO film that usually has an α value of 0.5 [18]. However, YBCO+2 mol % BSO had an α value close to 0.5. A lower α value indicates a less rapid decrease in J_c with an increase in magnetic field. Similar low α values were also noted in other YBCO films with nanocolumns and the present trend of lowered α with increased nanocolumns is consistent with improved pinning [15].

Figure 1.20 shows the pinning force F_p vs. B plots at 77 and 65 K. Of particular interest is that the F_p peak maximum (F_{pmax}) continues to increase in value as the BSO content is increased at 65 K but only up to 10 mol% in the case of 77 K. In Figures 1.20 (b) and (d), the normalized F_p / F_{pmax} vs. magnetic field is plotted to show the shifts in the peak position. It can be seen that the peak position moves to higher fields as the BSO content is increased at both 65 and 77 K. The F_p peak in YBCO+20 mol% BSO occurs at as high as 4 T at 77 K. In addition, the overlapping dual peak structure become discernible in the F_p plots of YBCO+20 mol% BSO content at 77 K, similar to the plots seen in YBCO+BSO films containing higher BSO content [20]. The presence of the dual peak structure (where the composite overlapping dual peak structure has a main peak with a shoulder) in the F_p plots of YBCO+BSO with higher BSO content as shown in this work is reproducible from previous work and apparently is process independent, depending largely upon the amount of BSO content in the film. The presence of the dual peak structure and peak shifts in the F_p plots signify the potential fundamental changes in the pinning mechanisms that may be operative in the samples as the BSO content is increased, as previously discussed.

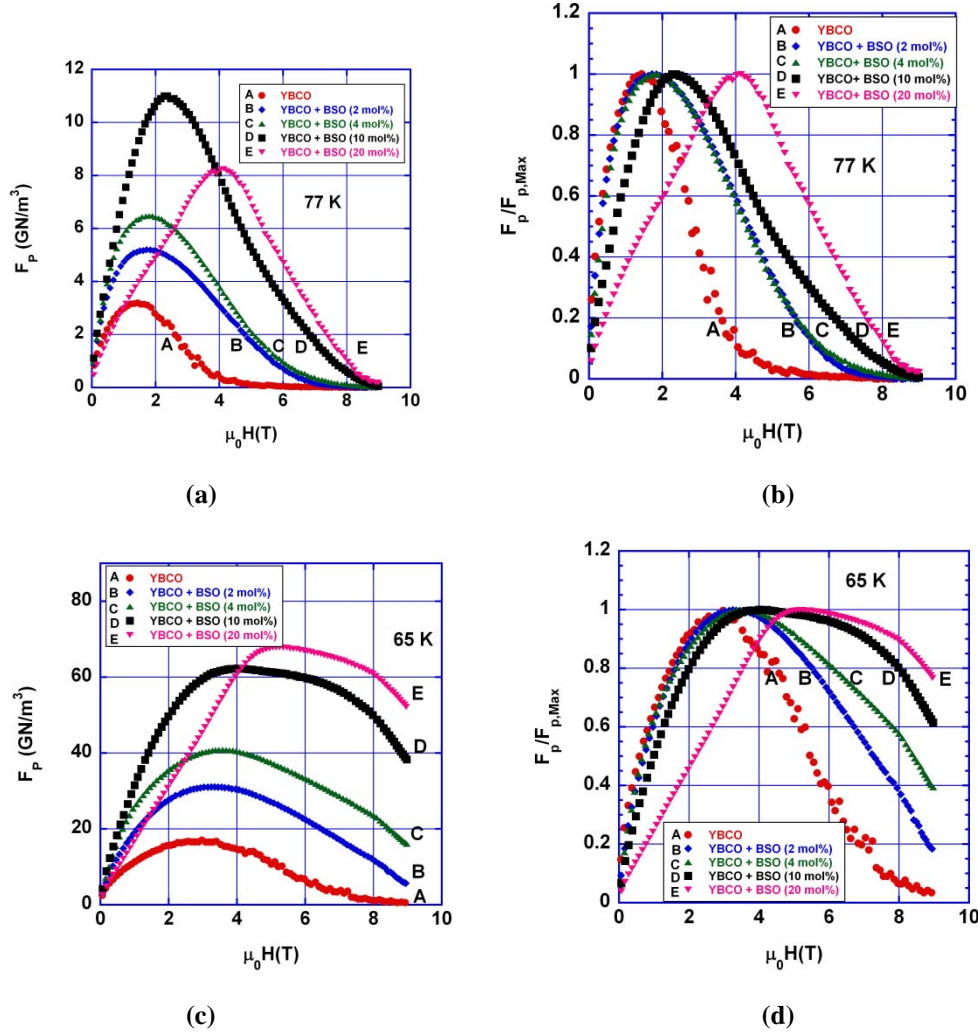


Figure 1.20. Flux pinning force (F_p) of different YBCO + BSO films (a) F_p at 77 K, (b) $F_p/F_{p, \text{max}}$ at 77 K, (c) F_p at 65 K, (d) $F_p/F_{p, \text{max}}$ at 65 K

In SEM characterization of the microstructures, the presence of 0.4 – 0.5 μm sized particles as well as thoroughly dispersed nanoparticles were observed in all the samples. Figure 1.21 shows SEM images of a YBCO+BSO (4 mol%) sample as an example. As the BSO content was increased, the number density of these nanoparticles as seen in the plan view SEM images increased. These nanoparticles could be BSO nanocolumns as seen by cross-sectional TEM images (discussed later) projected on a 2-D plane. The presence of the larger particles does occur at times in PLD films and is generally attributed to particle/grain transfer that happens from the target to the films. Typically, these large particles are not expected to participate in the flux pinning enhancement due to their large size as compared to coherence length of YBCO.

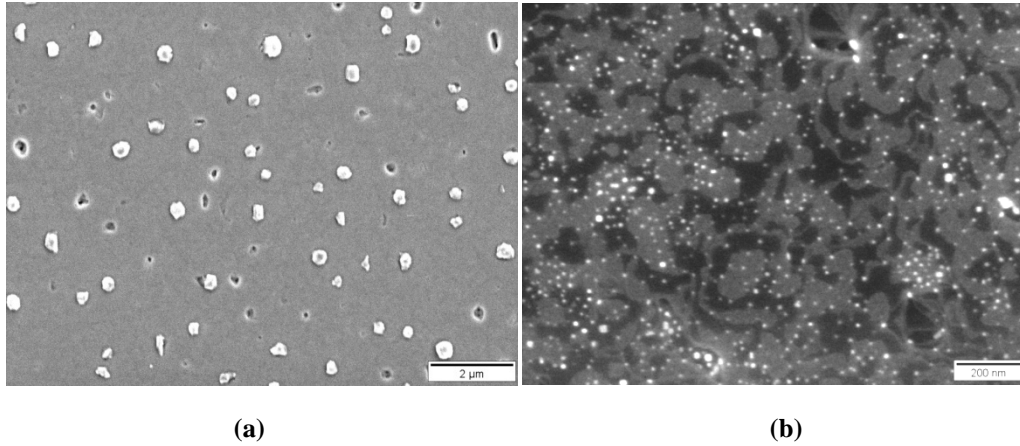
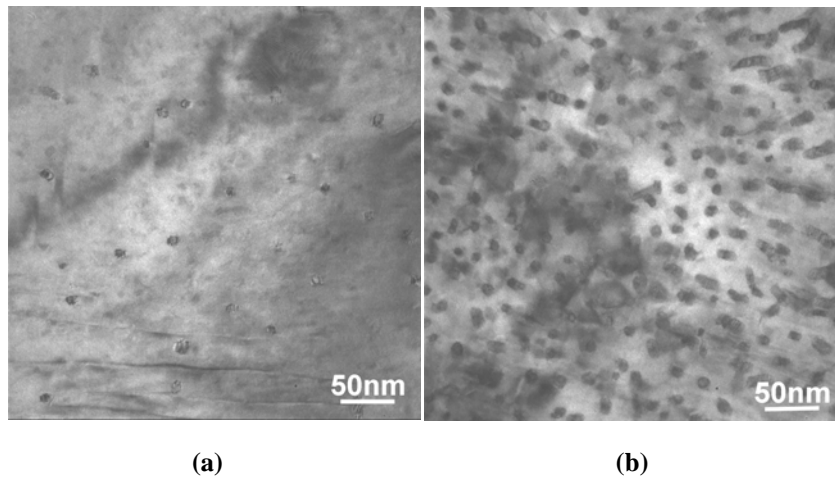


Figure 1.21. Scanning electron micrograph showing the BSO nanoparticles in a YBCO+4 mol% BSO sample: (a) low magnification micrograph showing large particles, and (b) high magnification micrograph showing nanoparticles in plan view

Figure 1.22 shows the TEM plan view and cross-sectional view images of different composition samples (YBCO with 2 and 20 mol% BSO). As the BSO content was increased, the density of the nanoparticles as seen in plan view also increased. In the cross-sectional TEM, well separated uniform diameter nanocolumns extended throughout the thickness of the films. It is possible that the nanocolumns seen in the cross-sectional view account for most of the nanoparticles observed in the plan view TEM or SEM. Due to the lattice mismatch between BSO and YBCO ($\sim 7.7\%$), Moiré patterns are observed in the microstructure. Selected area diffraction patterns taken from these nanocolumns confirmed that they are indeed BSO. The number density of these nanocolumns increased to as high as $1.5 \times 10^{11}/\text{cm}^2$ in YBCO+20 mol % BSO samples while the average diameter of the nanocolumns remained relatively constant at $\sim 7 - 8$ nm. The average spacing between them decreased from 50 to 20 nm as the BSO content was increased from 2 to 20 mol%. It should be noted that although no nanoparticle BSO was used in the target manufacture, the BSO nanocolumns were formed in the films. It is believed that the strain in the matrix of the YBCO favors such nucleation and growth of BSO nanocolumns.



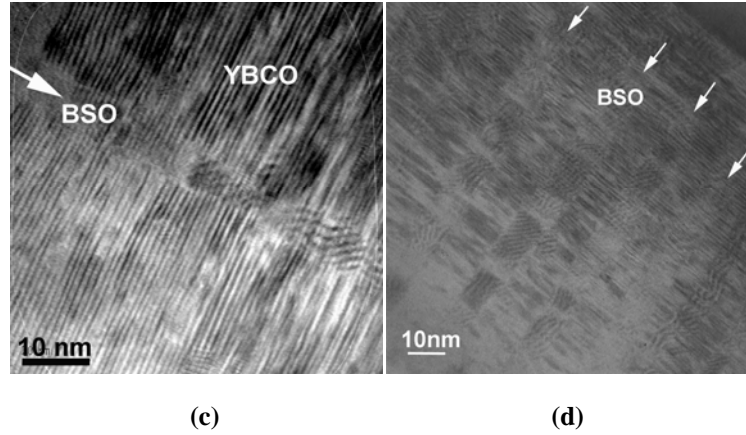


Figure 1.22. TEM images showing (a) YBCO+2 mol% BSO in plan view, (b) YBCO+20 mol% BSO in plan view, (c) YBCO+2 mol% BSO in cross-section view, and (d) YBCO+2 mol% BSO in cross-section view

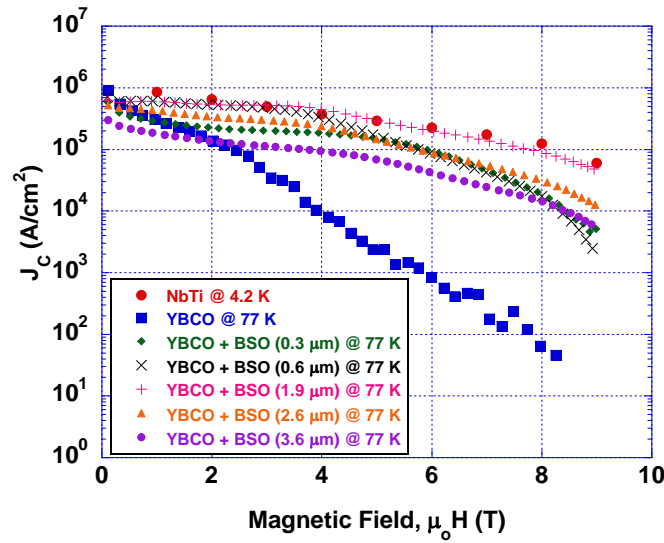
A one-to-one correlation with the microstructure consisting of the BSO nanocolumns and the J_c properties is clearly seen in the present study. An increase in the number density of the nanocolumns seems to help to increase the high field J_c . Local lattice mismatching and the associated strain fields continue to help form the nanocolumns to a very high density as supported by theoretical predictions [23]. What is apparent is that the BSO nanocolumns of similar diameter continue to form even when the content is increased to 20 mol% and no coalescence between the columns is observed. Such a microstructure is found to be very beneficial for J_c property enhancement if the T_c can be maintained reasonably high.

1.3.5. Flux pinning enhancements in YBCO+BSO thick films

1.3.5.1. Preparation using sector target method

The J_c at 77 K as a function of applied magnetic field of YBCO+BSO films with different thicknesses are compared with 300 nm thick YBCO film at 77 K and a NbTi sample at 4.2 K in Figure 1.23. These films were found to contain ~ 15 – 20 mol% of BSO by image analyses. It can be seen that the J_c at 9 T in 1.9 μm thick YBCO+BSO films is nearly 3 orders of magnitude higher as compared to 300 nm thick YBCO film and is almost similar to NbTi. No significant degradation was noticed in YBCO+BSO films when the thickness is increased from 0.3 to 3.6 μm . In fact, as compared to YBCO+BSO films of 300 nm thickness, the 2.6 μm thick films had J_c that is more than 5 times higher over a range of fields. Contrary to what is observed in regular YBCO, as the thickness is increased, the films had some initial improvement. In addition, the 2 μm thick YBCO+BSO film ($J_c > 0.1 \text{ MA/cm}^2$) showed more than an order of magnitude increase in J_c at 7 T as compared to the J_c of a 1 μm thick regular YBCO film ($J_c = 0.01 \text{ MA/cm}^2 - 0.02 \text{ MA/cm}^2$) reported in the literature [24]. The J_c at 8 T of the 3.6 μm thick film is almost the same as the 300 nm thick YBCO+BSO nanocomposite film showing nearly no loss of J_c with thickness when measured at this field. Although the J_c of 3.6 μm thick films is slightly lower than that of the 2 or 2.6 μm thick films, an order of magnitude improvement in the J_c at 4 T in a 3.6 μm thick film as compared to regular YBCO film can also be observed. With the present processing conditions, films with thickness around 2 – 2.5 μm were found to have better quality than the films with other thickness. An increased extent of a-axis grain growth in the films was

determined from both x-ray diffraction and SEM observations as the thickness was increased especially in films with thickness greater than 2 μm . This increased a-axis grain growth is thought to be partially responsible for the reduction in J_c in 3.6 μm thick film. It may be contended that the in-field J_c of the films did not appreciably decrease with thickness from 300 nm to 2.5 μm since the self-field J_c of the films was lower to begin with. However, this is not the case since the in-field starting values are cited above as being significantly improved above that of other YBCO films. It is noted that the self-field values are slightly depressed, but for in-field applications this is irrelevant since the values are much improved in-field and maintain the high values up to large fields which is what matters for the applications. The self-field J_c is lower due to high volume fraction BSO content in the YBCO+BSO nanocomposite films, where pinning centers play a greatly reduced role. Figure 1.23 (b) shows the flux pinning force (F_p) data for various samples with different thicknesses, and it can be seen that a $F_{p \max}$ as high as 25 GN/cm³ can be obtained in these films. $F_{p \max}$ values seem to depend on the position showing decreased F_p as the peak position is moved to higher fields.



(a)

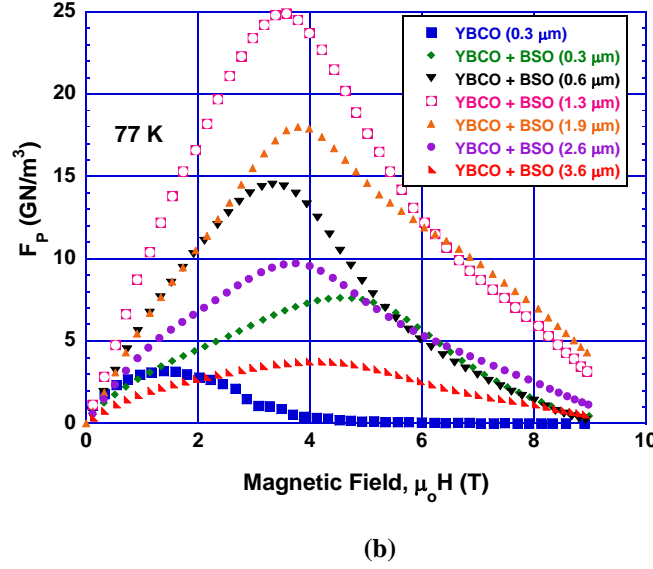


Figure 1.23. (a) Critical current density (J_c) of different thickness YBCO+BSO nanocomposite films as compared to 300 nm YBCO samples at 77 K, H/c and a NbTi sample at 4.2 K; (b) Flux pinning force (F_p) data for various samples with different thicknesses

Of particular importance is that the J_c reported in this report are derived from the magnetization measurements that are traditionally known to give lower J_c data than the transport current measurements. However, by comparing the J_c of 300 nm thick films with the 3.6 μm film measured in the same instrument, it is clear that the J_c remains high at high fields and does not show significant degradation as the thickness is increased at magnetic fields up to 9 T, the limit of our particular magnetometer model. The incorporation of a high volume fraction of (~ 10 vol%) of non-superconducting BSO phase would with no pinning enhancement reduce the J_c due to reduction of the superconducting phase (by ~ 10 vol%), indicating the additional strength of the pinning centers. A T_c of 87 – 88.5 K was measured in these thick YBCO+BSO films. Although high volume content of BSO was added, it did not reduce T_c as opposed to BZO, which reduces the T_c with > 2 vol% [25].

To see the J_c thickness dependence clearly, the J_c at 77 K in several of YBCO+BSO nanocomposite films is plotted as a function of their thickness in Figure 1.24. It can be seen that up to ~ 2.5 μm , J_c values at fields greater than 1T are higher in thick films than the corresponding thin films (300 nm) at any given field except self-field. It should be noted again that self-field J_c values are lower due to the high volume fraction of the BSO as discussed above. Further, the magnitude of drop in J_c with a change in field from 0 – 8 T is much less in YBCO+BSO thicker films as evidenced by the narrower J_c data spread in 3.6 μm thick sample compared to 300 nm thick YBCO+BSO sample in Figure 1.24.

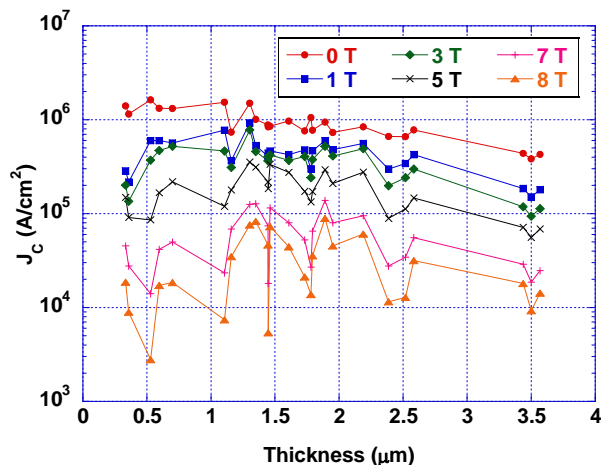


Figure 1.24. J_c values of YBCO+BSO films with different thicknesses at different applied fields measured at 77 K, with H//c orientation

Figure 1.25 shows a plan view scanning electron micrograph (SEM) of a 3.6 μm thick YBCO+BSO film showing uniform distribution of BSO (the bright phase) in these films. Figure 1.26 shows a cross-sectional TEM image of another sample of similar thickness. BSO nanocolumns were found to be straight, continuous and extend all the way through the thickness of the films. The average column size was found to be 10 – 11 nm and the separation was nearly 20 nm. The area density is calculated to be $2.5 \times 10^{11}/\text{cm}^2$ from these micrographs. Other defects such as dislocations, strain fields and stacking faults were also found to be present in thick films similar to the nanocolumns and defects observed in previously reported 300 nm thick YBCO+BSO films. The mechanism for such a microstructure formation is believed to be due to the strain energy minimization that exists due to the lattice mismatch (7.7%) between BSO and YBCO. A high density of continuous, solid BSO nanocolumns and associated defects, and increased irreversibility field are responsible for the improved properties observed in YBCO+BSO films. What is shown in this report is that a microstructure with long BSO nanocolumns can be maintained in thick films and that these nanocolumns help to grow thicker films that can maintain high J_c at high magnetic fields.

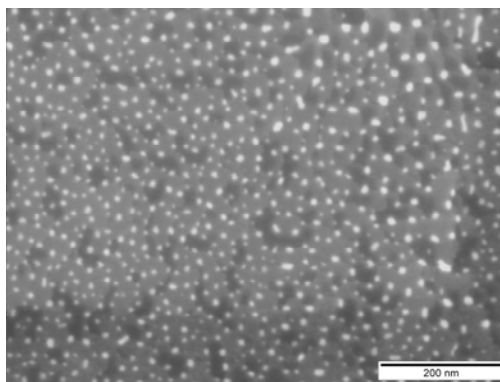


Figure 1.25. SEM micrograph of a ~ 3.6 μm film showing uniform distribution of BSO in YBCO matrix

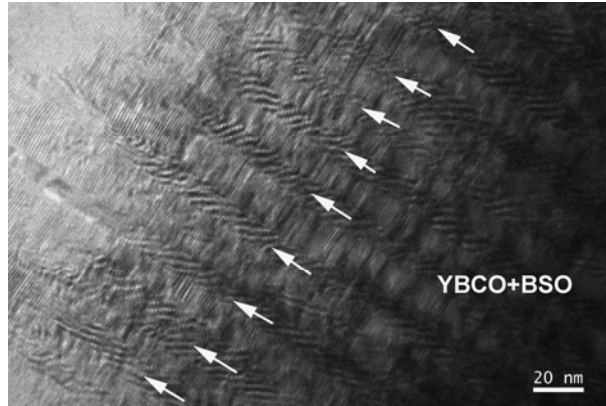


Figure 1.26. TEM cross-sectional image of a $\sim 3.6 \mu\text{m}$ film showing the BSO nanocolumns extending throughout the thickness of the films

TEM images show long BSO nanocolumns that extend throughout the thickness of the films, as shown in Figure 1.27. The density of the nanocolumns was $\sim 2.5 \times 10^{11}/\text{cm}^2$, and the average size was 10 – 11 nm. As compared to BaZrO_3 , nanocolumns of BSO seem to grow straight, and as a result of this microstructure, thick films continue to have higher J_c . The strain between BSO and YBCO seem to help grow such nanocolumns. In addition, thick films also showed some regions of very ordered and parallel nanocolumns, as shown in Figure 1.28. These straight nanocolumns that are ordered at some places are thought to be responsible for improved J_c values in thick films.

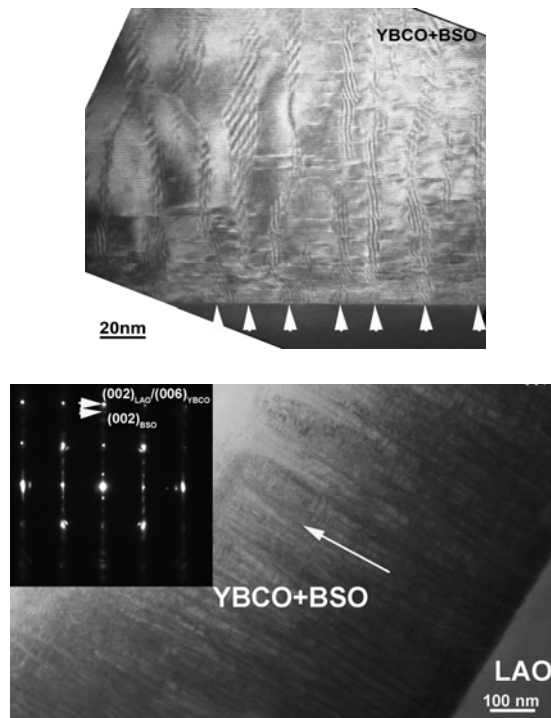


Figure 1.27. Cross-sectional TEM images of YBCO+BSO thick films at different magnifications showing that the BSO nanocolumns extend throughout the thickness

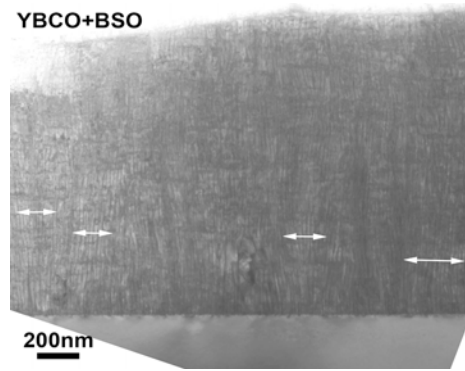


Figure 1.28. Cross-sectional TEM image of YBCO+BSO thick films showing the ordering of nanocolumns as shown by arrow marks

However, as the thickness was increased beyond $3.5\ \mu\text{m}$ with the present set of deposition conditions, a decreased J_c in films was observed. All the thick films had structurally well-defined nanocolumns (seen as nanoparticles in plan view), in high magnification SEM images as shown in Figure 1.29, and in the lower magnification images shown in Figure 1.30, although each of these films showed roughening of the films due to the growth of other orientation (such as a-axis) grains. X-ray diffraction data taken on thick films indicated that the (103) orientation grains were also present in these films and is illustrated in Figure 1.31. The increased number of mis-oriented grains is believed to be due to decreased substrate temperature as the thickness was increased. However, this occurs in much thinner films typically starting at $1\ \mu\text{m}$ in the YBCO only films. Due to the increased number of these mis-oriented grains, the J_c of films with more than $3.5\ \mu\text{m}$ can be expected to decrease. If a proper growth temperature can be maintained to avoid the formation of mis-oriented grains, much thicker films with the same quality as thin YBCO+BSO films can be made with improved properties. Even so, the addition of the BSO nanocolumns apparently delays the formation of the mis-oriented growth until significantly thicker films [26].

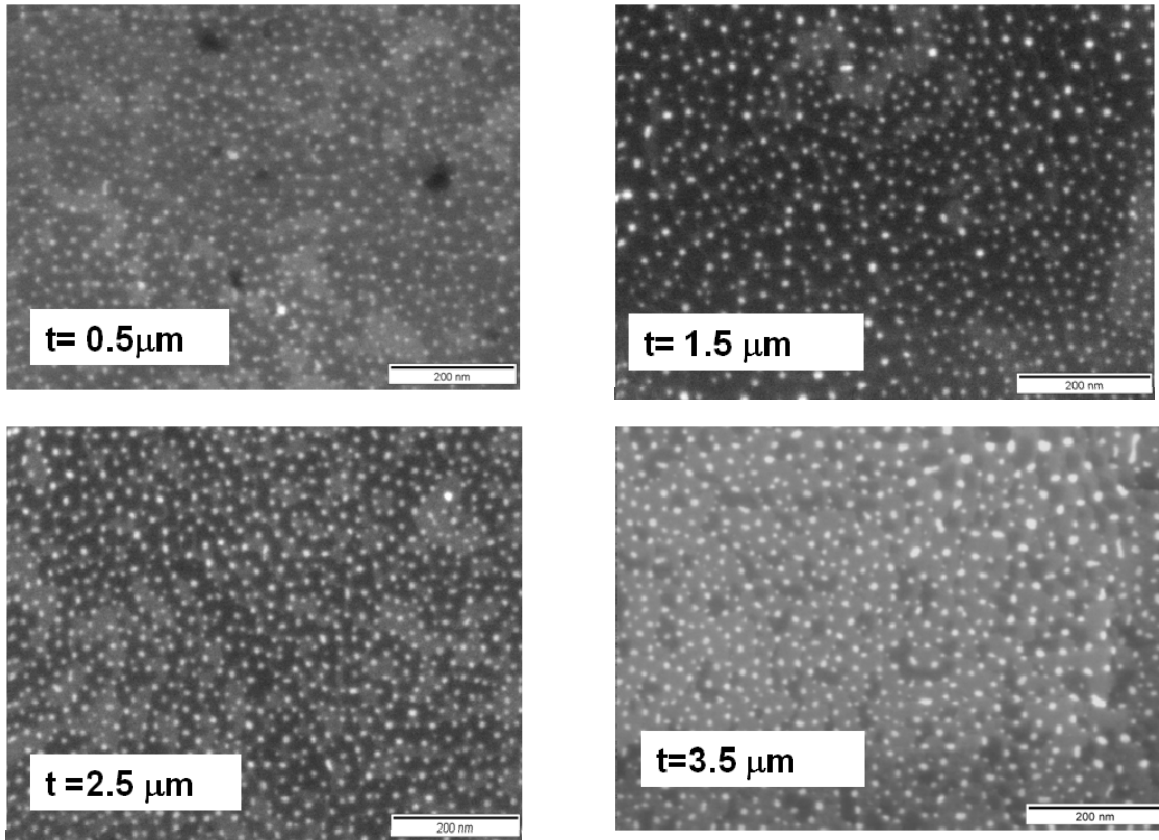


Figure 1.29. High resolution scanning electron images of YBCO+BSO thick films with different thicknesses (t) showing the planar view of the BSO nanorods

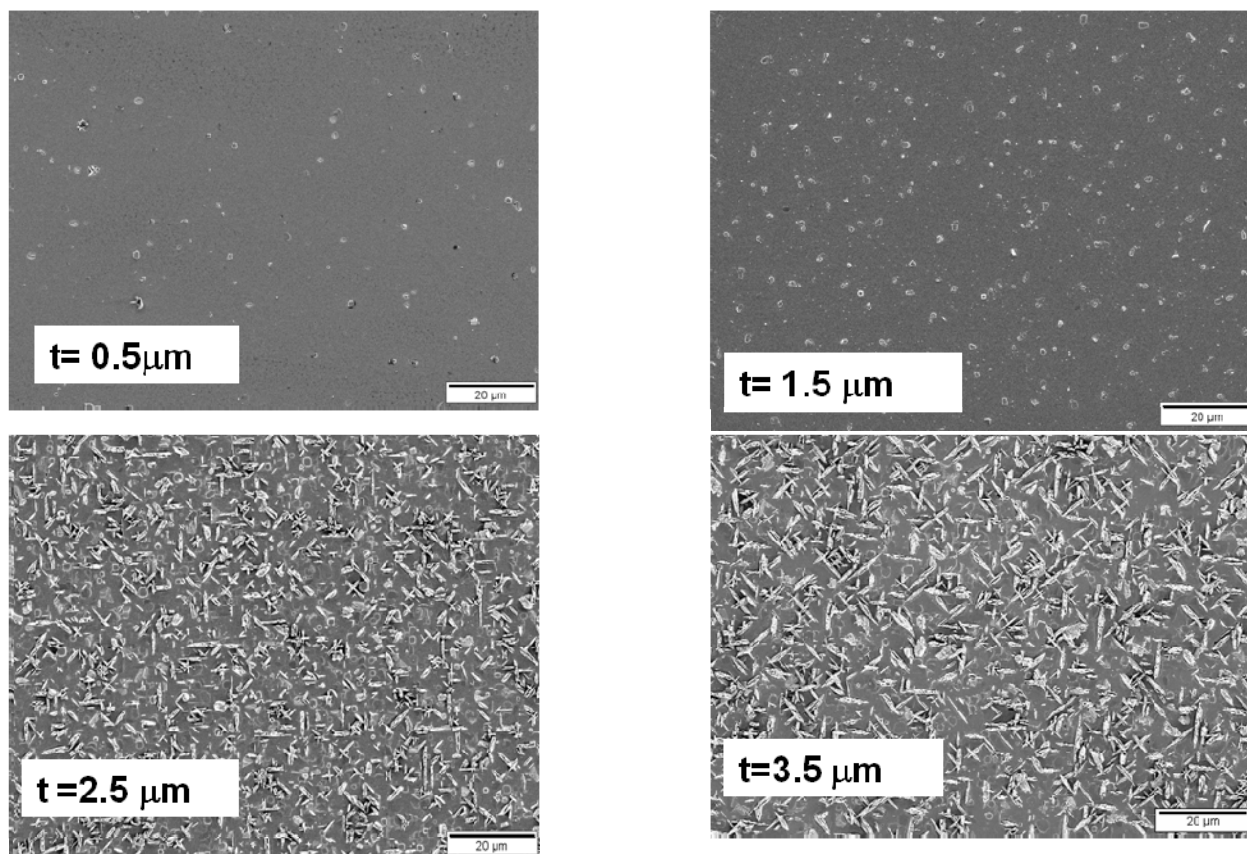


Figure 1.30. Low magnification SEM images of YBCO+BSO thick film showing an increase in the amount of mis-oriented grains as the thickness was increased.

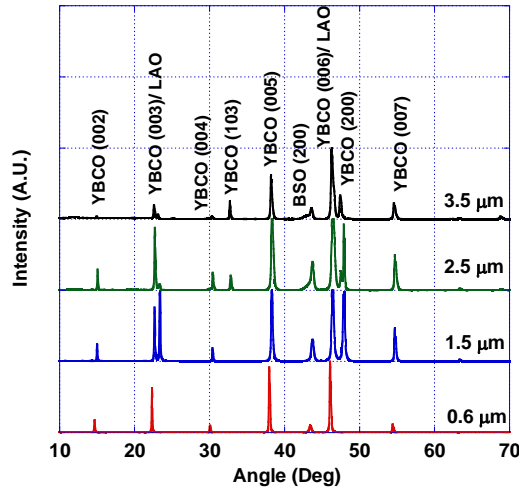


Figure 1.31. X-ray diffraction patterns of YBCO+BSO thick films showing the BSO (100) and YBCO (100) peaks in all samples; an increase in YBCO (103) is seen as thickness was increased

1.3.5.2. YBCO+20 mol% BSO thick films made using a pre-mixed target

The T_c data of YBCO+BSO samples of different thickness are shown in Figure 1.32. All the films for this study showed a T_c of ~ 87 K. It can be seen that the T_c does not degrade as the film thickness is increased, even up to 3 μm. This offers initial confirmation that 30 min of oxygenation is sufficient for even the thick films. A slight reduction of T_c to 87 K is consistent with the thin films of YBCO+BSO as reported earlier [26].

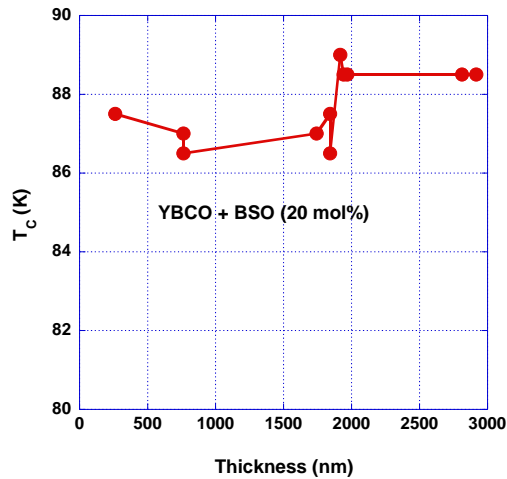


Figure 1.32. T_c in YBCO+20 mol% BSO films with varying thickness

A plot of the J_c of different thickness samples is shown as a function of applied magnetic fields in Figure 1.33. The results show that the samples continue to maintain their J_c very well even when the thickness is increased, especially at higher fields. At 8 T of applied magnetic field, the J_c of a YBCO+BSO sample of 2.8 μm thickness was $1.5 \times 10^4 \text{ A/cm}^2$, which is similar to the J_c of a 260 nm thick YBCO+BSO sample. Although there is some reduction in J_c evident at very low fields, there appears to be a slight improvement at the higher fields as the thickness approaches the 1 μm range.

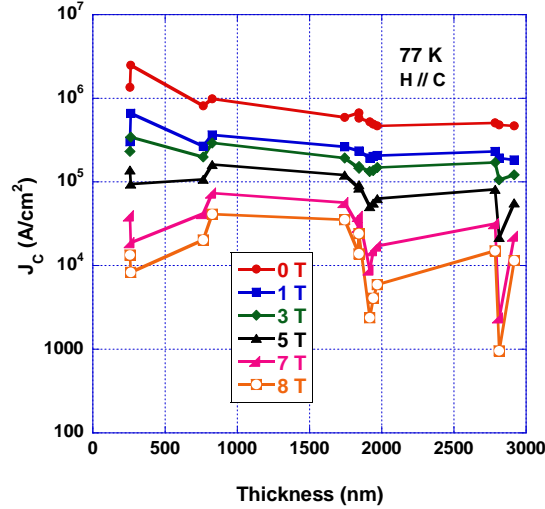


Figure 1.33. J_c values for varying thickness YBCO+20 mol% BSO films at 77 K and H//c

Figure 1.34 displays several magnetization J_c curves of thick YBCO+BSO samples. These are compared with a YBCO 300 nm film standard. After 1.8 T, all YBCO + BSO films show improvement from YBCO. At 8 T it can be seen that the YBCO + BSO films are at least 2 orders of magnitude better than the undoped YBCO.

X-ray diffraction ($\theta - 2\theta$) data taken from different samples is shown in Figure 1.35. The area of interest has been expanded and compared for 4 representative thickness samples. All the samples show good texture for (00l) type YBCO peaks. However, an additional peak appears in the thicker samples which corresponds to YBCO (103) peak. This peak becomes more intense in the 2.8 μm thickness sample. These mis-oriented grains are expected as the temperature at the growing surface could be lower in thicker films than thin films as the films are heated from the back of the substrate. These mis-oriented grains could be the primary cause for the slight drop in self-field J_c as observed in films with thickness $> 2 \mu\text{m}$.

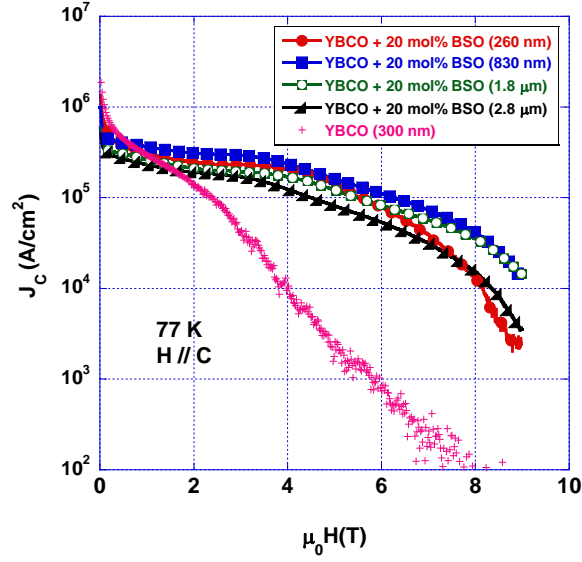


Figure 1.34. VSM J_c data for selected YBCO+20 mol% BSO film thicknesses compared with 300 nm YBCO at 77 K and H//c

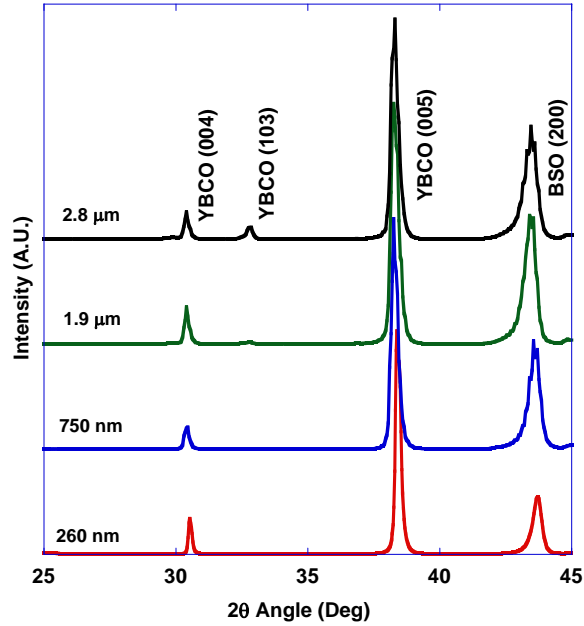


Figure 1.35. X-ray $\theta - 2\theta$ scans of YBCO+20 mol% BSO of varying thickness

Figure 1.36 shows the low magnification (1.5 kx) scanning electron surface micrographs of (a) 260 nm and (b) 2.8 μm thick YBCO+BSO samples. The 260 nm shows standard surface features for YBCO+BSO with small particles (note that these particles are not the planar view of the

nanocolumns) on the surface that can be observed at low magnification. The 2.8 μm sample, however, shows mis-oriented grains such as a-axis grain growth occurring in the sample. Despite these mis-oriented grain growth (possibly created by the lower surface temperature as discussed before) in thick films, the YBCO+BSO microstructure still shows nanocolumn formation of BSO continuing into the upperparts of the films. Figure 1.37 shows at higher magnification (150 kx) the (a) 260 nm sample and (b) 2.8 μm sample. Both display a uniform distribution of BSO nanoparticles at the surface. These are the cross-sections (ab planar view) of the BSO nanocolumns as observed in cross-sectional transmission electron micrographs shown later.

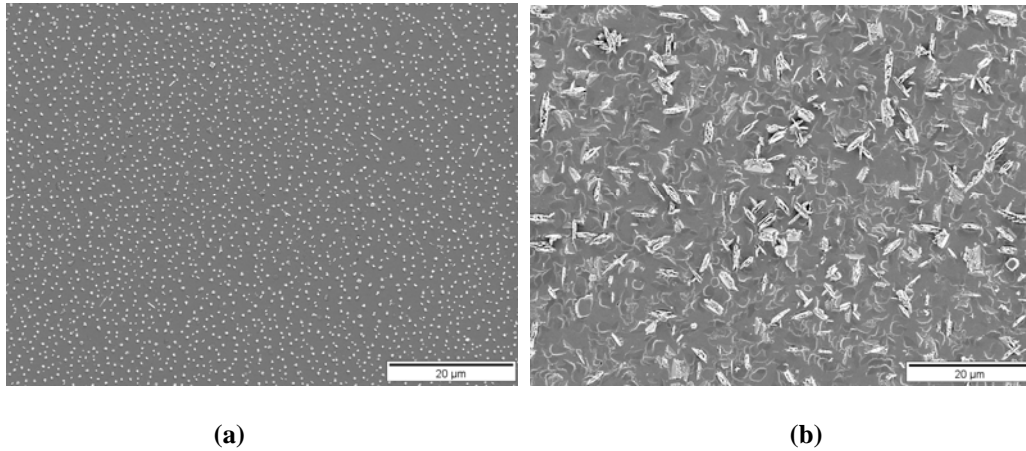


Figure 1.36. SEM photomicrograph showing surface microstructure of (a) 260 nm sample and a (b) 2.8 μm sample

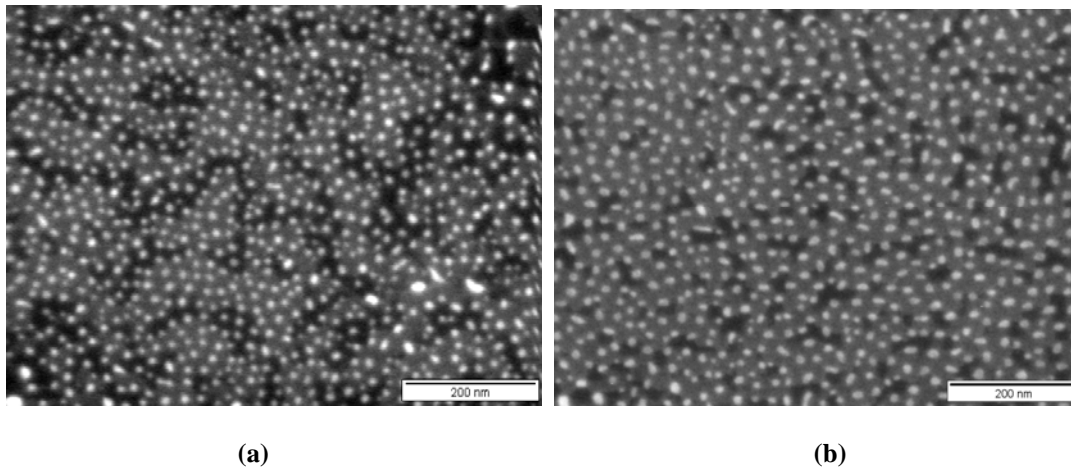


Figure 1.37. SEM photomicrograph showing uniform BSO distribution in YBCO on (a) 260 nm sample and a (b) 2.8 μm sample

Cross-sectional TEM was done on the samples to investigate the extent of the BSO nanocolumnar formation in the samples as well. Figure 1.38 shows a YBCO+BSO film of (a) 750 nm thickness and (b) 2.8 μm thickness. Both samples show nanocolumns with a diameter of

~ 8 – 11 nm. Both also show continuous nanocolumns that extend through the thickness of the film. They appear to be relatively unaffected by the appearance of a-axis growth. The nanocolumns were similar to the nanocolumns shown in the YBCO+BSO thick film made with a sector target.

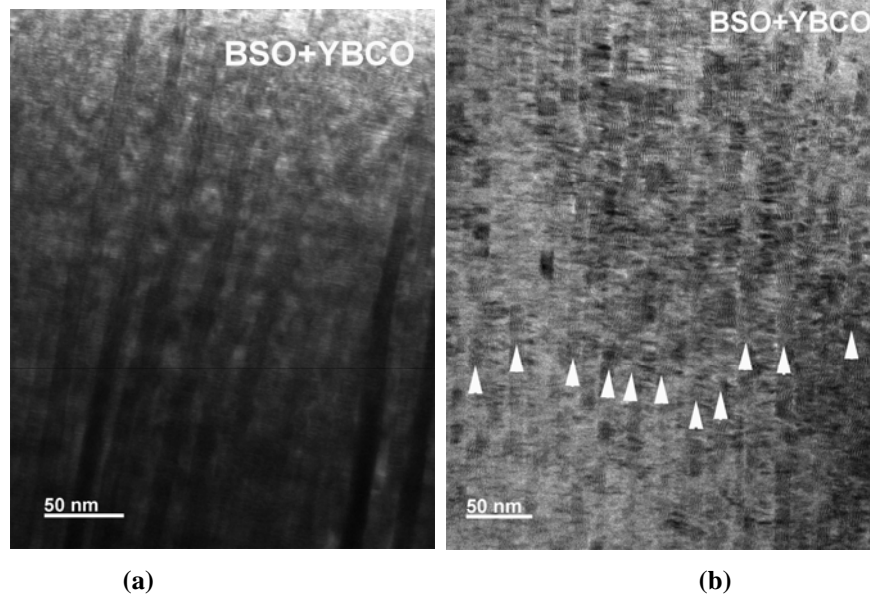


Figure 1.38. Cross sectional TEM image showing through-thickness, uniform BSO nanocolumns in (a) 780nm film and a (b) 2.8 μm film

1.4. Conclusion

It is shown that YBCO films with BaSnO_3 (BSO) nano-additions, made with either a sector target or with a premixed target in PLD, have a much greater improvement in J_c at higher fields with a H//c orientation. More than two orders of magnitude improvement in J_c was observed as compared to undoped or similarly processed Y_2BaCuO_5 (Y211) doped samples at magnetic fields higher than 5 T. The reasons for such an improvement were found to be due to the formation of BSO nanocolumns of 8 – 10 nm diameters in the films in a density of $\sim 3.5 \times 10^{11}/\text{cm}^2$. These nanocolumns nucleate at the interface and subsequently grow perpendicular to the substrate while allowing high quality YBCO to grow around them. Although similar processing conditions were used, Y211 formed nanoparticles, whereas BSO formed nanocolumns in the YBCO due to the crystal structure match between both BSO and YBCO (both are perovskites) and appropriate lattice strain and suitable deposition conditions. The BSO content was also systematically increased from 2 to 20 mol% by using premixed targets of YBCO, BSO to explore the effects of BSO content variations in YBCO. It is shown that even with 20 mol% BSO addition, films can be grown without a significant decrease in critical transition temperature (T_c). While the nanocolumns' diameter remained 8 – 10 nm in diameter, the distance between them decreased from 50 nm to 20 nm as the concentration was increased from 2 mol% to 20 mol%, resulting in an increase in the number density. An overall improvement at both low and high fields was observed in YBCO+10 mol% BSO samples. BSO nanocolumns were also found to help maintain a high critical current density ($J_c > 10^4 \text{ A}/\text{cm}^2$, at

8 T) in thick films made by a sector target and showed no degradation in J_c at the higher fields when the thickness was increased from 300 nm to 3 μm . Also $F_{p\text{ max}}$ values of more than 25 GN/m³ at 77 K were noted in the YBCO+BSO films with thickness > 1 μm . The F_p peak position was found to be shifted to higher fields (> 4 T) and two clearly distinguishable peaks were observed in some of the F_p plots. The YBCO+BSO films deposited on buffered metallic substrates showed similar improvements as seen on the single crystal substrates, indicating that the BSO nano-additions can be introduced on polycrystalline buffer layers as used in coated conductors. Unlike BaZrO₃, BSO seems to allow higher relative amounts of additions to YBCO without a significantly depressing T_c . The BSO nanocolumns seem to grow as solid nanorods as opposed to stacked individual nanoparticles. In addition, they were found to grow vertically straight and hence help to improve the J_c at high fields by several orders of magnitude in thick films making it attractive for coated conductors.

1.5. References

1. D. Larbalestier, A. Gurevich, D. M. Feldmann and A. Polyanskii, *Nature* 414 (2001) 368.
2. A. Goyal, D.F. Lee, F.A. List, E.D. Specht, R. Feenstra, M. Paranthaman, X. Cui, S.W. Lu, P.M. Martin, D.M. Kroeger, D.K. Christen, B.W. Kang, D.P. Norton, C. Park, D.T. Verebelyi, J.R. Thompson, R.K. Williams, T. Aytug and C. Cantoni, *Physica C* 357-360 (2001) 903.
3. X. Li, M.W. Rupich, T. Kodenkandath, Y. Huang, W. Zhang, E. Siegal, D.T. Verebelyi, U. Schoop, N. Nguyen, C. Thieme, Z. Chen, D.M. Feldman, D.C. Larbalestier, T.G. Holesinger, L. Civale, Q.X. Jia, V. Maroni and M.V. Rane, *IEEE Trans. Appl. Supercond.* 17 (2007) 3553.
4. X. Xiong, K.P. Lenseth, J.L. Reeves, A. Rar, Y. Qiao, R.M. Schmidt, Y. Chen, Y. Li, Yi-Y. Xie and V. Selvamanickam, *IEEE Trans. Appl. Supercond.* 17 (2007) 3375.
5. T. Aytug, M. Paranthaman, L. Heatherly, Y. Zuev, Y. Zhang, K. Kim, A. Goyal, V. A. Maroni, Y. Chen and V. Selvamanickam, *Supercond. Sci. Technol.* 22 (2009) 015008.
6. P. Malozemoff, S. Fleshler, M. Rupich, C. Thieme, X. Li, W. Zhang, A. Otto, J. Maguire, D. Folts, J. Yuan, H.-P. Kraemer, W. Schmidt, M. Wohlfart and H.-W. Neumueller, *Supercond. Sci. Technol.* 21(2008) 034005.
7. V. Selvamanickam, Y. Chen, X. Xiong, Y.Y Xie, J.L. Reeves, X. Zhang, Y. Qiao, K.P. Lenseth, R.M. Schmidt, A. Rar, D.W. Hazelton and K. Tekletsadik, *IEEE Trans. Appl. Supercond.* 17 (2007) 3231.
8. P.N. Barnes, M.D. Sumption and G.L. Rhoads, *Cryogenics* 45 (2005) 670.
9. C. Varanasi, R. Biggers, I. Maartense, D. Dempsey, T.L. Peterson, J. Solomon, J. McDaniel, G. Kozlowski, R. Nekkanti and C.E. Oberly, *Proceed. Mater. Res. Soc. Advances in Laser Ablation of Materials Symposium*, eds. R.K. Singh, D. Lowndes, D.B. Chrisey, E. Fogarassy and J. Narayan (1998) p. 263.
10. C.V. Varanasi, J. Burke, L. Brunke, H. Wang, J.H. Lee and P.N. Barnes, *J. Mater. Res.* 23 (2008) 3363.
11. C. Varanasi, P.N. Barnes, J. Burke, J. Carpenter and T.J. Haugan, *Appl. Phys. Lett.* 87 (2005) 262510.
12. C.V. Varanasi, P.N. Barnes, J. Burke, L. Brunke, I. Maartense, T.J. Haugan, E.A. Stinzianni, K.A. Dunn and P. Halder, *Supercond. Sci. Technol.* 19 (2006) L37.

13. C.V. Varanasi, J. Burke, L. Brunke, H. Wang, M. Sumption and P.N. Barnes, *J. Appl. Phys.* 102 (2007) 063909.
14. C.V. Varanasi, J. Burke, L. Brunke, J.H. Lee, H. Wang and P.N. Barnes, *IEEE Trans. Appl. Supercond.* (2009) in press.
15. A. Goyal, S. Kang, K.J. Leonard, P.M. Martin, A.A. Gapud, M. Varela, M. Paranthaman, A.O. Ijaduola, E.D. Specht, J.R. Thomson, D.K. Christen, S.J. Pennycook and F.A. List, *Supercond. Sci. Technol.* 18 (2005) 1533.
16. L. Civale, B. Maiorov, A. Serquis, S.R. Foltyn, Q.X. Jia, P.N. Arendt, H. Wang, J.O. Willis, J.Y. Coulter, T.G. Holesinger, J.L. MacManus-Driscoll, M.W. Rupich, W. Zhang and X. Li, *Physica C* 412-414 (2004) 976.
17. L. Civale, B. Maiorov, J.L. MacManus-Driscoll, H. Wang, T.G. Helesinger, S.R. Foltyn, A. Serquis and P.N. Arendt, *IEEE Trans. Appl. Supercond.* 15 (2005) 2808.
18. P. Mele, K. Matsumoto, T. Horide, A. Ichinose, M. Mukaida, Y. Yoshida and S. Horii, *Supercond. Sci. Technol.* 20 (2007) 244.
19. A. Gapud, D. Kumar, S.K. Viswanathan, C. Cantoni, M. Varela, J. Abiade, S.J. Pennycook and D.K. Christen, *Supercond. Sci. Technol.* 18 (2005) 1502.
20. C.V. Varanasi, P.N. Barnes and J. Burke, *Supercond. Sci. Technol.* 20 (2007) 1071.
21. S. Kang, A. Goyal, J. Li, P. Martin, A. Ijaduola, J.R. Thomson and M. Paranthaman, *Physica C* 457 (2007) 41.
22. J. Feng, K.K. Yeung, K.W. Wong, C.L. Fu and C.C. Lam, *Supercond. Sci. Technol.* 13 (2000) 215.
23. J.P. Rodriguez, P.N. Barnes and C.V. Varanasi, *Phys. Rev. B* 78 (2008) 052505.
24. S.R. Foltyn, L. Civale, J.L. Macmanus-Driscoll, Q.X. Jia, B. Mairov, H. Wang and M. Maley, *Nat. Mater.* 6 (2007) 631.
25. S. Kang, A. Goyal, J. Li, P. Martin, A. Ijaduola, J.R. Thomson and M. Paranthaman, *Physica C* 457 (2007) 41.
26. C.V. Varanasi, J. Burke and P.N. Barnes, *Appl. Phys. Lett.* 93 (2008) 092501.

2. Effects of Second Phase (BaGeO₃, BaSiO₃) Nanocolumns in YBa₂Cu₃O_{7-x} Films

2.1. Introduction

YBa₂Cu₃O_{7-x} (YBCO) coated conductors need the introduction of additional flux pinning centers to enhance the critical current density (J_c) in applied magnetic fields [1, 2]. Second phase additions such as BaZrO₃ (BZO) [3,4] and BaSnO₃ (BSO) [5,6] have been shown to form nanocolumnar pinning sites in YBCO films and contribute towards enhancing the critical current density (J_c), especially in the H//c orientation. Up to 20 mol% of BSO additions seem to have no deleterious effects on the critical transition temperature (T_c) [7] of the YBCO+BSO films but enhance J_c by several orders of magnitude at high fields as shown in Chapter 1. Typically, BSO nanocolumns were found to enhance J_c by more than two orders of magnitude at 77 K in applied fields of > 5 T in H//c. Even in thick films > 1 μ m, the BSO nanocolumns continue to grow perpendicular to ab planes and offer maintenance of high J_c in the films [8]. In the YBCO+BZO system, similar improvements were also noted but it was found that just 5 vol% BZO could reduce the T_c significantly [9].

It appears that for nanocolumnar formation in YBCO, values such as T_c , J_c , etc., depend mainly upon the composition of the added second phases as well as the self-assembly of the second phase material into the nanocolumns. Similarly processed YBCO+Y₂BaCuO₅ (Y211) films do not form the nanocolumns. Further, the T_c is not significantly reduced in YBCO+Y211 films but the T_c is slightly reduced in YBCO+BSO films. The T_c reduction indicates a potential chemical compatibility issue for the second phase addition. It is important that the number density of nanocolumns and associated defects need to be increased as high as possible at higher magnetic fields to maximize J_c in YBCO films, without sacrificing the T_c of the films. The number density of nanocolumns also depends upon the composition and concentration of the second phase doping. It is of interest to study what effect different compositions of second phase additions will have on the formation of nanocolumns and superconducting properties (T_c , J_c) of YBCO films. In this study, second phase additions of BaGeO₃ (BGeO) and BaSiO₃ (BSiO) were investigated for their ability to form nanocolumns and their effect on the T_c and J_c of YBCO films. The intent was to determine the effect of substituting different column IV elements of the periodic table in place of Sn for BSO. The properties were compared with YBCO+BSO films.

2.2. Experimental

2.2.1. BaGeO₃

BGeO (PDF# 30-0127) has a hexagonal crystal structure with cell dimensions as 7.59 Å x 7.59 Å x 10.79 Å and a density of 4.73 g/cm³. It also has a high temperature orthorhombic form [11,12]. The BGeO target was prepared in-house by solid state reaction from precursor powders of BaCO₃ (99.997% purity, Alfa Aesar) and GeO₂ (99.999% purity, Alfa Aesar). The precursor powders were dried at 450 °C for 8 h in alumina crucibles. The powders were measured with a 1:1 molar ratio and mixed in an agate mortar for 30 mins to ensure a homogeneous mixture. The mixed powder was reacted at 1050 °C for 48 h in air. The powder was again mixed using agate mortar and pestle and then was pressed in a hydraulic hand press using a 1.25 in. dia. die then placed in a furnace and heated to 1050 °C for 48 h. A third heating cycle was run at 1100 °C for 48 h yielding a theoretical density of 57.7 %. An additional higher temperature reaction at 1200 °C improved the density but showed some evidence of incipient melting. X-ray diffraction

patterns were obtained from the ground powder from these disks. Sector pieces cut from these disks were fixed on top of a YBCO target and was used to make YBCO+BGeO films.

2.2.2. BaSiO₃

BSiO (PDF# 26-1402) has an orthorhombic crystal structure with cell dimensions of 5.6182 Å x 12.445 Å x 4.5816 Å and a density of 4.425 g/cm³. Ba₂SiO₄ (PDF# 26-1403) is also orthorhombic with a cell size of 7.508 Å x 10.214 Å x 5.8091 Å and a density of 5.468 g/cm³. BaSiO₃ targets were made using BaSiO₃ powder purchased from Alfa Aesar. The commercially available powder has a composition corresponding to 74.3% BaO and 21.8% SiO₂. Initially the purchased powder was dried in an alumina crucible at 450 °C for 8 h. The powder was then mixed in an agate mortar and then pressed in a hydraulic hand press using a 1.25 in. dia. die. The target was then reacted at 1000 °C for 50 h yielding a density of approximately 64.2 % the theoretical density. The target was then heated again to 1200 °C yielding a density of approximately 90.7 % the theoretical density. A small section of target was then cut using a diamond saw and ground using agate mortar and pestle and was analyzed using a Rigaku DMAX 2500 X-ray powder diffractometer. Sectors of the BSiO disk were cut and fixed on top of a YBCO target and was used to make YBCO+BSiO films.

2.2.3. Targets and Deposition

To create the premixed targets of YBCO+BGeO, for example, a 20 g batch of BGeO was first made by solid state reaction from precursor powders as discussed above. The precursor powders were dried at 450 °C for 8 h in an alumina crucible. The powders were measured with a 1:1 molar ratio and mixed in an agate mortar with pestle for 30 min to ensure a homogeneous mixture. The mixed powder was reacted at 1050 °C for 48 h. The powder was again mixed using agate mortar and pestle and heated to 1050 °C for 72 h. The mix targets were made from Nexans YBCO powder and the BGeO powder previously made. YBCO was dried in an alumina crucible at 450 °C for 8 h. After drying, the powders were mixed using 2 vol% and 4 vol% BGeO to YBCO powder. Each target was thoroughly mixed using agate mortar and pestle and pressed in 1.25 in. dia. die using a hydraulic press. The targets were then reacted in air at 850 °C for 72 h and 920 °C for 168 h. The targets obtained a density of 93.1 % (2 vol% BGeO) and 91.05 % (4 vol% BGeO) of the theoretical density.

All the YBCO+second-phase films were deposited in a Neocera pulsed laser ablation chamber using $\lambda = 248$ nm Lambda PhysiK excimer laser. Standard method as used before for processing YBCO+BSO films (780 °C growth temperature, 300 mTorr O₂ pressure, 625 mJ laser energy, 4 Hz repetition rate) were used to process YBCO+BGeO and YBCO+BSiO films [10]. LaAlO₃ (100) single crystal substrates were used to deposit YBCO film with different second-phase additions. Sected targets with a 30° sector of BGeO or a BSiO fixed on top of a YBCO target and premixed targets of 2, 4 vol% BGeO were used to deposit ~ 300 nm thick films.

Films were characterized by x-ray diffraction and the microstructures were studied by plan view scanning electron microscopy (SEM) and a cross-sectional transmission electron microscopy (TEM). The superconducting properties such as critical transition temperature (T_c) was measured by using a dc susceptibility method in a Physical Property Measurement System (Quantum Design PPMS) and the self-field critical current density (J_c) was measured by using a four point probe method on a patterned bridge at 77 K.

2.3. Results and Discussion

Figure 2.1 shows the $\theta - 2\theta$ x-ray diffraction pattern of BGeO powder used for premix targets and sintered BGeO used for sector target. All the peaks corresponding to BGeO were observed indicating that the reaction was mostly complete and the precursors are converted into BaGeO₃. However some small intensity peaks corresponding to some other unidentified phases were also observed to be present in the patterns. Repeated grinding and high temperature reactions did not reduce this unknown phase. In the literature [11, 12] the possibility of formation of other polymorphic phases as well as other phases such as Ba₂GeO₄ were noted in the BaO-GeO₂ system. Although the peaks did not match any of the known phases, it is thought that the unknown peaks correspond to some other intermediate phases. Figure 2.2 shows the x-ray powder diffraction patterns taken from BaSiO₃ powders used in this study. It can be seen that the commercially available powders contain mixtures of BaSiO₃, BaSi₂O₄. Since both are orthorhombic structures and contain Ba, Si, and O, targets were made using these powders to investigate the nanocolumn formation. In either case, during the PLD, the bonds of these phases are broken and recombine in the growing film to form again.

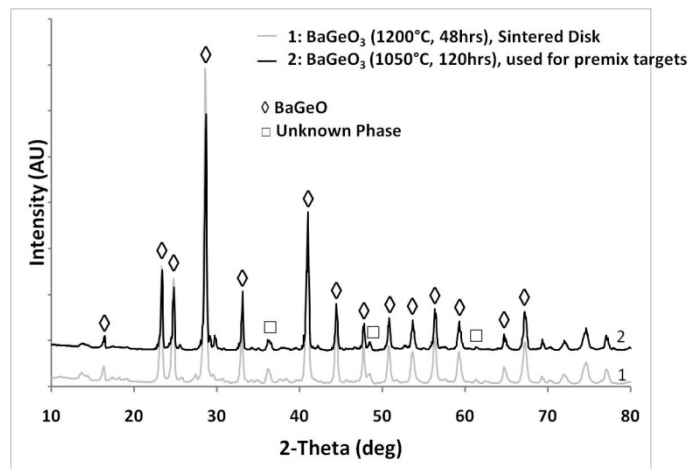


Figure 2.1. X-ray $\theta - 2\theta$ scans of BaGeO₃ prepared samples

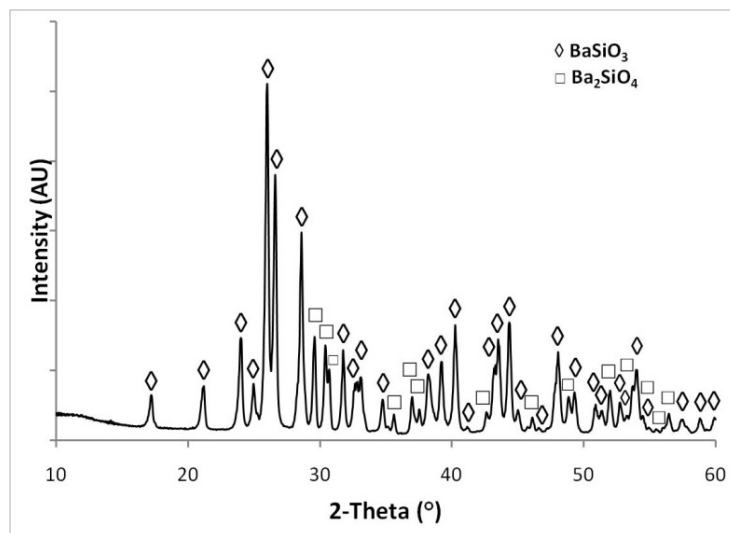


Figure 2.2. X-ray $\theta - 2\theta$ patterns of Ba-Si-O powder

Figure 2.3 shows a plan view SEM micrograph of images of YBCO+BGeO and YBCO+BSiO films made by using a sector target. A good distribution of the bright phase (white contrast) that represents the second phase material is found to be well dispersed in the microstructure. Around 20 nm diameter nanoparticles were observed in both the samples. Although they appear as nanoparticles in plan view SEM, these are evidently the cross-sections of nanocolumns as discussed later. The microstructures of YBCO+BGeO and YBCO+BSiO look very similar to YBCO+BSO samples processed in the same fashion. Figure 2.4 shows cross-sectional transmission electron micrographs of YBCO+BGeO samples in two different magnifications. It can be seen that the nanocolumns are around 20 nm and extend throughout the thickness of the films. As reported earlier, nanocolumns in YBCO+BSO are of 8 – 10 nm in diameter and were found to be very straight. However with YBCO+BGeO, the nanocolumns seem to be almost double in size and also they were found to be not as straight as BSO. The lattice mismatch and strain between the matrix of YBCO and second phase additions can dictate the equilibrium diameter and splay of the nanocolumns.

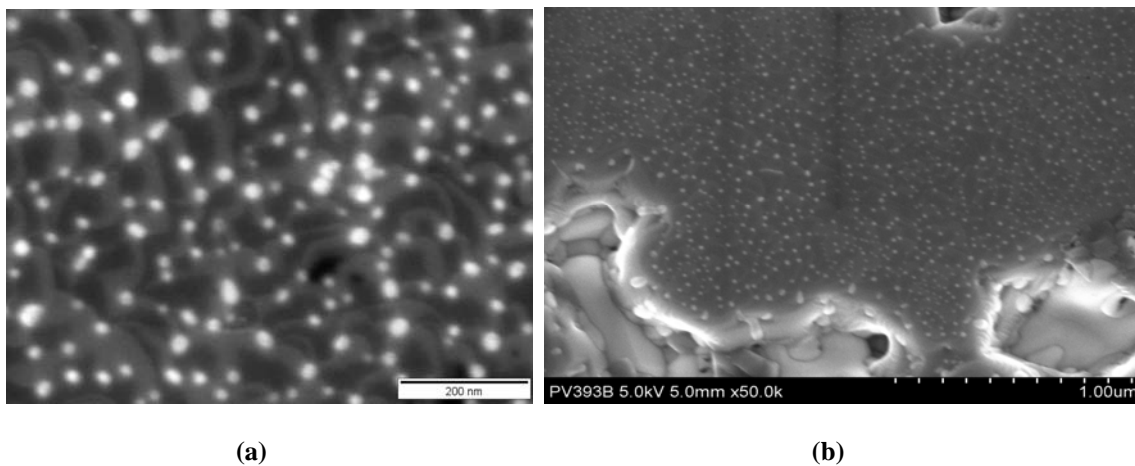


Figure 2.3. Plan View SEM micrographs of YBCO films made by using a PLD sector target of (a) YBCO+BGeO and (b) YBCO+BSiO

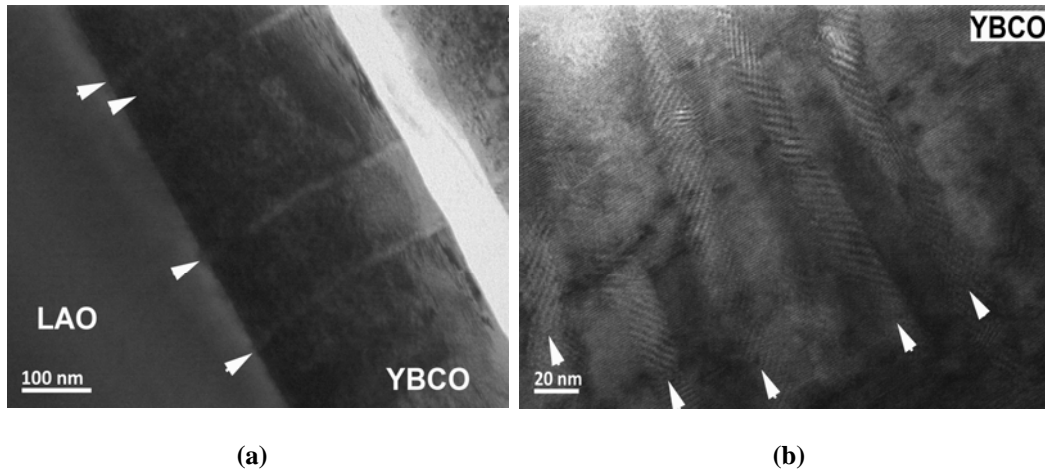


Figure 2.4. Cross-sectional TEM micrographs of YBCO+BGeO samples showing the nanocolumns at two different magnifications: (a) low magnification and (b) high magnification

Figure 2.5 shows the x-ray diffraction patterns taken from the films which indicate that the YBCO films are c-axis oriented. However, reflections corresponding to BGeO of (112) orientations were noted as opposed to (002) orientations BSO peaks observed in YBCO+BSO films. The orientation relationships between BGeO and YBCO appear to be different than YBCO and BSO as the crystal structures are different. Figure 2.6 shows the cross-sectional transmission electron micrographs of YBCO+BSiO films also showing the presence of 20 nm diameter nanocolumns extending throughout the thickness of the YBCO+BSiO films. The diameters of the nanocolumns were similar to BGeO nanocolumns observed in YBCO+BGeO.

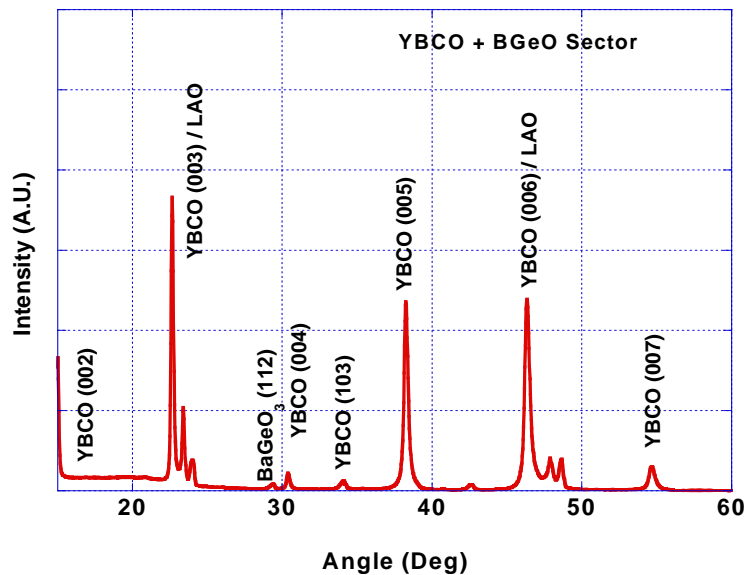


Figure 2.5. X-ray $\theta - 2\theta$ diffraction patterns of YBCO+BGeO films showing the (001) orientation of YBCO films

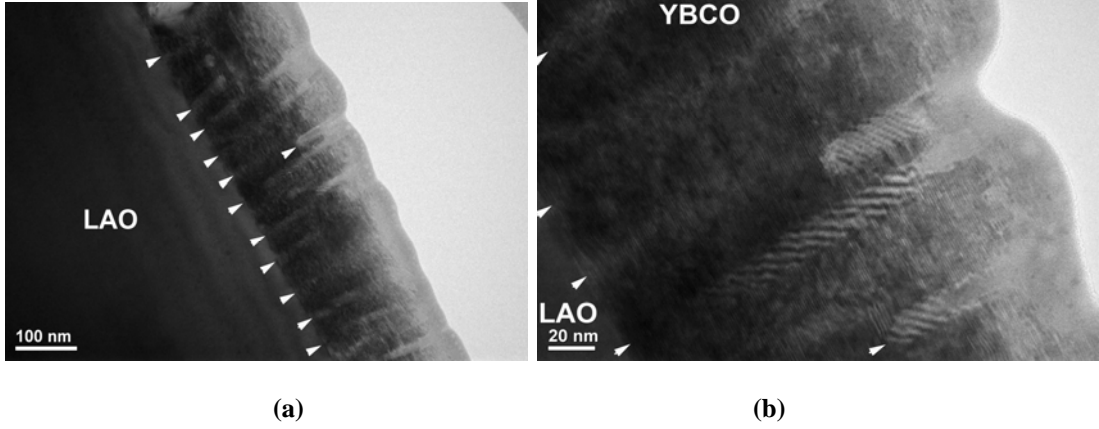


Figure 2.6. Cross-sectional TEM showing the nanocolumns in YBCO+BSiO films at two different magnifications: (a) low magnification and (b) high magnification

Figure 2.7 shows the T_c measurement of various films processed in the present study. It can be seen that the T_c is severely depressed in all the doped films. YBCO+20 mol% BGeO films had a T_c of 78 K where as YBCO+20 mol% BSiO with had a T_c of 88 K. The T_c depression is thought to be due to the substitution of Ge in the YBCO lattice mostly in the Cu sites. When the doping levels are reduced from 4 mol% to 2 mol% in the case of BGeO and large sector vs. small sector in the case of BSiO, the T_c of the samples was found to improve. This trend also seems to suggest that the atomic substitutions were possibly responsible for the T_c depression. As the concentration was reduced, fewer amounts of substitutions could take place resulting in better T_c . However, the T_c is still very low even with 2 mol% BGeO giving a self field J_c of 0.7 MA/cm² at 77 K. The T_c was found to be reduced in YBCO+BSiO films as well and it is also thought that Si substitutions could cause the T_c drop.

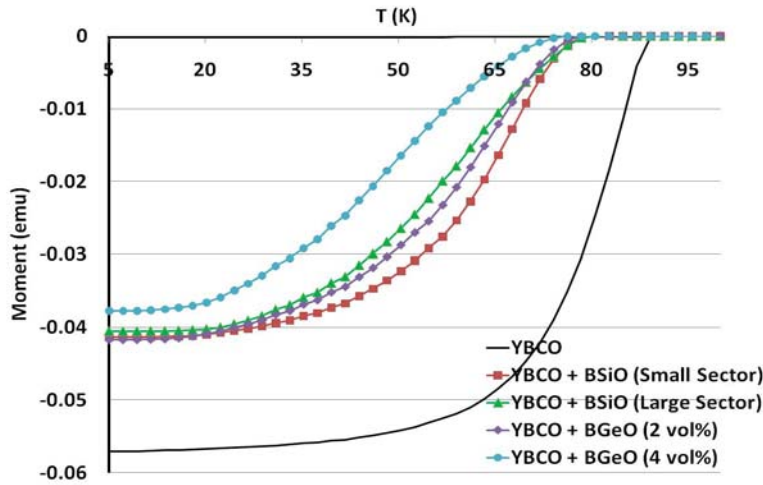


Figure 2.7. Susceptibility of YBCO+BGeO and YBCO+BSiO films showing the T_c data of different samples

YBCO+BSO samples with BSO nanocolumns also had slightly reduced T_c of 87 K, but the T_c reduction effect on J_c was minimal. So the net effect was that J_c enhancements with the BSO nanocolumns are possible. Although the BGeO and BSiO form nanocolumns, the T_c suppression

is too high to realize the advantages of having these pinning centers. It appears that the chemical compatibility of the second phases is very critical to maintain high J_c of the films. Even though the texture of YBCO was unaffected and a desired microstructure with nanocolumns was present, the T_c is reduced and the overall J_c of the films was reduced. Again, this may be due to the atomic substitutions of Ge and Si in to YBCO. While both the YBCO+BZO and YBCO+BSO systems offer a nice combination of texture maintenance, favorable T_c , and appropriate pinning centers, BSO seems to offer more flexibility in terms of the amount of additions that can be added as compared to BZO, and used as the basis for exploring this extension to additional materials more closely related to BSO.

2.4. Conclusion

Sectored targets with BaGeO_3 (BGeO) or BaSiO_3 (BSiO) wedges as well as pre-mixed targets of YBCO, BGeO or BSiO with appropriate compositions were used to deposit YBCO+BGeO and YBCO+BSiO films on (100) single crystal LaAlO_3 substrates. The cross-sectional transmission electron micrographs showed the presence of 20 nm diameter nanocolumns in the YBCO films of both the compositions. However, the critical transition temperature (T_c) of the films was found to significantly decrease. As a result, the critical current density (J_c) in applied magnetic fields was suppressed. With YBCO+2 vol% BGeO a self field J_c of 0.7 MA/cm² was observed. The YBCO+BGeO and YBCO+BSiO films made with lower concentrations of additions showed slight improvement in T_c indicating that the substitution of Ge and Si in the lattice is possibly responsible for the T_c depression. This study shows that in addition to the ability to form nanocolumns, the chemical compatibility of BaSnO_3 (BSO) and BaZrO_3 (BZO) as observed in YBCO+BSO and YBCO+BZO is critical to process high J_c YBCO films.

2.5. References

1. D. Larbalestier, A. Gurevich, D.M. Feldman and A. Polyanski, *Nature* 414 (2001) 368-377.
2. S.R. Foltyn, L. Civale, J.L. Macmanus-Driscoll, Q.X. Jia, B. Mairov, H. Wang and M. Maley, *Nat. Mater.* 6 (2007) 631-642.
3. J.L. MacManus-Driscoll, S.R. Foltyn, Q.X. Jia, H. Wang, A. Serquis, L. Civale, B. Maiorov, M.E. Hawley, M.P. Maley and D.E. Peterson, *Nat. Mater.* 3 (2004) 439-443.
4. S. Kang, A. Goyal, J. Li, A.A. Gapud, P.M. Martin, L. Heatherly, J.R. Thomson, D.K. Christen, M. Paranthaman and D.F. Lee, *Science* 311 (2006) 1911-1914.
5. C.V. Varanasi, J. Burke, H. Wang, J.H. Lee and P.N. Barnes, *Appl. Phys. Lett.* 93 (2008) 092501-092501-3.
6. C.V. Varanasi, P.N. Barnes, J. Burke, L. Brunke, I. Maartense, T.J. Haugan, E.A. Stinzianni, K.A. Dunn and P. Halder, *Supercond. Sci. Technol.* 19 (2006) L37-L41.
7. C.V. Varanasi, J. Burke, L. Brunke, H. Wang, J.H. Lee and P.N. Barnes, *J. Mater. Res.* 23 (2008) 3363-3369.
8. P. Mele, K. Matsumoto, A. Ichinose, M. Mukaida, Y. Yoshida, S. Horii and R. Kita, *Supercond. Sci. Technol.* 21 (2008) 125017-125017-6.
9. P.N. Barnes, M.D. Sumption and G.L. Rhoads, *Cryogenics* 45 (2005) 670-686.

10. C.V. Varanasi, J. Burke, L. Brunke, H. Wang, M. Sumption and P.N. Barnes, *J. Appl. Phys.* 102 (2007) 063909-063909-5.
11. J.P. Guha, *J. Mat. Sci.* 14 (1979) 1744-1748.
12. O. Yamaguchi, T. Niimi and K. Shimizu, *Mater. Lett.* 2 (1983) 119-121.

3. YBa₂Cu₃O_{7-x} coated Conductors on Ceraflex (Polycrystalline Flexible Yttria-Stabilized Zirconia) Substrates

3.1. Introduction

YBa₂Cu₃O_{7-x} (YBCO) coated conductors are presently being developed using conductive metallic substrates such as Ni-5 at% W or HastelloyTM [1, 2]. However, losses due to eddy currents appear when these conductors are used in ac applications. Non-conducting or highly-resistive substrates can avoid this issue for ac applications [3]. In addition, for cryo-electronic applications, YBCO films deposited on thermally- and electrically-insulating substrates are also of interest. Earlier work showed that YBa₂Cu₃O_{7-x} coatings can be grown on highly resistive flexible polycrystalline yttria-stabilized zirconia (YSZ) substrates with ion-beam assisted deposition (IBAD)-YSZ layers for RF cryo-electronic applications [4].

Polycrystalline YSZ substrates such as Ceraflex are commercially available in ultra thin, tough, flexible thin sheet form [5]. Sheets as thin as 0.05 mm thick and as large as 200 x 200 mm² are readily available. These substrates also have high hardness and fracture toughness three times higher in bending strength, two or three times in fracture toughness than alumina. Properties such as this would make the material suitable as substrates for coated conductors if the lengths can be increased.

Gnanarajan et al. reported that IBAD-YSZ layers and YBCO with a phi scan full width half maximum (FWHM) of 19° can be grown on Ceraflex substrates when coated with an additional silica coating to reduce surface roughness [6]. However, it is known that biaxial texture can develop in IBAD-MgO faster than IBAD-YSZ [7, 8]. Initial work by Lu et al. indicated that highly textured IBAD-MgO with a FWHM of 9.3° can indeed be grown on properly-prepared Ceraflex substrates using particular processing conditions [9, 10]. Here, we present initial results which indicate that biaxially textured YBCO can be grown on the IBAD-MgO buffered Ceraflex substrates using lanthanum manganate (LMO) cap layers deposited by pulsed laser ablation (PLD). Results on this YBCO/LMO/IBAD-MgO/Y₂O₃/SiO₂/Ceraflex architecture include biaxial texture of the layers, superconducting properties such as critical transition temperature (T_c), critical current density (J_c), microstructures and SIMS depth profile analyses of the coatings. Both Ceraflex 3Y with 3 mol% Y₂O₃ and Ceraflex 8Y with 8 mol% Y₂O₃ were used. In addition, mechanical properties of the Ceraflex substrates were measured and compared with published values of biaxially textured Ni-5 at% W and HastelloyTM substrates.

3.2. Experimental

3.2.1. Mechanical properties of Ceraflex substrates

The Ceraflex substrates are obtained from Marktech International Inc. [5]. Ceraflex 3Y strips also have good elasticity and high flexibility and are capable of bending to a radius of 8 mm. The Ceraflex 3Y substrates were sliced to a nominal tensile specimen size of 50.8 x 3.34 x 0.09 mm³. To prevent damage during the slicing operation, the substrates were hot-wax mounted and sandwiched between two microscope glass slides. The glass-sandwiched substrate was fed into a slow-speed, water cooled/lubricated, diamond-impregnated, slicing wheel rotating at ~100 rpm at a 0.25 mm/s feed rate. After slicing, the test specimens were unmounted and cleaned in toluene to remove the wax and further cleaned in acetone and methanol, and then dried. After

cleaning, the tensile specimens were optically inspected at 50 X for machining damage and edge chipping.

The Ceraflex tensile specimens were then tabbed with 12 x 12 x 0.762 mm³ (nominal) aluminum plates at the ends to prevent crushing of the thin ceramic specimens in the tensile grip. Each end of Ceraflex tensile specimen was glued with a general-purpose two-part epoxy and sandwiched with two aluminum plates as shown in Figure 3.1. The epoxy was allowed to cure for ~ 24 h to achieve maximum shear strength. The Ceraflex specimen tensile gage length after end tabbing was approximately 25 mm.

The width and thickness of the samples were measured before testing. The thickness was measured using a micrometer with debris-free flat anvils to prevent any surface damage to the tensile specimen. The width was measured optically using a calibrated microscope to prevent damage to the edge of the thin specimen. Typical variation in the sample widths is shown in Figure 3.1.

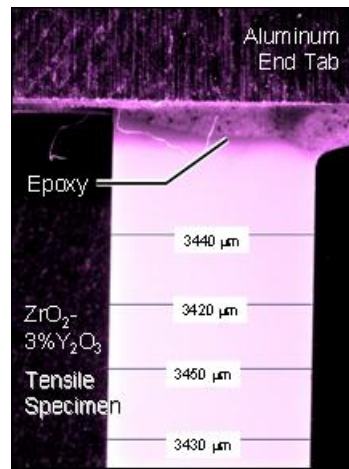


Figure 3.1. Optical macrograph of a Ceraflex tensile test specimen in aluminum tabs with width measurements

The tabbed Ceraflex tensile specimens were mounted on an aligned tensile wedge grip (Instron Model 2716-015) on a Universal testing system (Instron Model 4486 SN C8825) with a 1 kN load cell (Instron Load Cell SN: UK881). The tensile extension rate was 0.0212 mm/s (0.05 ipm). A total of three tensile specimens were tested to failure. After testing, the remnants of each test specimen were photographed to show that the fracture occurred between the end tabs as shown Figure 3.2. A simple tensile testing method originally developed for textured metallic substrates [11] was used to test these thin ceramic substrates.

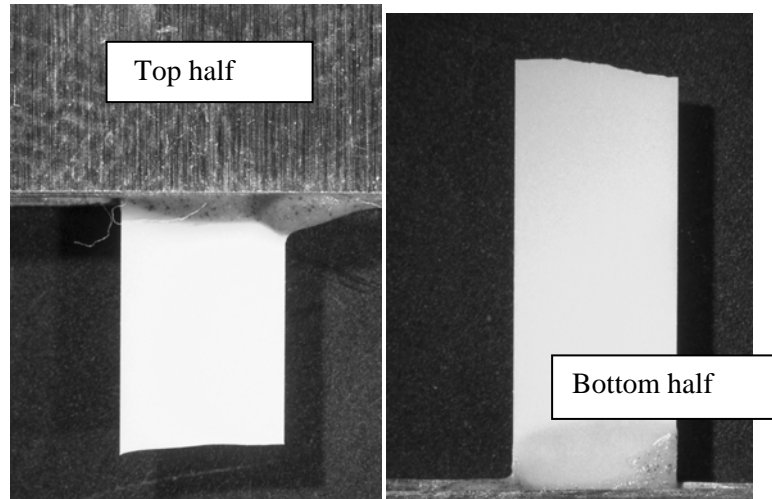


Figure 3.2. Optical macrograph of a tested Ceraflex tensile test specimen at the end of the test showing the fractured tensile gage section: (a) top half and (b) bottom half

3.2.2. Buffer layers (MgO, LaMnO₃) and YBCO

The Ceraflex 8Y substrates were initially spin coated with methyl siloxane polymers to make smooth SiO₂ coatings as described in detail elsewhere [6]. A thin amorphous Y₂O₃ buffer layer (15 – 40 nm thickness) was deposited by e-beam deposition and pre-exposed in Ar⁺ for 1 – 2 min on the initial SiO₂ layer. MgO of 9 – 11 nm thickness was deposited by IBAD at 1.5 Å/s, at room temperature using Ar⁺ beam operating at 750 eV and 10 mA. An ion-to-atom ratio of ~0.9 was maintained during deposition. A homo-epitaxial MgO layer of 100 – 200 nm thickness was grown at 0.5 – 1.0 Å/s, at 300 – 500 °C. *In-situ* real-time reflection high-energy electron deflection (RHEED) was used to monitor the texture development during IBAD-MgO and homo-epitaxial MgO depositions. A detailed discussion of the deposition conditions and characterization of these layers have been discussed elsewhere [10]. In the present study, LaMnO₃ (LMO) buffer layer and YBCO layer deposition and characterization is presented.

A LMO cap layer was deposited by pulsed laser ablation (PLD) on the MgO buffered Ceraflex substrates. A YBCO film was then grown by PLD on top of the LMO cap layer. The YBCO/LMO layers were also grown on MgO (100) single crystal substrates for comparison purposes. All the PLD depositions were done in a Neocera chamber. A Lambda Physik KrF excimer laser (wavelength $\lambda = 248$ nm) was used to deposit films at an energy density of 2 – 4 J/cm². A layer of LMO of ~200 nm thickness was first deposited at 750 °C in an atmosphere of 300 mTorr of O₂ at 4 Hz for 15 min, and then a layer of YBCO of ~300 nm thickness was deposited at 780 °C in an atmosphere of 300 mTorr of O₂, at 4 Hz for 20 min. The films were annealed inside the chamber in 600 Torr of oxygen at 500 °C for 30 min. before cooling down to the room temperature.

The YBCO coatings were characterized for biaxial texture using a four circle x-ray diffractometer. Characterization of the film's microstructure was done using a scanning electron microscope (SEM), the critical transition temperature (T_c) was characterized by ac susceptibility and the critical current density (J_c) using a Quantum Design physical property measurement system (PPMS) vibrating sample magnetometer. Compositional sputtered depth profiles of the

films were obtained with secondary ion mass spectrometry (SIMS) (CAMECA Model IMS4F7). The SIMS instrument employed Cs^+ primary ion bombardment at 5.5 keV and 42° incidence and detected positively-charged atomic ions with a mass resolution of $M/dM = 600$. The analyzed area was circular with a 60 μm diameter.

3.3. Results and Discussion

3.3.1. Mechanical properties

Tensile test results are summarized in Table 3.1. The average measured tensile yield and ultimate strength from three Ceraflex test specimens is 790 MPa with a standard deviation of 120 MPa. It is not surprising that the yield strength and the ultimate strength are same in Ceraflex as it is a brittle structural ceramic material and deforms only elastically and not plastically. It may be of concern that the standard deviation is slightly high; however, this is due to the sensitivity of the ceramics to cracks and other defects and this behavior is expected.

Table 3.1: Summary of Yield Strength Measurements

Material	Sample ID	Nominal Gage Length, mm	Displacement Rate, mm/min	Yield Strength, MPa	UTS, MPa	Width, mm	Thickness, mm
ZrO_2 - 3% Y_2O_3	1	25	1.270	650	650	3.442	0.090
	2	25	1.270	860	860	3.384	0.090
	3	25	1.270	850	850	3.343	0.090
	Average \pm Stdev			790 \pm 120	790 \pm 120		
Ni-5%W				163[Ref. 11] 176[Ref. 12]			
Hastelloy TM				464 [Ref. 12]			

Figure 3.3 shows the stress-extension curves of a Ceraflex substrate as compared to previously reported data [11] of Ni-5 at% W biaxially textured metallic substrate. The tensile yield strength of the Ceraflex substrate is higher than a similarly tested Ni-5 at% W substrate showing a steep slope in stress extension curve as the load was applied. As expected, the Ni-5 at% W substrate shows considerably more plastic deformation as compared to the Ceraflex substrates. Even so, the YS of the Ceraflex substrate was found to be almost five times higher than the YS of Ni-5 at% W substrate. Also as compared to the published data of HastelloyTM substrate [12], the YS data of Ceraflex substrates were found to be 1.5 times higher than that of HastelloyTM substrates as shown in Table 3.1.

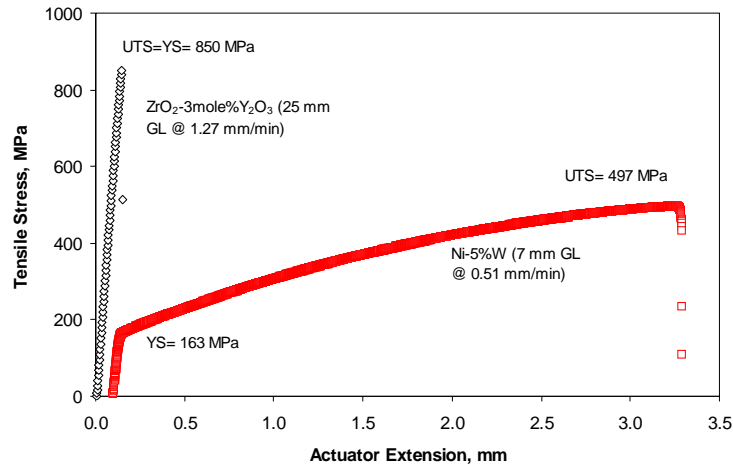


Figure 3.3. Stress-extension curves of a Ceraflex substrate compared with a stress-extension curve of a biaxially textured Ni-5 at% W substrate

3.3.2. Texture quality of YBCO

Intensity $\theta - 2\theta$ x-ray diffraction patterns of different YBCO/LMO/IBAD-MgO/Y₂O₃/SiO₂/Ceraflex samples are compared with the diffraction pattern of a YBCO/LMO/MgO single crystal sample in Figure 3.4. It can be seen that c-axis oriented YBCO layers are grown in both types of samples showing only (00 l)-type peaks from YBCO. As expected, peaks corresponding to the polycrystalline Ceraflex substrates were evident only in the Ceraflex substrate samples.

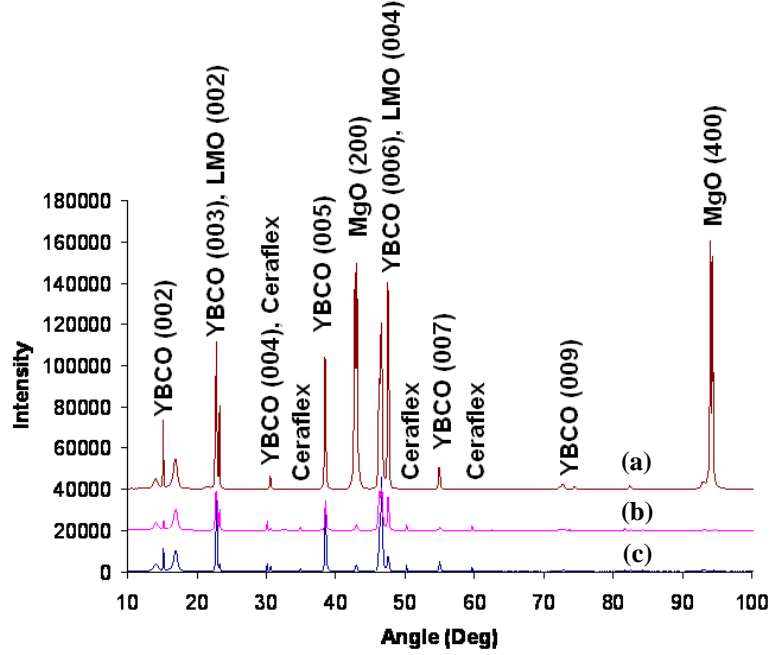


Figure 3.4. X-ray $\theta - 2\theta$ diffraction patterns of (a) YBCO/LMO/single crystal MgO, and (b) and (c) two different samples of YBCO/LMO/IBAD-MgO/Y₂O₃/SiO₂/ Ceraflex

Figure 3.5 (a) shows the (110) phi scans of the YBCO/LMO/single crystal MgO substrate. A very low FWHM of 1.4° observed for the YBCO films indicates the presence of high-quality biaxial texture. However, a (110) phi scan of YBCO on the YBCO/LMO/IBAD-MgO/Y₂O₃/SiO₂/Ceraflex sample, as shown in Figure 3.5 (b), does show that the FWHM is wider in these films. For this sample, a FWHM of 6.75° was measured. Although this value is greater than what was achieved on the single-crystal substrate, the FWHM is comparable to what is generally observed in YBCO films grown on textured metallic substrates [13]. Omega scans of YBCO (200) taken on these samples also show c-axis out of plane alignment with a FWHM of $\sim 5^\circ$ in both longitudinal as well as transverse directions as shown in Figure 3.6 (a) and 3.6 (b), again indicating that YBCO films with good biaxial texture can be grown on the Ceraflex substrates using the present architecture.

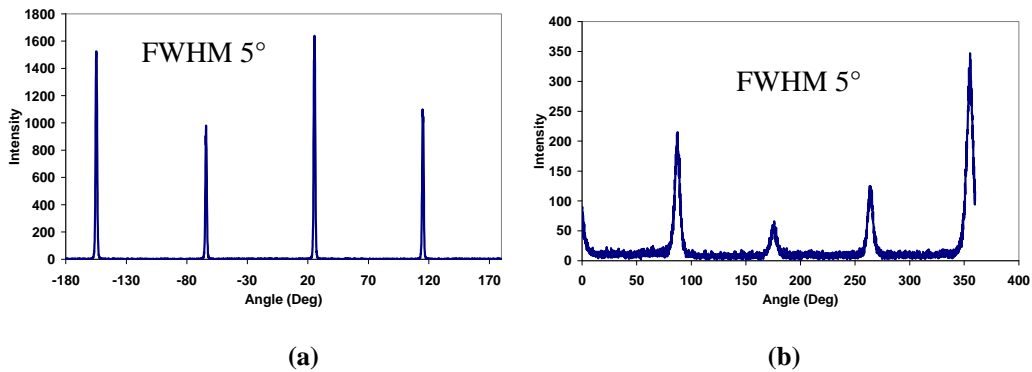


Figure 3.5. Phi scans of (110) YBCO on (a) YBCO/LMO/ single crystal MgO, and (b) YBCO/LMO/IBAD-MgO/Y₂O₃/ SiO₂/ Ceraflex

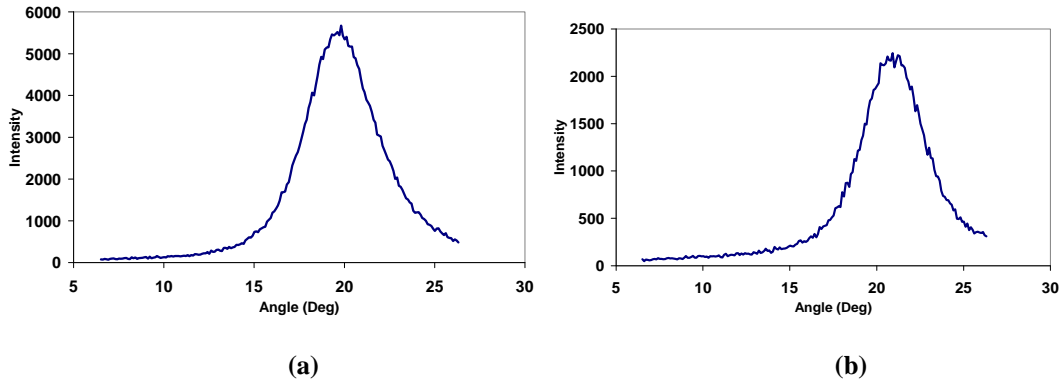


Figure 3.6. (200) YBCO Omega scans of YBCO/LMO/IBAD-MgO/Y₂O₃/SiO₂/Ceraflex in (a) longitudinal and (b) transverse directions

3.3.3. Microstructure of YBCO

Figure 3.7 shows a scanning electron micrograph of YBCO/LMO/IBAD-MgO/Y₂O₃/SiO₂/Ceraflex sample. It can be seen that YBCO grows with a typical plate-like microstructure. The average grain size was found to be 2 – 5 μm . In addition to the ab-oriented grains, some growth of a-axis grains was also observed in the films, which may account for the slight degradation of the observed J_c as discussed later. Reduction in the amount of a-axis grains can be achieved by adjusting the deposition temperature during processing [14].

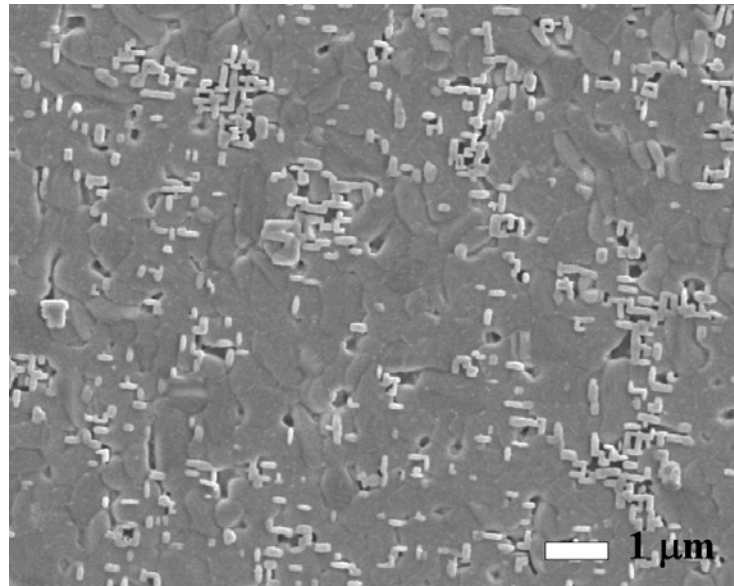


Figure 3.7. Scanning electron micrograph of a YBCO/LMO/IBAD-MgO/Y₂O₃/SiO₂/ Ceraflex sample

3.3.4. Superconducting properties of YBCO layers

The T_c of the YBCO films measured by ac susceptibility showed that a high T_c , above 91 K, is possible in the YBCO/LMO/single crystal MgO sample as shown in Figure 3.8 (a). The YBCO/LMO/IBAD-MgO/Y₂O₃/SiO₂/Ceraflex samples (Figure 3.8 (b)) have a slightly lowered T_c , 88.5 K, and broader transitions compared to the YBCO/LMO/single crystal MgO. The presence of a broad transition width in the ac susceptibility data indicates that the YBCO films may have a lower J_c [15]. The magnetization critical current density (J_c) of the YBCO/LMO/IBAD-MgO/Y₂O₃/SiO₂/Ceraflex films measured at 77 K and 65 K are shown in Figure 3.9. A self field J_c of 0.25 MA/cm² at 77 K and J_c close to 1 MA/cm² at 65 K self field was noted in these films using Bean's model and the measured magnetic moment. The observed reduction in J_c in these films as compared to YBCO grown on single crystal substrates (typically > 1 MA/cm²) can be due to several factors, including the lower T_c and a-axis grain growth observed in the films.

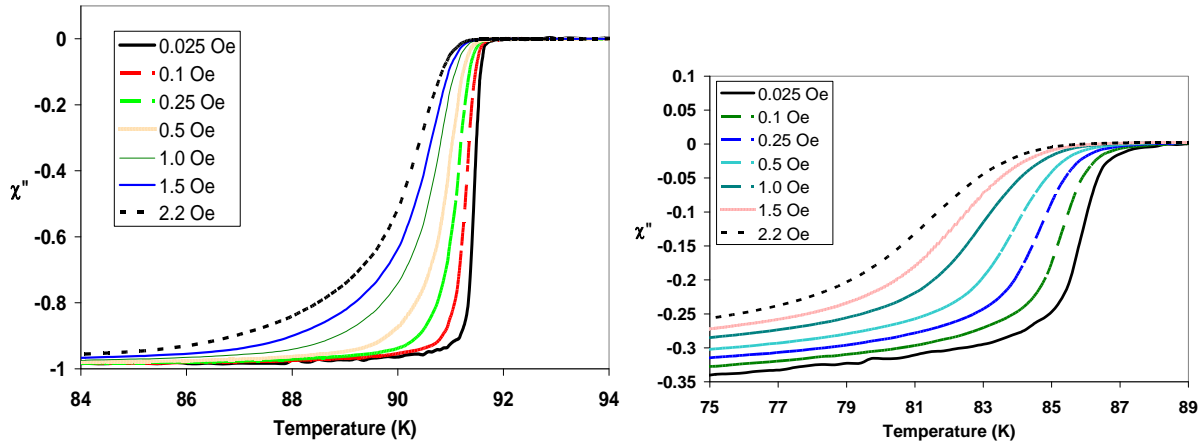


Figure 3.8. AC susceptibility curves of (a) YBCO/LMO/single crystal MgO and (b) YBCO/LMO/IBAD-MgO/Y₂O₃/SiO₂/Ceraflex

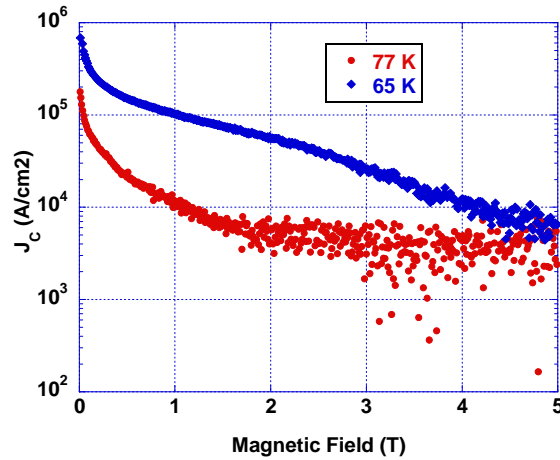


Figure 3.9. Magnetization J_c data as a function of applied magnetic field of YBCO/LMO/IBAD-MgO/Y₂O₃/SiO₂/Ceraflex sample at 77 K and 65 K

To further understand the reasons for the reduction in T_c and J_c in these films, compositional depth profiling was performed using SIMS. Figure 3.10 shows a sputtered depth profile acquired from a YBCO/LMO/IBAD-MgO/ Y_2O_3 /SiO₂/Ceraflex sample. In this figure, all elemental signals are plotted on a linear scale, with each signal normalized to its own maximum intensity, so as to best indicate composition. The interfaces in the sputtered profile show some broadening, or non-infinite slope. Both elemental inter-diffusion and roughness of the film surface and/or film interfaces can contribute to these interface slopes in the observed profile. While some roughness is expected, the signals from the YBCO elements show a second, even less steep interface slope at sputter times just beyond an inflection in the signals, at approximately 300 nm of sputter time. This secondary slope indicates elemental interdiffusion between the YBCO and LMO. Also, Mg is seen to diffuse from the MgO layer, as revealed by the broader slope of the Mg signal into LMO compared to the slope of the La and Mn signals into the MgO. Furthermore, the Mg has diffused well into the LMO layer, as evidenced by the substantial penetration of the Mg signal into the LMO layer, when compared to its lack of penetration into the SiO₂ layer. It can also be observed in the SIMS data that the relative ratio of La/Mn signals is not constant in the LMO layer. It is thought that this is not due to artifact of depth profiling but probably caused by Mg diffusion in to LMO and its substitution in the lattice.

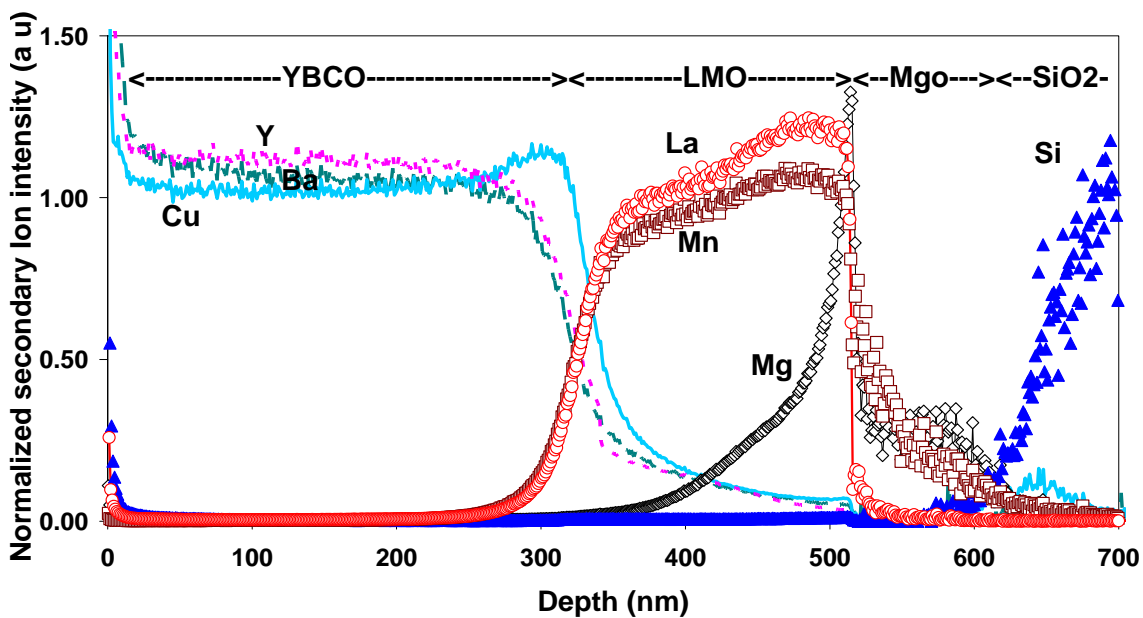


Figure 3.10. SIMS depth profile analyses of a YBCO/LMO/IBAD-MgO/ Y_2O_3 /SiO₂/ Ceraflex sample

The diffusion of La and Mn into the YBCO matrix, especially via the grain boundaries, can potentially reduce the T_c and J_c of the YBCO films. Even though the biaxial texture of YBCO was shown to be good, elemental inter-diffusion causing chemical substitutions could adversely

affect the superconducting properties. However, a LMO layer of similar thickness deposited on an MgO single crystal yielded high quality YBCO using the same processing conditions. This suggests that the elemental interdiffusion is not contingent on the LMO chemical composition used or on the subsequent processing conditions used after the IBAD layer is deposited.

It is possible that the small grain size of the IBAD-MgO on these Ceraflex samples makes it more reactive, resulting in its interdiffusion into the LMO as compared to LMO on single crystal MgO deposition under the same deposition conditions. Different deposition methods like SuperPower Inc. processes have produced YBCO coated conductors of excellent quality using an intermediate LMO layer on top of a homo-epitaxial MgO layer [16]. Similar results have also been demonstrated by Oak Ridge National Laboratory [17]. It can then be expected that optimization of the deposition conditions should correct the interdiffusion issue, especially since the biaxial texture is good and high J_c (2.5×10^5 A/cm²) was readily achieved on the initial Ceraflex sample with little optimization. Possible changes to the processing conditions used in the present work include making the LMO layer thicker or lowering the deposition temperature to reduce the observed interdiffusion. Importantly, the data presented here shows that highly textured YBCO with reasonable superconducting properties can be grown with little process optimization on polycrystalline flexible YSZ substrates using IBAD-MgO as template layers and LMO as a cap layer.

It is expected that further refinement of the processing parameters can further improve the superconducting properties. The results discussed in the present report are believed to be useful not only for the coated conductor applications development but also for cryo-electronic applications or microwave filters. In other words, in the applications where a non-conducting substrate and a textured superconducting film are preferred, the MgO buffered ceraflex substrates can be very useful. The future research may include mechanical property testing of YBCO on Ceraflex substrates to determine if the properties of the conductors remain the same as the substrates or change due to the additional processing. Additionally, AC loss testing of the conductors made using Ceraflex substrates will be also useful, to determine the advantages of using these substrates over conducting metallic substrates.

3.4. Conclusion

Biaxially textured $\text{YBa}_2\text{Cu}_3\text{O}_{7-x}$ (YBCO) films were grown on polycrystalline flexible yttria stabilized zirconia (YSZ) ceramic substrates (Ceraflex) buffered with MgO and LaMnO_3 layers. These substrates were initially coated with silica glass to obtain a smooth surface and then biaxially textured MgO buffer layers were deposited by ion-beam assisted deposition (IBAD-MgO). LaMnO_3 (LMO) cap layers and YBCO layers were then deposited by the pulsed laser ablation method. Highly-textured YBCO films with a full width half maximum (FWHM) of 6.75° in (110) phi scans and a FWHM $\sim 5^\circ$ in (200) omega scans were obtained. An initial deposition yielded samples with a $T_c > 88$ K and a self-field magnetization J_c of 2×10^5 A/cm² at 77 K. A secondary ion mass spectrometry (SIMS) depth profile of the samples indicated that with the present a deposition condition, some La and Mn, Mg diffusion into the YBCO layers is possible and this may reduce the J_c in the self-field. The yield strength (YS) of uncoated Ceraflex substrates was compared with that of metallic substrates and it was found that Ceraflex substrates can have a YS at least 4 – 5 times higher than the YS of biaxially textured Ni-5 at%W

substrates and ~1.5 times that of Hastelloy™ substrates. This work demonstrates the feasibility of using Ceraflex as a substrate in YBCO coated conductors or electronic applications in instances where it is desirable to have a nonconducting substrate.

3.5. References

1. X. Li, M.W. Rupich, T. Kodenkandath, Y. Huang, W. Zhang, E. Siegal, D.T. Verebelyi, U. Schoop, N. Nguyen, C. Thieme, Z. Chen, D.M. Feldman, D.C. Larbalestier, T.G. Holesinger, L. Civale, Q.X. Jia, V. Maroni and M.V. Rane, *IEEE Trans. Appl. Supercond.* 17 (2007) 3553.
2. X. Xiong, K.P. Lenseith, J.L. Reeves, A. Rar, Y. Qiao, R.M. Schmidt, Y. Chen, Y. Li, Y.-Y. Xie and V. Selvamanickam, *IEEE Trans. Appl. Supercond.* 17 (2007) 3375.
3. P.N. Barnes, M.D. Sumption and G.L. Rhoads, *Cryogenics* 45 (2005) 670.
4. K.S. Harshavardhan, H.M. Christen, S.D. Silliman, V.V. Talanov, S.M. Anlage, M. Rajeswari and J. Classen, *Appl. Phys. Lett.* 78 (2001) 1888.
5. <http://www.mkt-intl.com/electrochem/pages/cereflex.html>.
6. S. Gnanarajan and J. Du, *Supercond.Sci.Technol.* 18 (2005) 381.
7. C.P. Wang, K.B. Do, M.R. Beasley, T.H. Geballe and R.H. Hammond, *Appl. Phys. Lett.* 71 (1997) 2955.
8. S. Kreiskott, P.N. Arendt, J.Y. Coulter, P.C. Dowden, S.R. Foltyn, B.J. Gibbons, V. Matias and C.J. Sheehan, *Supercond. Sci. Technol.* 17 (2004) S132.
9. R. Lu, R.N. Vallejo, D.W. Fisher and J.Z. Wu, *Appl. Phys. Lett.* 89 (2006) 132505.
10. R. Lu, J.Z. Wu, C. Varanasi, J. Burke, I. Maartense and P.N. Barnes, *J. Electr. Mater.* 36 (2007) 1258.
11. C.V. Varanasi, L. Chuck, L. Brunke, J. Burke, A.D. Chaney and P.N. Barnes, *J. Electr. Mater.* 36 (2007) 1265.
12. C.C. Clinker, J.W. Ekin, N. Cheggour, C.L.H. Thieme, Y. Qiao, Y.-Y. Xie and A. Goyal, *Cryogenics* 46 (2006) 432.
13. D.T. Verebelyi, U. Schoop, C. Thieme, X. Li, W. Zhang, T. Kodenkandath, A.P. Malozemoff, N. Nguyen, E. Siegel, D. Buczek, J. Lynch, J. Scudiere, M. Rupich, A. Goyal, E.D. Specht, P. Martin and M. Paranthaman, *Supercond. Sci. Technol.* 16 (2003) L19.
14. A. Ibi, H. Iwai, K. Takahashi, T. Muroga, S. Miyata, T. Watanabe, Y. Yamada and Y. Shiohara, *Physica C* 426 (2005) 910.
15. P.N. Barnes, I. Maartense, T.L. Peterson, T.J. Haugan, A.L. Westerfield, L.B. Brunke, S. Sathiraju and J.C. Tolliver, *Mat. Res. Soc. Symp. Proc.* XS-3 (2004) EE6.4.1-3.
16. X. Xiong, K.P. Lenseith, J.L. Reeves, A. Rar, Y. Qiao, R.M. Schmidt, Y. Chen, Y. Li, Y.-Y. Xie and V. Selvamanickam, *IEEE Trans. Appl. Supercond.* 17 (2007) 3375.
17. M.P. Paranthaman, T. Aytug, H.Y. Zhai, L. Heatherly, A. Goyal and D.K. Christen, *Supercond. Sci. Technol.* 18 (2005) 223.

4. Carbon Nanotubes Growth and Characterization for Electrical and Thermal Applications: Constantan (Ni-Cu-Mn Alloy) Metallic Substrates without Adding Additional Catalysts

4.1. Introduction

Carbon nanotubes first imaged by Iijima in 1991 [1] are now being investigated worldwide for many potential applications in several fields such as electronic, thermal, biomedical, composite, field emission, sensors, etc. due to their unique properties [2]. With regards to many industrial and government agencies, particularly the U.S. Air Force, thermal management has become a very important issue in recent years for improving device reliability and increasing the performance of existing devices. In most devices, heat dissipation remains as an increasing problem with decreases in the sizes of the integrated circuits and increases to the power density. Unless developments in thermal management technology occur in parallel, the continued enhancements in the performance of these devices are threatened. Nano-engineered materials are currently being developed to make more efficient thermal interfaces to address these thermal management problems. Carbon nanotubes (CNTs) with very high thermal conductivity are very attractive for developing thermal interface materials (TIMs). Although significant progress has been made in understanding the growth mechanism of CNTs, the control over the chirality of CNTs still remains as a significant challenge and an active continuing area of research. While there are several methods of manufacturing CNTs [3, 4] being investigated, one of the common methods used to grow CNTs on a variety of substrates is chemical vapor deposition (CVD) using C_2H_2 or CH_4 as precursors.

Metallic nanoparticles such as Fe, Ni, etc. are deposited on the substrates prior to the carbon deposition to act as catalysts during the CVD process [3]. However, in this approach the adhesion of CNTs to the substrates can sometimes be problematic as the nanoparticles are not integrated into the substrate. One means to overcome this problem is the use of metallic substrates to grow CNTs without the additional processing step of adding nanoparticle catalysts. In the literature pure Ni substrates have been reported to be used to grow CNTs [5, 6] with some success. In some other studies, Ni and other metallic substrates were used with additional catalysts to improve the density of CNTs [7, 8]. Stainless steel [9] or aluminum [10] were also used as substrates but were given prior treatments to create catalyst islands on these substrates to grow CNTs.

In this present research study, rolled and annealed commercially available constantan (Cu55-Ni44- Mn1 wt%) alloy substrates with a well defined grain structure were investigated as an alternate substrate to grow CNTs. No additional catalysts were added to the substrates. Experiments were conducted to determine if it is possible to grow high density CNTs on these substrates. As opposed to a pure Ni metal, an alloy with the precipitates of the alloying additions and other defects such as grain boundaries, etc. may provide the necessary and appropriate nucleation sites for the high density of CNT growth.

4.2. Experimental

A vertical thermal CVD reactor was built in house to grow CNTs. Initially the CNTs were grown at atmospheric pressure using C_2H_2 /Ar mixtures. Prior to deposition, the quartz tube of the reactor was purged with Argon gas with a flow rate of 300 sccm, for 30 min. The

temperature was then ramped up to 700 °C in Ar gas flowing at a rate of 300 sccm. The CNTs were grown on different substrates in an Argon/Acetylene (10%) gas flowing at a rate of 30 – 300 sccm for 2 – 10 min. The precursor gas was subsequently purged using Argon gas at a flow rate of 300 sccm for 30 min. at the end of the growth and the furnace was cooled down to room temperature in flowing Argon gas at 300 sccm.

To determine the quality of CNTs grown in the home built CVD reactor, CNTs were grown on Si substrates decorated with Ni islands. Pulsed laser deposition (PLD) was used to deposit Ni islands on Si substrates. A Lambda Physik KrF excimer laser (wavelength $\lambda = 248$ nm) was used to deposit Ni films in a Neocera PLD chamber. The deposition was carried out using an energy density of 2 J/cm² at a 20 Hz repetition rate at room temperature in an Argon gas pressure of 300 mTorr. A thin film of Ni was deposited for 30 sec to 3 min. and then the Si substrate was annealed at 750 °C for 30 min. in Ar/ 4% H₂ gas mixture to break the film into islands. These substrates as well as several as rolled and annealed (500 °C, 3 h and 1200 °C for 2 h) constantan substrates were investigated to grow CNTs. It has been shown earlier that different heat treatments would produce different degree of (100) texture and grain size in constantan substrates [11]. The annealed as well as rolled metallic substrates were roughened by either mechanical grinding using 600 grit SiC paper or by ion milling for 10 – 15 min.

Scanning electron micrographs of CNTs grown on various substrates were taken using a FEI Sirion scanning electron microscope as well as a Hitachi S-4800 High Resolution Scanning Electron Microscope. Transmission electron microscopy was done using a Philips CM200 electron microscope as well as Hitachi H – 7600 Transmission Electron Microscope. Raman spectroscopy was used using a Renishaw inVia Reflex Spectrometer System. The excitation source was a 300 mW red laser of wavelength 785 nm.

4.3. Results and Discussion

Figure 4.1 shows the SEM photomicrograph of a Si substrate with Ni islands deposited by PLD method. After the annealing treatment, Ni islands of 10 – 50 nm were formed as can be seen in this micrograph. Figure 4.2 shows the plan view of the CNTs grown on the same substrate. A very high density of several micron long CNTs of ~ 20 nm – 50 nm diameters can be seen in this micrograph. Figure 4.3 shows the cross-sectional SEM of a similar sample and the CNTs were found to be random but extend to more than 2.5 μ m thickness. No preferential alignment was noticed due to low density of islands. In addition, the turbulence of the precursor gases in a vertical CVD reactor is thought to be partly responsible for the lack of alignment of the CNTs. The processing parameters are not yet optimized to reduce the Ni island size or to produce the CNTs of uniform diameter. However, these results on the Si substrates served the purpose of evaluating the present CVD reactor with the aforementioned set of processing conditions for use in investigating whether constantan can be used as a substrate.

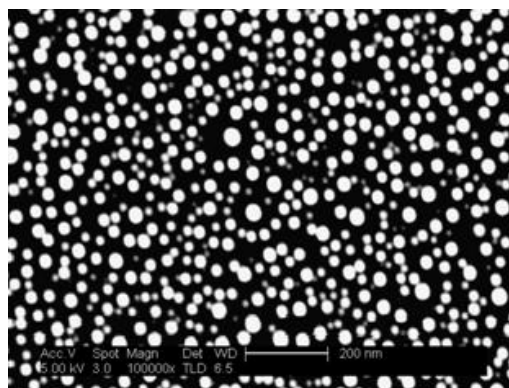


Figure 4.1. Scanning electron micrograph of a Si substrate sample with Ni islands deposited using a pulsed laser ablation method and then annealed

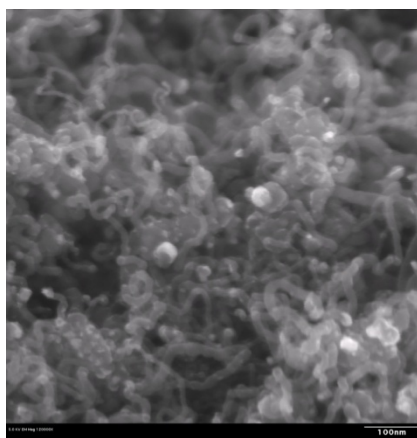


Figure 4.2. Scanning electron micrograph showing CNTs on the Si substrate sample decorated with Ni islands presented in Figure 4.1

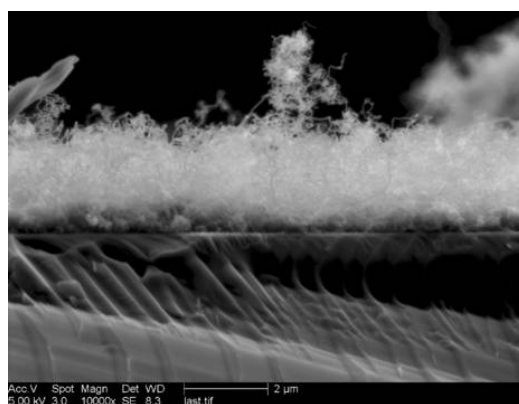


Figure 4.3. Cross-sectional SEM of the same sample showing the thickness of the CNT mat grown on the Si substrate with PLD deposited Ni islands

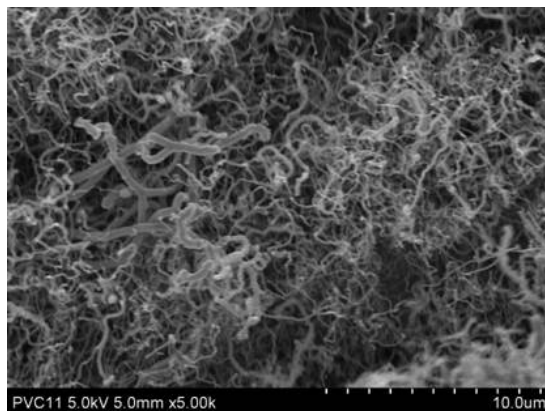


Figure 4.4. CNTs grown on a rolled and low temp annealed (500 °C, 3 h), mechanically roughened, constantan substrate

Figure 4.4 shows the CNTs grown on rolled and low temp annealed (500 °C, 3 h) constantan substrates of a 50 μm thickness when similar processing conditions are used as for the Si substrate. A very high density of CNTs of varying diameters (20 – 100 nm) can be seen to grow on these substrates similar to the Si substrates decorated with Ni islands as shown in Figure 4.2. Even though the substrate was roughened using a 600 grit SiC paper as mentioned before, it was thoroughly cleaned in an ultrasonic cleaner prior to the CVD growth to prevent any residual particles from remaining on the substrate. Therefore, it is believed that the Ni and Mn that is integral to the constantan substrate serves as the catalysts to grow the CNTs and not the SiC residue.

Figure 4.5 shows CNTs grown on high temp annealed constantan substrate (1200 °C, 2 h) that were roughened using an ion milling process. The CNTs grown on this substrate are much denser and narrower in the diameters than compared to the substrates that were grown on mechanically polished substrate as shown in Figure 4.4. Although ion milling is not an economical way to roughen CNTs, the present results indicate that surface roughening/preparation plays an important role in determining the diameter of the CNTs. It further justifies the previous hypothesis that SiC residue of the mechanically polished substrate does not play a major role if any in the CNT growth. It was also noted that CNTs can be processed on as rolled constantan substrate with a different surface texture than the annealed substrates as shown in Figure 4.6. The ability to provide partial optimization of the CNTs produced to a desired quality through proper substrate treatment is presently under further investigation.

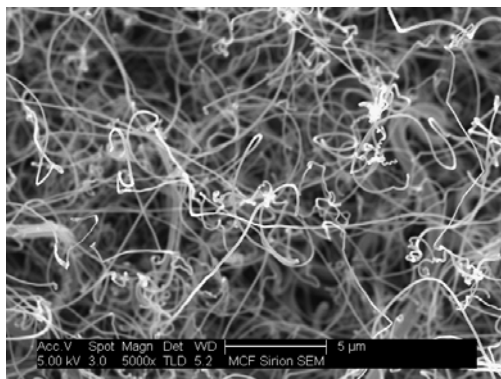


Figure 4.5. CNTs grown on a rolled and high temp annealed (1200 °C, 2 h), ion milled constantan substrate

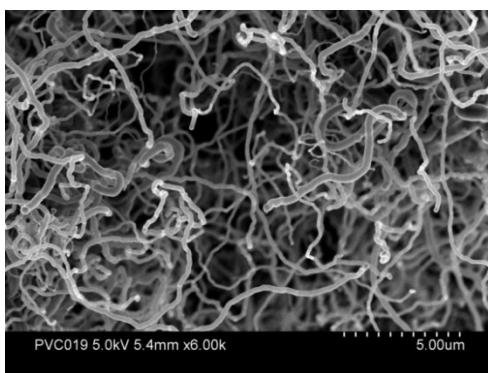


Figure 4.6. CNTs grown on as rolled, mechanically grinded constantan substrate

Figure 4.7 show the TEM images of the CNTs grown on the constantan substrates. While the tubular nature is clear from the pictures, the inner walls were not able to be imaged clearly. It appears that there could be some amorphous carbon present on the surface of the tubes with the present set of conditions used and probably interferes with the imaging of the inner walls. Experiments are underway to reduce the amorphous carbon on the surface of the CNTs and to improve the TEM sample preparation. The TEM figures provided in Figure 4.8 indicate that tip growth in addition to root growth can potentially occur in the CNTs grown on the metallic substrates.

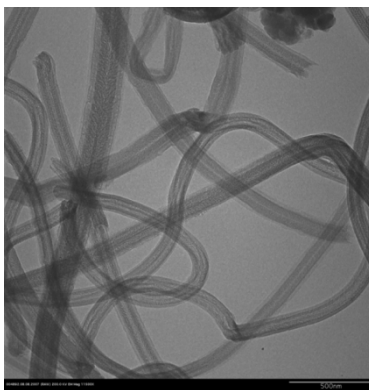


Figure 4.7. Transmission electron micrograph of CNTs grown on high temp annealed (1200 °C, 2 h), ion milled constantan substrates

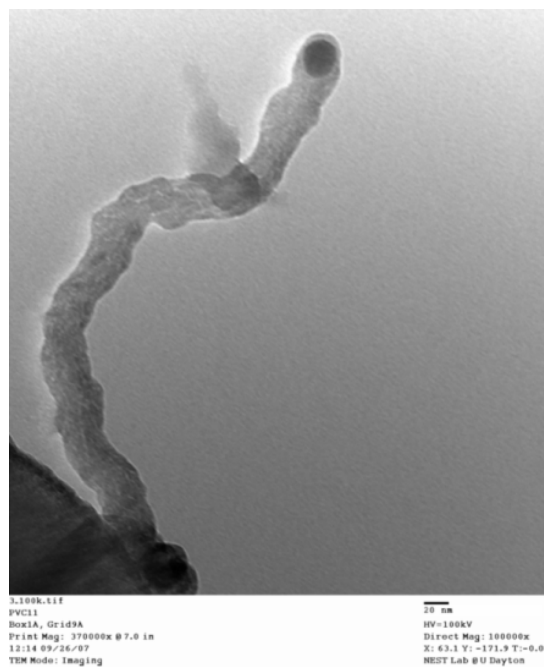


Figure 4.8. Transmission electron micrograph of CNTs showing tip growth mechanism may also be possible in the constantan substrates

The Raman spectra show the presence of the G band (peak at $\sim 1580 \text{ cm}^{-1}$) and D band (peak at $\sim 1320 \text{ cm}^{-1}$) peaks commonly observed for carbon materials in all the samples processed on the metallic substrates with varying relative intensities. The intensity of G/D seem to vary showing very high G/D ratio in as rolled substrates and very low value for ion milled roughened constantan substrates as shown in Figure 4.9. This further indicates that the surface preparation of the substrates is very important in determining the quality of the CNTs in constantan substrates. Even so, all the substrates indicate that the constantan can be used to produce CNTs without an additional treatment to nucleate catalyst particles.

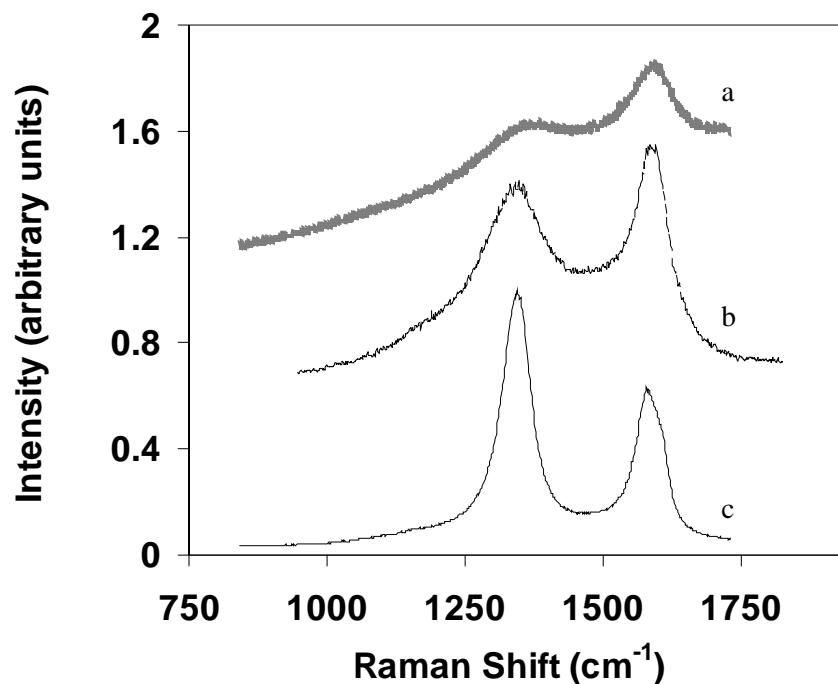


Figure 4.9. Raman spectra of CNTs grown on three different substrates: (a) constantan substrate annealed and then ion milled to roughen, (b) constantan substrate annealed and mechanically grinded to roughen, and (c) constantan substrate on as rolled condition and mechanically grinded

4.4. Conclusion

High density CNTs were grown on Si substrates with Ni islands (deposited by PLD) in a vertical CVD reactor using C_2H_2 precursor as well as on as rolled and annealed constantan substrates. In this research study, metallic constantan (Cu55-Ni44-Mn1 wt%) alloy substrates were investigated as an alternate choice of substrates to grow carbon nanotubes (CNTs). No additional catalysts were used other than the as rolled and annealed substrates to process CNTs on them. A high density CNTs growth was observed to take place on these substrates when suitable conditions were used in a thermal chemical vapor deposition (CVD) furnace with C_2H_2 as the carbon precursor. The CNTs also show both tip and root growth mechanisms on these constantan substrates. Scanning electron microscopy and transmission electron microscopy on these samples indicated the presence of several micron long CNTs ranging in 15 – 100 nm in diameter. Raman spectra taken from the samples confirmed the presence of G band peaks (peak at $\sim 1580\text{ cm}^{-1}$) and D band peaks (peak at $\sim 1320\text{ cm}^{-1}$) commonly observed in CVD grown multi-wall CNT samples with varying intensity ratios depending upon the processing conditions.

4.5. References

1. S. Iijima, *Nature* 354 (1991) 56.
2. R.H. Baughman, A.A. Zakhidov and W.A. de Heer, *Science* 297 (2002) 787.

3. A.V. Melechko, V.I. Merkulov, T.E. McKnight, M.A. Guillorn, K.L. Klein, D.H. Lowndes and M.L. Simpson, *J. Appl. Phys.* 97 (2005) 041301.
4. M. Endo, T. Hayashi, Y.A. Kim and H. Muramatsu, *Jpn. J. Appl. Phys.* 45 (2006) 4883.
5. E.F. Kukovitsky, S.G. Lvov, N.A. Sainov, V.A. Shustov, *Appl. Surf. Sci.* 215 (2003) 201.
6. N.K. Reddy, J. Meunier and S. Coulombe, *Mater. Lett.* 60 (2006) 3761.
7. C. Du and N. Pan, *Mater. Lett.* 59 (2005) 1678.
8. K. Oura, M. Katayama, S. Honda, K. Lee, N. Hayashi, T. Hirao, K. Endo, M. Kimoto, K. Nishimura and K. Nishio, *Jpn. J. Appl. Phys.* 42 (2003) L1167.
9. D. Park, Y.H. Kim and J.K. Lee, *Carbon* 41(2003) 1025.
10. Ch. Emmenegger, P. Mauron, A. Züttel, Ch. Nutzenadel, A. Schneuwly, R. Gallay and L. Schlapbach, *Appl. Surf. Sci.* 162 (2000) 452.
11. C.V. Varanasi, L. Brunke, J. Burke, I. Maartense, N. Padmaja, H. Efstathiadis, Chaney and P.N. Barnes, *Supercond. Sci. & Technol.* 19 (2006) 896-901.

5. Carbon Nanotubes Growth and Characterization for Electrical and Thermal Applications: Diamond Substrates

5.1. Introduction

Two carbon based materials have demonstrated the potential for high thermal conductivity: diamonds and carbon nanotubes (CNTs). Due to the high thermal conductivity (~ 1800 W/Km) of diamond, heat spreaders made of diamond plates are useful for thermal management in high power electronic devices [1] such as laser diodes, RF power transistors, etc. Diamond heat spreaders help to quickly remove the heat from the devices to the heat sinks and thus improve the reliability and device performance [2]. These characteristics may have a profound impact on developments that could lead to an improved electrical-thermal management system for optimized performance adaptive to all required U.S. Air Force operational conditions. Thus, a critical AFRL-INVENT (Integrated Vehicle Energy Technology) thrust area, Adaptive Power and Thermal Management Systems, will also be addressed.

Diamond coatings deposited by chemical vapor deposition (CVD) were investigated to serve as heat spreading films for thermally limited high-power high-frequency GaN-FET devices [3] as well. In addition to diamond films, discrete CNTs also were found to have very high thermal conductivity (~ 3000 W/Km) and high mechanical compliance thus offer a potential for the development of the next generation thermal interface materials [4-6]. CNTs can make excellent thermal interface materials if the proper quality can be maintained along with a robust attachment to the desired devices. For example, chip cooling with CNT microfin architectures have been recently proposed by Kordas et al. [5]. CNT films as thermal interface materials were also discussed by Zhu et al. [6]. Initial results by this group showed that an assembly with CNTs has a thermal conductivity of 81 W/m-K and a thermal resistance of $0.43 \text{ cm}^2\text{-K/W}$.

As an interface material, CNTs have been demonstrated to grow on a variety of materials/substrates. Cola et al. studied the performance of a thermal interface material consisting of Cu foil and CNT arrays and reported that thermal interface resistances of less than $10 \text{ mm}^2\text{-K/W}$ are possible [7]. Xu et al. [8] reported enhancements in thermal conductance using CNT arrays grown on Si wafers by plasma enhance chemical vapor deposition and reported a thermal interface resistance of $19.8 \text{ mm}^2\text{-K/W}$. Cola et al. [9] investigated CNT arrays grown on SiC to serve as thermal interface materials for high temperature SiC devices and achieved thermal resistances less than $10 \text{ mm}^2\text{-K/W}$. CNTs were grown on both sides of metallic substrates to fabricate thermal interface materials by Wang et al. [10].

Samples fabricated in this research study were measured to have thermal interface resistance of $12 \text{ mm}^2\text{-K/W}$. CNTs were also grown on constantan substrates without using catalysts [11] for similar applications. Carbon nanofiber-Cu composite films have been reported to have very low thermal resistances ($0.25 \text{ cm}^2\text{-K/W}$) to serve as thermal interface materials for microelectronic packaging by Ngo et al. [12].

It is therefore reasonable to consider the growth of CNTs on diamond since both can have superior thermal conductance. A structure containing a composite of diamond substrates for heat spreading and CNTs for heat radiation on top of them could provide a useful combination to conduct away the heat efficiently. By combining CNTs grown on diamond substrates, thermal diffusivity properties of the diamond spreaders can be expected to be enhanced. In the present

work, initial results of growth and characterization of CNTs grown on diamond substrates are presented.

5.2. Experimental

Diamond substrates were grown in a 5 kW Microwave Plasma Chemical Vapor Deposition (MPCVD) system on 2 in. diameter Si wafers. Prior to the diamond growth, the Si wafers were thoroughly cleaned and scratched with diamond crystals (pre-seeding) in an ultrasonic bath to initiate nucleation [13]. Diamond growth was carried out in a low concentration of CH_4 (1.5 – 2%) as the carbon source gas in a carrier gas of H_2 . Diamond films were grown using microwave powers between 2500 – 4000 W at temperatures of 850 – 900 °C for 6 – 7 d to obtain films of ~100 μm thickness. Free standing diamond substrates were subsequently obtained by dissolving away the Si wafer using chemical etchants. Catalyst layer (Ni or Ni-9%W-1.5% Fe) were then deposited by sputtering directly on to the diamond substrates without using any intermediate layers. All the depositions were done at room temperature and the metal catalyst layers from 2 – 10 nm thickness were deposited by varying the deposition time. While some samples were treated in Ar/5 % H_2 atmosphere for 30 min. to create catalyst islands prior to CNT growth, other samples were directly used for CNT growth without a prior heat treatment.

CNT growth was done in a lab constructed thermal CVD system using a 1 in. dia. quartz tube in a horizontal furnace. Initially, the tube furnace was evacuated by using a rough pump and then purged with Ar/5% H_2 for 20 min. The furnace with the samples was heated in an Ar/5 % H_2 atmosphere to 750 °C – 800 °C. Precursor gases of 10 vol.% C_2H_2 in an argon carrier gas was introduced as the carbon source at a flow rate of 50 – 400 sccm. The CNT's were grown for different lengths of time varying from 30 to 120 min. The samples were then cooled in an Ar/5% H_2 mixture to room temperature. Some samples were also grown at a total pressure of 90 Torr to observe the effect of low pressure growth.

Both diamond and CNT/diamond samples were analyzed by using a high resolution FEI Sirion scanning electron microscope and a Delta Nu Raman Microscope using a 532 nm diode laser. A Rigaku powder x-ray diffractometer was used to obtain theta-two theta XRD scans from the samples. CNTs from the diamond substrate were separated and then transferred to a copper grid and analyzed in a FEI Tecnai F20 analytical transmission electron microscope (TEM) with a point-to-point resolution of 0.21 nm to determine the crystalline quality.

5.3. Results and Discussion

Using MPCVD, diamond coatings up to 100 μm thick were processed. Figure 5.1 shows a scanning electron micrograph of a MPCVD processed diamond substrate used in the present study. It can be seen that these substrates have large crystals of diamonds with sharp facets and as a result have rough surfaces. Figure 5.2 shows a theta-two theta x-ray diffraction pattern taken from a diamond substrate. Peaks corresponding to different orientations of the diamond were noted indicating the polycrystalline nature of the diamond substrates. Figure 5.3 shows Raman spectra taken from one of such large crystal diamond substrates. A sharp peak at 1332

cm^{-1} at room temperature is observed with a very low G peak at 1550 cm^{-1} indicating a high degree of sp^3 bonding in the carbon and that the samples are of high quality. Similar sharp peaks were also noted to be present in high quality diamond substrates in literature [14, 15].

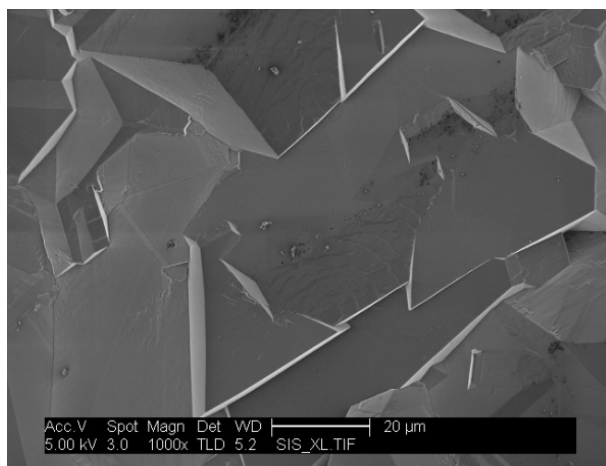


Figure 5.1. SEM micrograph of as grown diamond sample showing facets of crystals

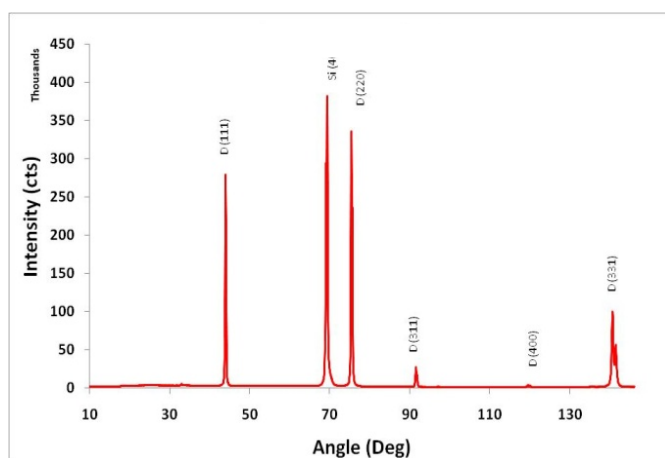


Figure 5.2. X-ray diffraction pattern taken from a diamond substrate

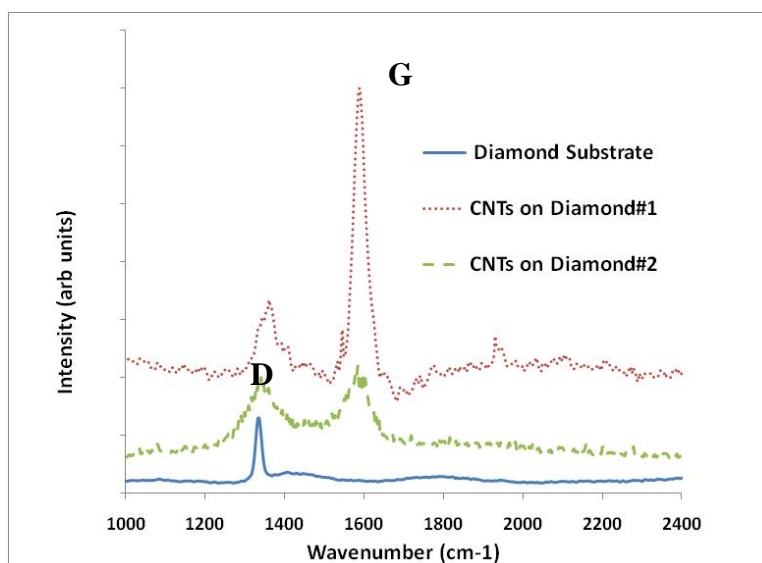


Figure 5.3. Raman spectra taken from a diamond substrate as compared to CNT/diamond samples grown at two different processing conditions

The free standing diamond substrates, obtained by dissolving the Si substrate, were found to be fairly translucent providing an additional indication that the impurity levels (sp^2 carbon, etc.) are in very low concentrations in these substrates. The lower impurity levels in the diamond films are desirable to have better thermal conductivities [1]. In addition, the microstructure of polycrystalline diamond films with grain boundaries also influences thermal conductivity [5-17]. Since the large crystal diamond substrates have a reduced grain boundary area, the in-plane thermal conductivity is expected to be better in large crystal diamond substrates as compared to small crystal diamond substrates. The quality of the diamond substrates just described made by the present set of conditions appears to be most suitable for growing CNTs for thermal management studies.

Complete CNT coverage of rough diamond substrates is very important to have better thermal contact. Several samples with different metal layer thickness and sputtering parameters were experimented on to determine the effect on catalyst coverage, as coverage of the catalyst particles will determine the final CNT coverage. Since intermediate layers were not used, catalyst particle coarsening is likely to occur during the annealing. In addition, the facets present in the diamond could assist in rapid coarsening of the catalyst particles by the presence of the valleys between grains. Figure 5.4 shows a CNT grown on a diamond sample decorated with a 2 – 5 nm thick Ni-9%W-1.5%Fe catalyst using initial set of sputtering conditions (30 mA, 0.44 kV, 200 mTorr Ar, 10 min). After the CNT growth on these samples, it can be seen that only certain facets were found to be covered with a high density of CNTs (bright areas) whereas other areas appear to have a very low density (dark areas). Although the whole area of the substrate is exposed to CNT growth, due to inadequate coverage, only certain areas had the appropriate metal catalysts available for the growth of CNTs.

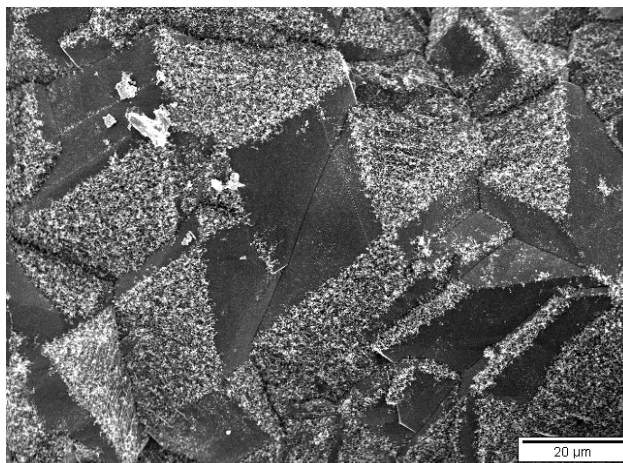


Figure 5.4. Partial coverage of CNTs grown on diamond substrate partially covered with Ni-W- Fe deposited by using initial sputtering conditions

Proper coverage of the surface was obtained using optimized sputtering conditions (190 mA, 0.32 kV, 200 mTorr Ar, 2 min) and around 5 – 9 nm thick Ni was deposited to create the catalyst nanoparticles. As shown in Figure 5.5, complete coverage of the substrate with CNT growth is possible with a catalyst layer. Although the initial diamond substrate surface was rough due to the faceting, the surface is completely covered with a thin layer of CNT carpet. A higher magnification photomicrograph of the samples is shown in Figure 5.6, where randomly oriented CNTs can be clearly seen. A cross-sectional SEM micrograph of the sample is shown in Figure 5.7 demonstrating that 3 – 5 μm thick CNT carpet is present on the samples. Samples processed with the optimized sputtering conditions for Ni-9%W-1.5% Fe also provided similar CNT coverage.

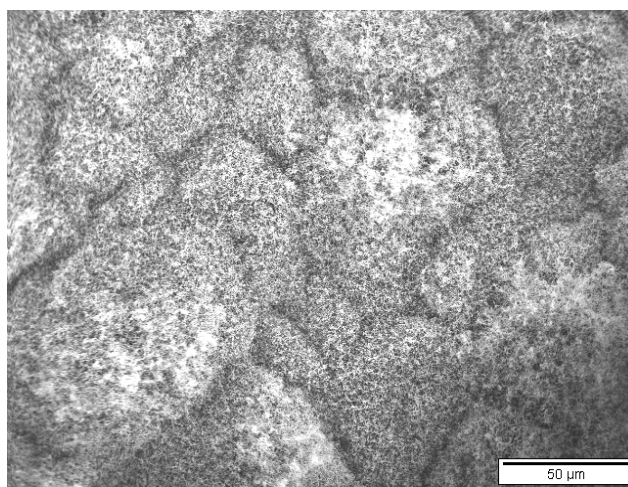


Figure 5.5. Complete coverage of CNTs on diamond substrates with Ni catalysts deposited by sputtering using optimized conditions

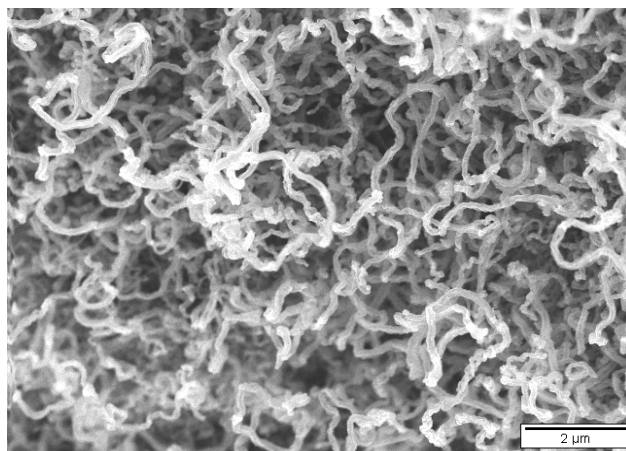


Figure 5.6. Higher magnification pictures showing the CNTs grown on a diamond substrate

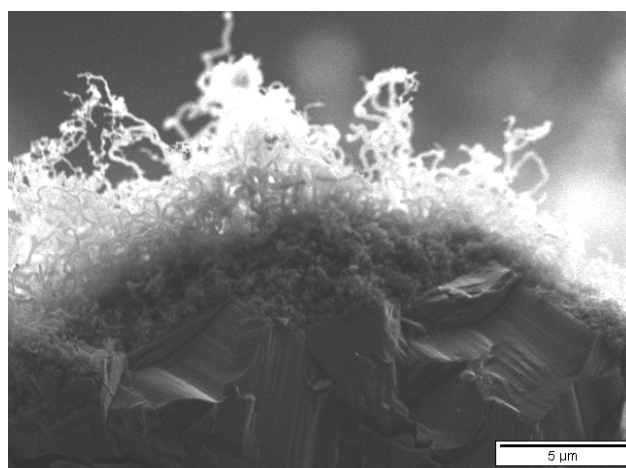
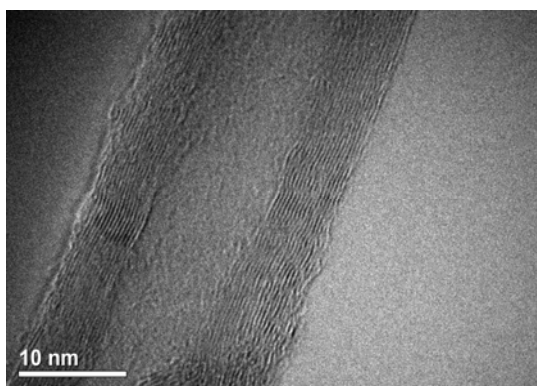


Figure 5.7. Cross-sectional SEM image showing CNTs grown on a diamond substrate

CNTs observed by TEM (image show in Figure 5.8 (a)) indicate that the diameter of the samples is around 20 nm. High resolution TEM of the samples show that a high crystalline quality for the CNT growth is possible on the diamond substrates. This particular image is that of a MWCNT where 16 walls are present as shown in Figure 5.8 (b). In order to further confirm the quality of these CNTs, Raman spectra were taken on different samples. Figure 5.3 shows a D/G peak ratio of 0.89 for the sample grown in atmospheric pressures (CNT/diamond #1). However, in other samples (CNT/diamond #2) grown with Ni islands and 400 sccm of C_2H_2 flow rate in 90 Torr of pressure, a D/G ratio as low as 0.3 are obtained as shown in Figure 5.3 indicating that high quality MWCNTs are possible to grow on diamonds. It is shown in the literature that smaller the D/G ratio, the better the structural purity of the graphitic materials [18] and in the present study samples showed D/G ratio of 0.2 – 0.3 when grown in low pressure.



(a)



(b)

**Figure 5.8. (a) TEM micrograph showing 20 nm diameter CNTs grown on diamond substrates
(b) High resolution TEM micrograph showing 16 Walls of highly crystalline MWCNT**

The lower pressure growth seems to improve the D/G ratio of CNTs grown on diamond as opposed to atmospheric pressure growth. Also prior heat treatment of the catalyst islands did not appear to influence the growth of CNTs as the samples heated in Ar/H₂ environment prior to CVD or the samples treated in the CNT furnace yielded similar quality CNTs. With the growth of CNT on diamond substrates demonstrated as possible for thermal applications, thermal resistance measurements of these substrates are underway.

5.4. Conclusion

Carbon nanotubes (CNTs) were grown on diamond coated Si substrates and free standing diamond wafers to develop efficient thermal interface materials for thermal management applications. High quality, translucent, free-standing diamond substrates were processed in a 5 kW microwave plasma chemical vapor deposition (MPCVD) system using CH₄ as precursor. Ni and Ni-9%W-1.5 %Fe catalyst islands were used to nucleate CNTs directly on to the diamond substrates. Both Ni and Ni-9%W-1.5%Fe catalysts deposited by optimized sputtering conditions

were found to produce CNTs on rough diamond substrates. Randomly oriented multiwalled carbon nanotubes (MWCNTs) forming a mat of ~5 μm thickness and consisting of ~20 nm diameter CNTs were observed to grow in a thermal CVD system using C_2H_2 as precursor. Transmission electron microscopy and Raman analyses confirmed the presence of quality CNTs on diamond showing a D/G peak ratio of 0.2 – 0.3 in Raman spectra.

5.5. References

1. Properties, Growth and Applications of Diamonds, Ed. by M.H. Nazare and A.J. Neves, (2001) p. 32.
2. L.K. Bigelow, *J. de Physique IV* 3 (1993) 897-902.
3. M. Seelmann-Eggebert, P. Meisen, F. Schaudel, P. Koidl, A. Vescan and H. Leier, *Dia. Relat. Mater.* 10 (2001) 744-749.
4. T. Tong, Y. Zhao, L. Delzeit, A. Kashani and M. Meyyappan, *IEEE T. Compon. Pack. T.* 30 (2007) 92-100.
5. K. Kordas, G. Toth, P. Moilanen, M. Kumpumaki, J. Vahakangas, A. Uusimaki, R. Vajtai and P.M. Ajayan, *Appl. Phys. Lett.* 90 (2007) 123105-1-123105-3.
6. L. Zhu, D.W. Hess and C.P. Wong, *IEEE Proc. Elec. Compon. Tech. Conf.* (2007) 2006-2010.
7. B.A. Cola, X. Xu and T. Fisher, *Appl. Phys. Lett.* 90 (2007) 093513-1-093513-3.
8. J. Xu and T. Fisher, *Int. J. Heat Mass Trans.* 49 (2006) 1658-1666.
9. B.A. Cola, X. Xu, T. Fisher, M. Capano and P. Amana, *Nanosc. Microsc. Therm.* 12 (2008) 228-237.
10. H. Wang, J. Feng, X. Hu and K.M. Ng, *J. Phys. Chem. C* 111 (2007) 12617-12624.
11. C. Varanasi, J. Bulmer, L. Brunke, J. Burke, J. Baca, K. Yost and P. Barnes, *J. Vac. Sci. Technol. A* 26 (2008) 832-835.
12. Q. Ngo, B.A. Cruden, A.M. Cassell, G. Sims, M. Meyyappan, J. Li and C.Y. Yang, *Nanolett.* 4 (2004) 2403-2407.
13. P.N. Barnes and R. Wu, *Appl. Phys. Lett.* 62 (1993) 37-39.
14. K. Fabisiak, A. Banaszak, M. Kaczmariski and M. Kozanecki, *Opt. Mater.* 28 (2006) 106-110.
15. R. Ramamurthi, V. Shanov, R.N. Singh, S. Mamedov and P. Boolchand, *J. Vac. Sci. Technol. A* 24(2) (2006) 179-189.
16. D.T. Morelli, C.P. Beetz and T.A. Perry, *J. Appl. Phys.* 64 (1988) 3063-3066.
17. H. Verhoeven, A. Floter, H. Reib, R. Zachai, D. Wittoerf and W. Jager, *Appl. Phys. Lett.* 71 (1997) 1329-1331.
18. E.F. Antunes, A.O. Lobo, E.J. Corat, V.J. Trava-Airoldi, A.A. Martin and C. Verissimo, *Carbon* 44 (2006) 2202-2211.

6. AC Losses in Superconductors

6.1. Introduction

High temperature superconductors (HTS), both as individual tapes or wound in coils, experience alternating current (AC) losses, and generate heat when exposed to AC or applied magnetic fields. Understanding these power losses as a function of transported AC and external alternating magnetic fields is very important due to the planned applications of superconductors in motors and generators [1]. Methods commonly used to extrapolate power loss techniques in which either (a) currents are induced in the superconductor by the application of an external AC magnetic field and a voltage proportional to the electric field is generated in a pickup coil surrounding the sample (hence the magnetic technique), or (b) current is driven through the sample and voltage is measured along the sample (the current transport technique). In both cases, measured power dissipation is related to the part of the voltage which is in-phase with the driving signal, whether it be the external magnetic field in or the applied current [2]. The goal of this project was to build a unique instrument that would directly measure all the AC related losses, both in phase and out of phase from an HTS coil, which may be successful in fostering improvements to existing and newly developed U.S. Air Force power generation, storage and conditioning systems.

The Self Field AC Loss Measurement System (Calorimeter) that was built to meet this need is a cryogenic isothermal calorimeter. It is designed to measure the energy losses in HTS samples carrying AC using the standard nitrogen heat of vaporization method in contrast to bolometric or magnetically inferred means. The samples are characterized by passing varying frequencies and levels of AC through them and measuring the energy losses which show as heat. Liquid nitrogen (LN_2) is used to cool the sample to superconducting temperature. The change in the amount gas evolved from the evaporated LN_2 when a sample is energized is measured, relative to when no power is applied, and energy losses are calculated based on the energy required to convert the liquid to gas.

6.2. Experimental

A system was built into a surplus magnet dewar originally designed to hold liquid helium (LHe). This eliminated the need to design and purchase a custom container for the LN_2 . It also very effectively limited heat flow from outside sources, which contribute to background gas generation and limit the sensitivity of the system. Prior to measuring an HTS coil, a resistance heater was used to characterize the system to determine background flow and response to known energy inputs, and the calibration curve is shown in Figure 6.1.

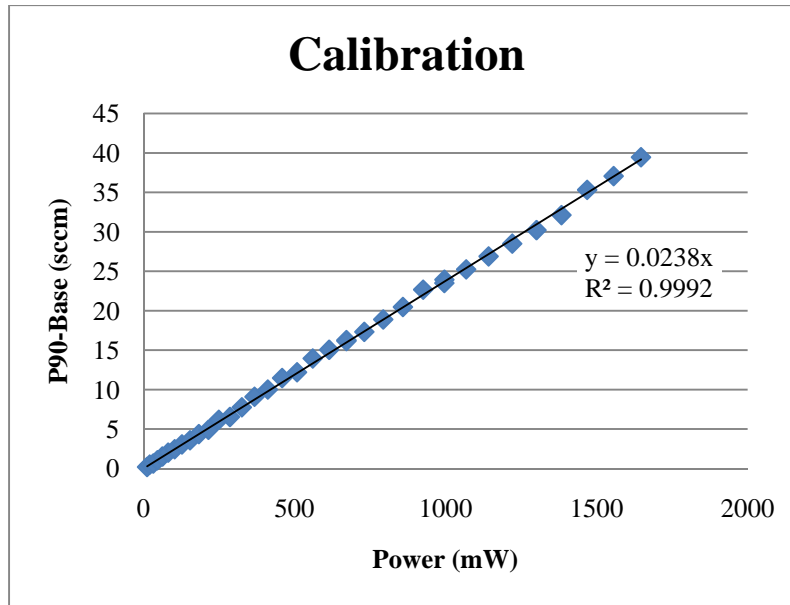


Figure 6.1. Compensation curve from resistance

Since the experimental plan called for measuring heat losses without quenching the coil under test, it was planned that the coil would be prevented from warming enough to actually boil the LN₂. Therefore, the heater used to stimulate a coil should not cause nucleate boiling. The heater is a 10 W kapton-coated flexible heater powered by a Lake Shore Cryotronics (Model 340) temperature controller, and is sandwiched between two aluminum plates as shown in Figure 6.2. This arrangement gives the heater a thermal mass and surface area similar to the coil to be tested, thereby providing a heating/cooling rate and surface heat flux per unit area similar to a coil exhibiting losses (but not quenched). The temperature sensor was used for indication of overheating only, but did verify that increase in gas flow could be measured with a sample having a temperature increase of only a few mK.

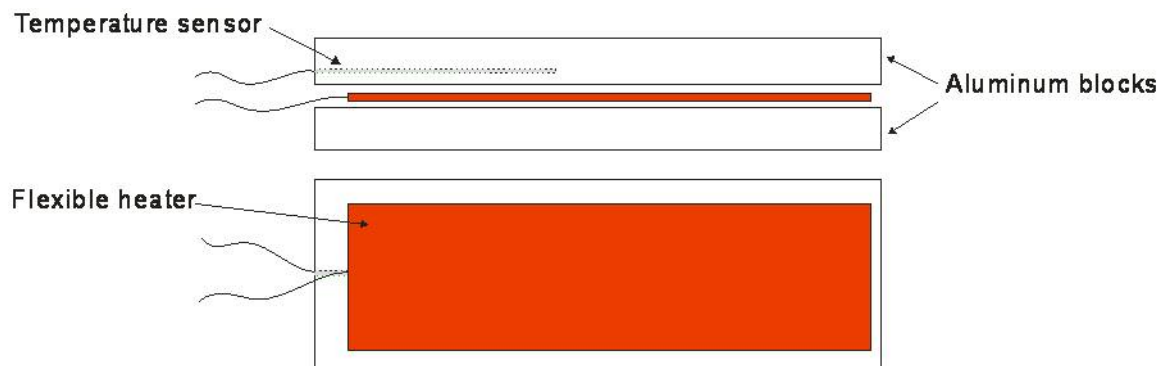


Figure 6.2. Schematic of resistance heater used for calibration

6.2.1. Evolution of the Instrument

The main changes to the Self Field AC Loss Measurement Calorimeter in the most recent iteration were both mechanical and operational. The mechanical change made was to improve heat flow management and provide more sensitive gas measurement. The operational changes consisted of improving fill/purge cycles and timing of sample power application and data collection. As illustrated in the schematic in Figure 6.3, the power leads inside the sample space of the original system had been enclosed in an isolated section of pipe, which was filled with LN_2 to reduce the amount of heat that would be conducted down the power leads into the sample space. This design allowed small amounts of water to condense and accumulate into the lead cooling space, thus causing some instability in the output.

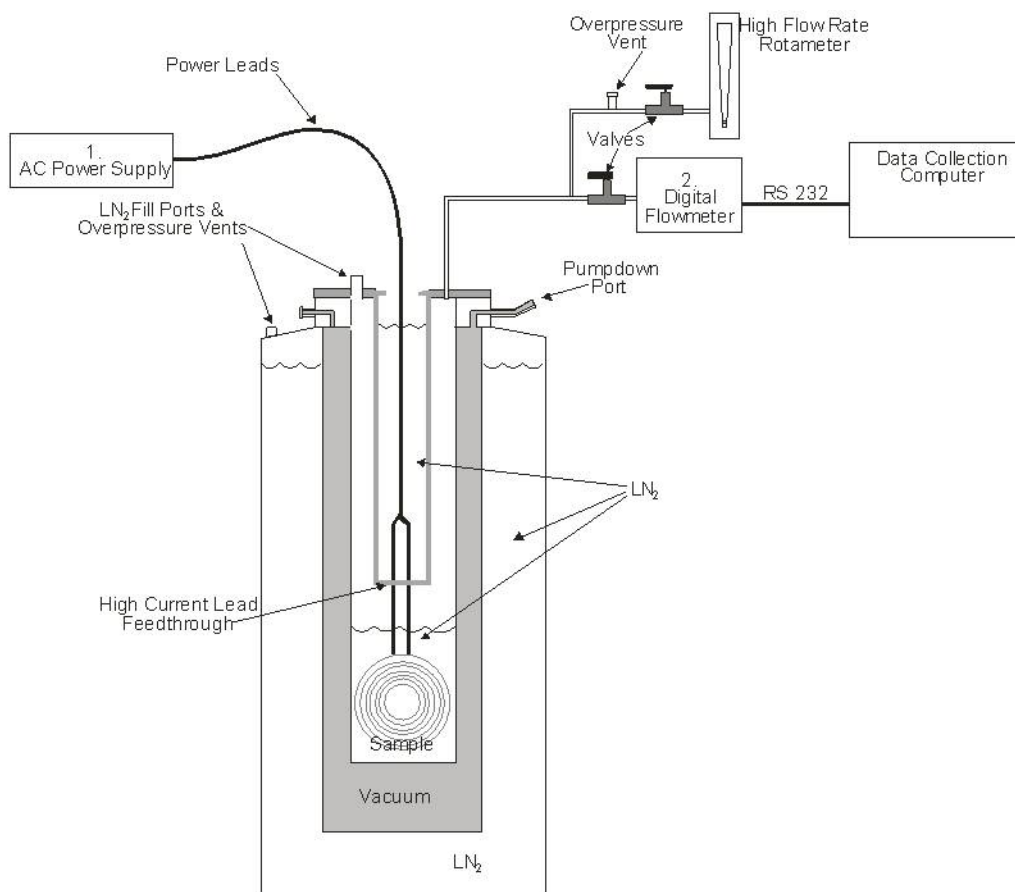


Figure 6.3. Schematic of initial system

Since some of the parameters of the system changed as the level of LN_2 dropped in the power lead cooling section, the time available for stable data collection was limited. By raising the level of the lead cooling LN_2 above the sample space, as shown in Figure 6.4, the amount of time the background flow remained stable was dramatically increased. Other published LN_2 -based calorimeters do not employ this feature. Capping this section permitted maintaining a positive gas pressure to prevent water condensation inside the power lead cooling space. The LN_2 fill

procedure has been continuously refined and the cryogen fill hardware was also modified to permit purging the sample space with fresh LN₂ whenever it was replenished.

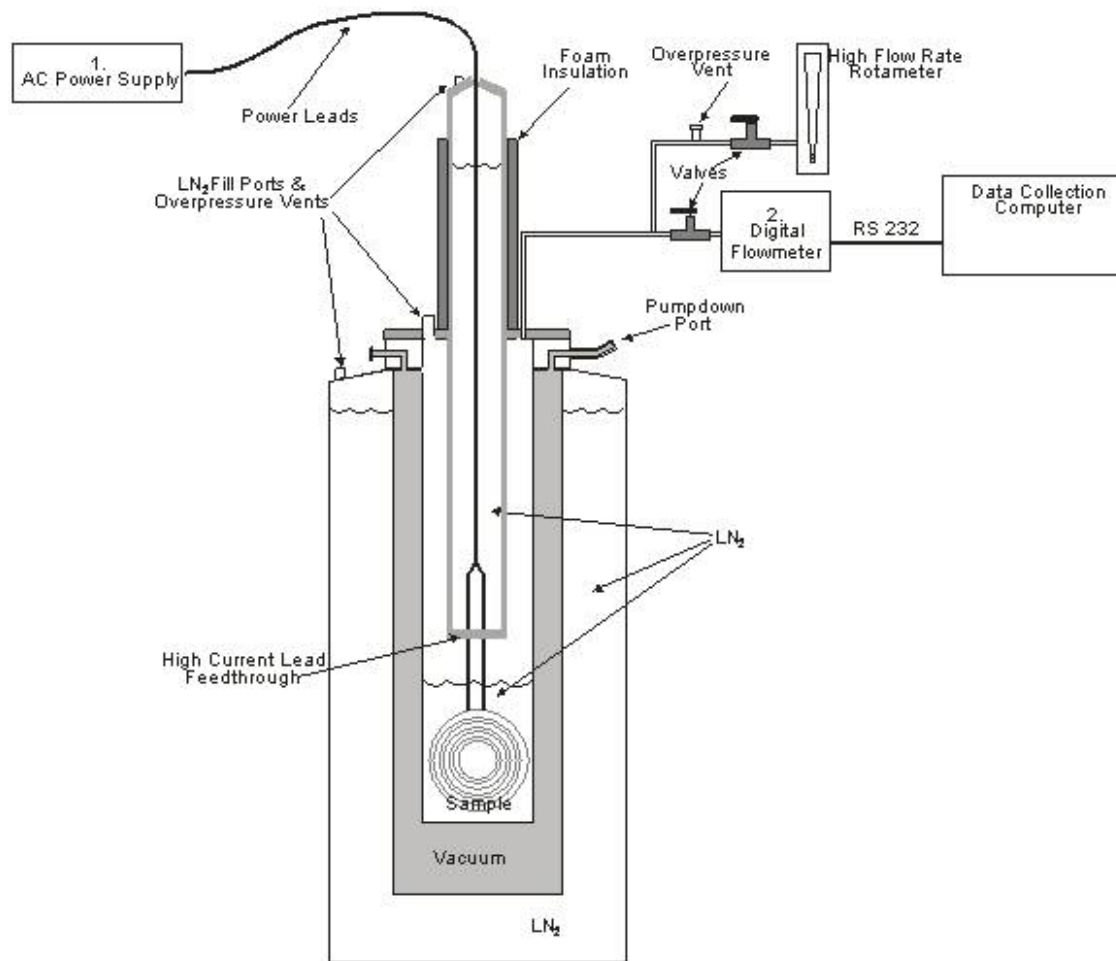


Figure 6.4. Schematic of modified system showing taller lead cooling section

As modifications to the system were made, and the operating procedures improved, it became apparent that the original flow meter was a limiting factor. A more sensitive flow meter (0.01 sccm resolution) was purchased. This permitted direct measurements with a minimum 12 mW sensitivity, using only the linear offset determined from the calibration heater. Figure 6.5 illustrates initial measurements that were done with a 1cm wide x 1 m long piece of YBCO tape coiled into a 2 in. dia. coil.

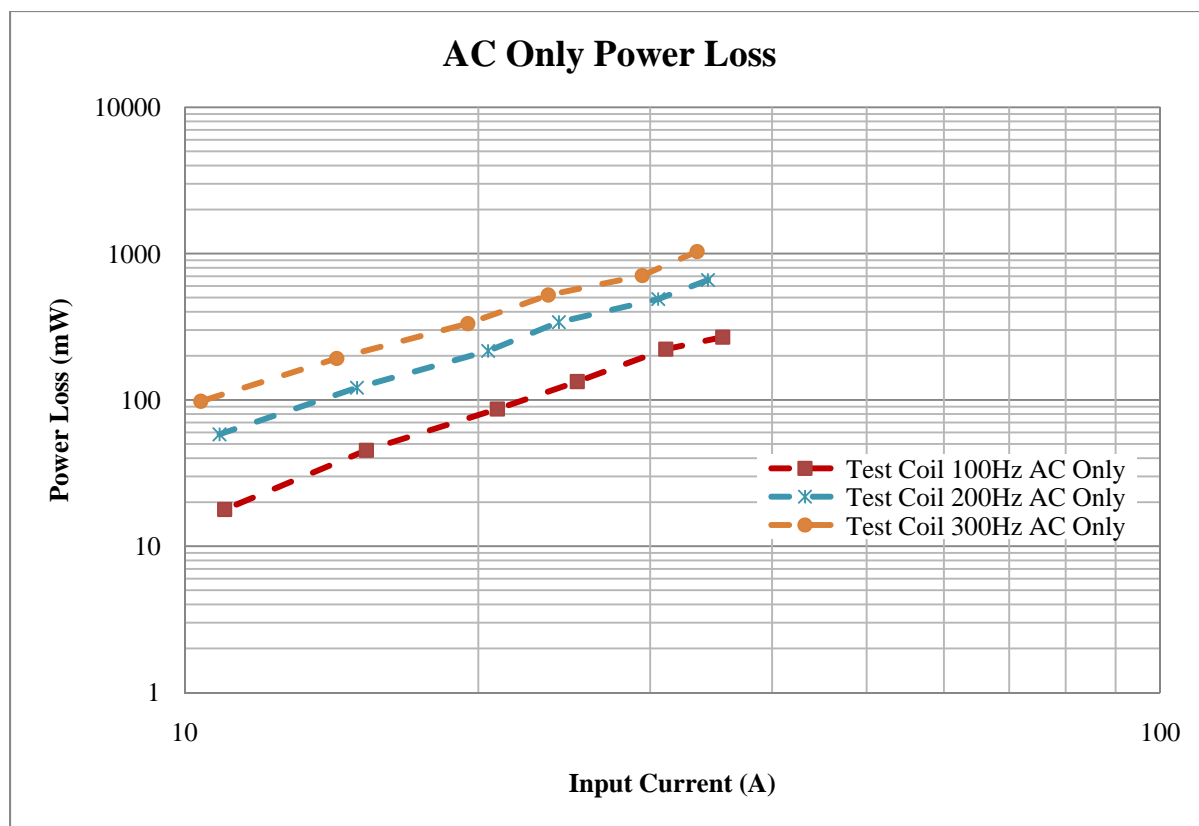


Figure 6.5. Results from initial coil measurements

6.3. Results and Discussion

The Spin Around Magnet (SAM) machine is designed to provide an intense, variable frequency, alternating magnetic field. With the addition of a calorimeter based on the Self Field AC Loss Calorimeter described above, it becomes a system to characterize HTS coils under conditions similar to usage in a generator or motor. UDRI provided conceptual guidance and solved an assortment of basic design hurdles for another contractor doing detailed engineering design for the USAF. Occasionally UDRI provided direct guidance during discussions with the design engineers.

The initial goal called for a device providing a uniform 1 T field, which would completely reverse at up to 400 Hz, across a $2.5 \times 10 \times 10 \text{ cm}^3$ sample space, corresponding to the dimensions planned for experimental test coils. This was to be achieved by spinning a set of permanent magnets, arranged in an eight-spoke Halbach pattern, and nested inside a concentric-aligned, laminated backiron stack, with enough space in between the magnet and backiron to fit the HTS test coil. A schematic of this arrangement is shown in Figure 6.6. The rotating magnet set and the backiron would simulate the magnetic fields around a rotor and stator in a motor or generator. Due to expected sample geometry and necessary volume for a calorimeter in the curved sample space, the gap evolved to 3.8 cm thick with a 0.6 T field.

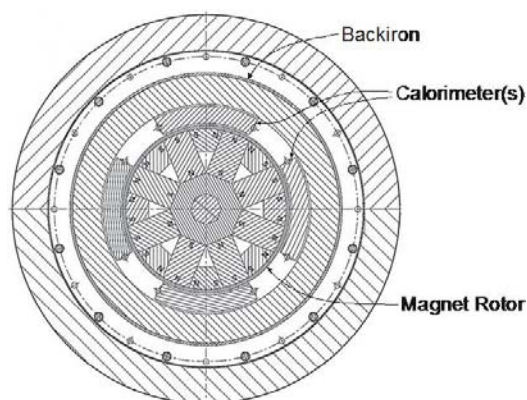


Figure 6.6. Cross section of SAM machine

One of the primary criteria for the sample holding calorimeter was that it function similar to the Self Field AC Loss Calorimeter. Keeping the base gas flow low enough to have reasonable resolution required enough insulation to avoid boiling when no energy was being applied to the sample inside. To eliminate the bulk of having integral vacuum jacket insulation on the calorimeter, it was decided to make the outer shell of the overall system a vacuum vessel. This would eliminate heating from other components via gas conduction. Evacuating the interior also eliminates vibration from wind effects and turbulence between the calorimeter and the surface of the rotor, this gap being only 1mm, and the surface speed of the rotor exceeding 100 mph at 3000 rpm, and is illustrated in Figure 6.7.

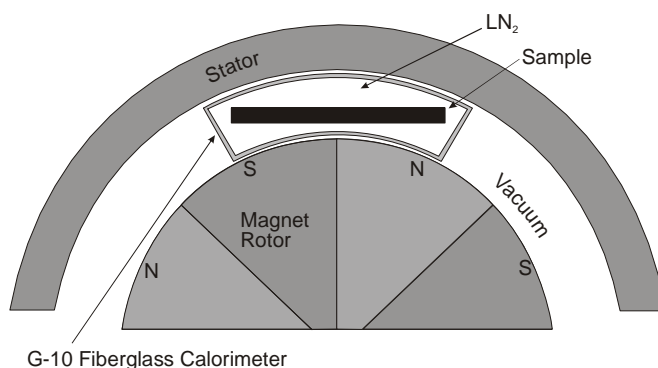


Figure 6.7. Schematic indicating the vacuum space

To reduce the radiant heating effects on the calorimeter, the rotor and stator was first cooled with LN_2 prior to taking measurements with the calorimeter, and the outside of the stator was continuously cooled during measurements. These two features, cooling and evacuating, which together require a cryogenic vacuum chamber, required finer fabrication tolerances between parts and special coating for the rotor bearings as well as fittings and valves for LN_2 transfer. The

calorimeter itself is to be constructed by Milan Polak of the Electrical Research Institute, Slovak Republic, using G-10 fiberglass composite, which has very low thermal conductivity. This limits heat conduction from the calorimeter mounting points.

The USAF was supposed to take delivery of a working device, but received only engineering drawings from the initial contractor when that contract ended. At the USAF's request, UDRI agreed to fabricate a device using the set of engineering drawings provided. It was decided to continue to work with the part fabricators that had provided consultation for the group that gathered the information to prepare the drawings. This required UDRI to contact these fabricators, develop communications, and coordinate their activities. There were initially four companies directly involved in part fabrication: (1) Electron Energies for the magnet fabrication and rotor assembly, (2) Laser Technologies for the back iron lamination fabricator, (3) Champion Bearings for the cryogenic bearing vendor, and (4) Jennison Engineering Services of Pittsburgh for the fabrication of the overall structure parts.

Jennison chose to subcontract out some of the parts, which took nine months longer than their longest projection, and the parts were not inspected prior to delivery to the USAF. This resulted in none of the parts fitting together as shown on the engineering drawings. Some of this was due to taking tolerances of adjacent parts to opposite extremes, and some was due to simply being well out of tolerance. It was decided that, even though Jennison offered to rework the parts, the parts would be reworked locally. This decision was due to shipping costs and the excessively slow initial delivery from Jennison, that is, we were trying to avoid additional delays. As a result, Mound Manufacturing (Dayton, Ohio) was the fifth outside company to be involved. They reworked the components, ranging from 30 to 800+ lbs each, to achieve the final tolerances required to maintain the vacuum seal. The parts were finally assembled at WPAFB by UDRI. Because of the extremely strong magnetic force from the permanent magnets in the rotor, and the tight tolerances, a set of non-magnetic assembly fixtures had to be made to permit handling the 400 lb magnet and install it centered into the stator assembly, without any parts or tools becoming stuck to, or scratching the magnet, which had been balanced to spin at 3000 rpm. These fixtures were designed and machined to fit on-site by UDRI. The magnet rotor has been spun up to 1500 rpm for initial testing and magnetic field measurement. The peak field was recorded at 0.6 T.

6.4. Conclusion

The hardware and techniques developed for the HTS Self Field AC Loss Measurement System are working to the best expectations of the isothermal cryogenic calorimeter. Since its recent upgrade, it has been used to successfully measure losses in a non-coil sample, which has lower losses than coils, and a loosely wound coil, to higher resolution than originally anticipated. More samples of higher quality are being fabricated to specifically be characterized with this instrument. A smaller version is also currently being fabricated to insert into the external alternating field device. This will permit simulating measurement of losses resulting from using HTS coils as components in motors and generators.

6.5. References

1. S.P. Ashworth and M. Suenaga, *Cryogenics* 41 (2001) 77-89.
2. S. Fleshler, L.T. Cronis, G.E. Conway, A.P. Malozemoff, T. Pe, J. McDonald, J.R. Clem, G. Vellego, P. Metra, *Appl. Phys. Lett.* 67 (1995) 3188.

List of Acronyms, Abbreviations and Symbols

AC – Alternating current
B – Magnetic flux density
CNT – Carbon nanotube
CVD – Chemical vapor deposition
FET – Field-effect transistor
FFT – Fast Fourier transform
 F_p – Flux pinning force
 F_{pmax} – Flux pinning force maxima
FWHM – Full width half maximum
H – Magnetic field
HTS – High temperature superconductor
Hz – Hertz
IBAD – Ion-beam assisted deposition
 I_c – Critical current
 J_c – Critical current density
 J_{ct} – Transport critical current density
 J_e – Engineering critical current density
KrF – Krypton-fluoride excimer laser
 λ – Wavelength
LHe – Liquid helium
LN₂ – Liquid nitrogen
MOCVD – Metal-organic chemical vapor deposition
MOD – Metal-organic deposition
MPCVD – Microwave plasma chemical vapor deposition
MRI – Magnetic resonance imaging
MWCNT – Multi-walled carbon nanotube
PLD – Pulsed laser deposition
PPMS – Physical property measurement system
RABiTSTM – Rolling-assisted-biaxially-textured substrate
RHEED – Reflection high-energy electron deflection
rpm – rotations per minute
sccm – Standard cubic centimeters
SEM – Scanning electron microscopy
SIMS – Secondary ion mass spectrometry
SMES – Superconducting magnet energy storage
 T – Temperature
T – Tesla
 T_c – Critical transition temperature
TEM – Transmission electron microscopy
 θ – Bragg angle
YS – Yield strength
YSZ – Yttria-stabilized zirconia